Low SO2 Emission Preheaters for Cement Production

Rasmussen, Martin Hagsted

Publication date:
2011

Low SO_2 Emission Preheaters for Cement Production

Martin Hagsted Rasmussen

Ph.D thesis

2011

Technical University of Denmark
FLSmidth A/S
The Danish National Advanced Technology Foundation

Preface

This Ph.D. thesis is part of the research platform *New Cement Production Technology*, financially supported by *The Danish National Advanced Technology Foundation*, *FLSmidth A/S* and *The Technical University of Denmark*. The focus area for the platform, and especially this project, is to obtain knowledge about the cement production process, and then use this knowledge to develop the cement production process of tomorrow. The supervisor group comprised the following people: Professor Kim Dam-Johansen, Associate Professor Stig Wedel and Senior Advisor Jytte Boll Illerup, from the Department of Chemical and Biochemical engineering, and Ph.D. Kim Hougaard Pedersen from the R&D department at FLSmidth, who took over the supervisor role from Kent Thomsen. I would like to thank all the supervisors for their guidance and the many valuable discussions we have had. Besides the supervisors, a large number of people have influenced the project. Of these, I would especially like to thank the students that have been associated with the project in connection with their Master/Bachelor theses. I am also grateful to the other Ph.D. students connected to the platform for their help and support, as well as the technician staff at the Department of Chemical and Biochemical Engineering, who have been very supportive in solving practical problems during the project. Last but not least, I would like to thank the people inside and outside the R&D department at FLSmidth, who have helped me considerably during the project.

Abstract

The most common way of producing cement today is effected through what is known as the dry process. If the raw materials used in this process contain sulphide, the plant layout can lead to emissions of SO_2 from the preheater tower. SO_2 emissions are most often caused by the oxidation of pyritic sulphide, which occurs between 300 and 600 °C. Of the formed SO_2, around 50% is often said to be emitted from the preheater. However, large variations in this number have been observed, with the circulation of CaO from the calciner given as the main reason for this phenomenon.

One of the experimental goals in this thesis has been to produce CaO with a large surface area in order to increase the absorption of SO_2. For this purpose flash calcination of $CaCO_3$, calcination under vacuum, calcination in a fixed bed and a fluid bed has been tested between 650 °C and 850 °C. The results showed that flash calcination at low temperatures resulted in the largest surface area, about 140 m^2/g CaO. The material produced from all of the methods was a mixture of CaO and $CaCO_3$, meaning that the material was only partly calcined, but with the particle surface area being comprised by CaO.

One focus in this thesis was to investigate the reaction between CaO and SO_2 in the temperature interval where SO_2 is formed within the preheater tower, in order to understand the role of CaO in connection with SO_2 emission. The experiments were conducted using CO_2 concentrations up to 25 %. The reaction times in all cases were less than 1 second, which was possible using an entrained flow reactor. Furthermore, the experimental results were found to be limited by both external and internal diffusion. The reaction product was identified as a mixture of $CaSO_3$ and $CaSO_4$. For temperatures below 600 °C no effect from O_2 was observed. At low CO_2 concentrations the CaO conversion with respect to SO_2 increased with both temperature and surface area. At high CO_2 concentrations no effect or even a negative effect of temperature was seen. In general, CO_2 was found to inhibit the CaO/SO_2 reaction. Based on the CaO experiments under carbonating conditions it was concluded that CaO recirculation within the preheater tower does not influence the SO_2 emission to any significant extend. This conclusion is opposite to what previously has been stated.

Modelling of experimental results concentrates on the results obtained for CaO in non-CO_2-enriched atmospheres. Due to external and internal diffusion limitations and very short reaction times, a time-dependent grain model with chemical reaction between SO_2 and CaO at the shrinking core interface in the non-porous grains was used and found to describe data very well. The outcome of the modelling was that the chemical reaction between SO_2 and CaO is so fast that the observed rates exclusively are determined by solid state diffusion in the product layer of the non-porous CaO grains. An activation energy of 115 kJ/mole was found to fit all CaO sources very well, even though data fitting by the least sum of squares method showed that this figure could be between 90 kJ/mole and 140 kJ/mole, with a corresponding change of

preexponential factors.

The ability to predict emissions is very important in the design of cement plants. In this thesis the zone model concept has been applied to the modelling of the cyclone stages in a preheater tower. The idea is to account for the complex flow pattern in a cyclone stage by dividing it into zones, each zone having special features. In this manner the model can account for gas/solid heat exchange, gas/solid separation, different gas and solid residence times, etc. The model was evaluated against SO_2 data from five full-scale plants, showing satisfactory results in two cases. An investigation of the parameters showed that it was possible to obtain satisfactory results in four out of five cases by allowing the $CaCO_3$ surface area available for SO_2 absorption to be about 4 m^2/g instead of the measured surface areas, which was up to around 10 m^2/g.

Dansk Abstrakt

Den mest almindelige måde at producere cement i dag er ved den tørre metode. Den tørre metode kan, hvis råvarerne indeholder sulfid, føre til udledning af SO_2 fra forvarmertårnet. SO_2 emissionen er ofte forårsaget af oxidering af pyritsulfid, som er oxideret mellem 300 og 600 °C. Af den dannede SO_2 antages det ofte at omkring 50 % vil udledes som SO_2 fra forvarmeren. Imidlertid er store variationer i dette tal blevet observeret med blandt andet recirkulering af kalcinermateriale som en forklaring.

Et af de eksperimentelle mål i denne afhandling har været at producere CaO med et stort overfladeareal. Dette er gjort med henblik på at øge optagelsen af SO_2. Til formålet er benyttet flashkalcinering, kalcinering under vakuum og kalcinering i en fixed bed reaktor samt i en fluid bed. Forsøgene blev udført i et temperaturinterval fra 650 °C til 850 °C. Resultaterne viste, at flashkalcinering ved lave temperaturer resulterede i det største overfladeareal, ca 140 m^2/g CaO. Det kalcinerede materiale var i alle tilfælde en blanding af CaO og $CaCO_3$, hvilket betyder, at materialet kun var delvist kalcineret.

Hovedformålet med denne afhandling har været at undersøge reaktionen mellem CaO og SO_2 i et temperaturinterval hvor SO_2 dannes i forvarmeren. Forsøgene blev udført i en CO_2 koncentration på op til 25 %. Reaktionstiden har i alle tilfælde været kortere end 1 sekund, hvilket var muligt ved brug af en entrained flow reaktor. I alle forsøg blev det fundet at reaktionen var begrænset af både ekstern og intern diffusion. Reaktionsproduktet er blevet identificeret som en blanding af $CaSO_3$ og $CaSO_4$. For temperaturer under 600 °C blev ingen effekt af O_2 observeret. Ved lave CO_2 koncentrationer steg CaO omdannelsesgraden med både temperatur og overfladeareal. Ved høje CO_2 koncentrationer blev observeret en positiv effekt af øget overfladeareal, men ingen effekt eller endda en negativ effekt af temperatur. Overordnet blev det observeret at CO_2 inhiberer CaO/SO_2 reaktionen.

Modellering af de eksperimentelle resultater er koncentreret om de opnåede resultater for CaO i en ikke CO_2 beriget atmosfære. På grund af eksterne og interne diffusionsbegrænsninger og de meget korte reaktionstider er en tidsafhængig grain model med kemisk reaktion mellem SO_2 og CaO på grænsefladen mellem produktlaget og den skrumpende kerne blevet brugt i modelleringen af de opnåede data. Resultatet af modelleringen var, at den kemiske reaktion mellem SO_2 og CaO er så hurtig, at de observerede reaktionshastigheder udelukkende bestemmes af faststof diffusion i produktlaget af de ikke-porøse CaO korn. En aktiveringsenergi på 115 kJ/mol blev fundet brugbar til at beskrive temperaturafhængigheden af alle dataserier, selvom modeltilpasning ved brug af mindste kvadratersmetoden viste, at aktiveringsenergien kunne være mellem 90 kJ/mol og 140 kJ/mol.

Forudsigelse af emissioner er meget vigtig i forbindelse med opførelse og ombygning af cementfabrikker. I denne afhandling introduceres en ny måde at modellere cyklontrinene i et cement forvarmertårn. Ideen er at tage højde for de komplekse strømningsmønstre i en cyklon

ved at opdele et cyklontrin i zoner, som hver har særlige karakteristika. På denne måde kan modellen redegøre for varmeveksling mellem gas og faststof, seperation af gas/faststof separation, forskellige opholdstider for gas og faststof i et cyklontrin, med mere. Modellen er blevet evalueret i forhold til SO_2 data fra fem fuldskala anlæg, og viste tilfredsstillende resultater i to tilfælde. En undersøgelse af modelparametrene viste, at det var muligt at opnå tilfredsstillende resultater i fire ud af fem tilfælde ved at benytte et overfladeareal af $CaCO_3$ omkring 4 m^2/g i stedet for de målte arealer, som var op til omkring 10 m^2/g .

Contents

Chapter 1

Introduction

This chapter will give the reader a short introduction to the background for the thesis and the objectives of the project will be outlined. In order to give the reader of this thesis an overview of the thesis content the chapter also contains an introduction to the three main sections of the thesis.

1.1 Background

Archaeological excavations have shown that as far back as 5600 B.C. cementitious materials were used in the Mediterranean region for the construction of buildings [1]. Today, the most common type of cement is Portland cement, which was developed during the Industrial Revolution in England and named after the isle of Portland in the English channel. In the early days of Portland cement production, clinker was burned in dome and shaft kilns, but in the late nineteenth century these types of kilns were outmatched by the rotary kiln, which has been the preferred method for production of cement clinker ever since.

At the beginning of the modern cement industry, the focus was on how to increase production rates and reduce energy consumption in order fulfil a steadily growing demand for cheap cement. As production facilities grew larger, the environmental impact, especially on the local community, also significantly increased. For this reason, the emission of harmful gases has been an issue for the cement industry since the 1970s. Combined with more awareness of what the emission of harmful gases can do to humans, the number of components subjected to restrictions have increased, while emission limits have been tightened up. The rising focus on environmental aspects has forced cement manufacturers to deal with emission problems, while the delivery of cheap and efficient equipment for handling emissions has become an important area for equipment suppliers. Besides the demand for equipment, predicting emissions has also become more important because new plants, as well as existing plants undergoing reconstruction, are often required to be delivered with a guarantee that the equipment will fulfil emission limitations.

1.2 Objectives

In order to be able to deliver better and cheaper solutions on a continuous basis, as well as predict emission levels more accurately, it is important to increase the fundamental knowledge about emission components. The emission component considered in this thesis is SO_2, which is known to be both formed and to some extent absorbed within a modern cement plant. The fact that the absorption of SO_2 also takes place within a plant means that the emission of SO_2 can be difficult to estimate, since the absorption efficiency of the raw materials must be considered. In previous Ph.D. theses [2,3] concerning SO_2 emissions from cement plants, the focus has been on the formation of SO_2 and how this is absorbed by $CaCO_3$. However, the fundamental knowledge concerning SO_2 absorption by CaO in a cement production context was still limited, so further research was required in order to understand the influence and potential of these components. In order to bring on the desired knowledge the following eight objectives for the project were established.

- Gain knowledge about the CaO/SO_2 reaction under conditions where SO_2 is formed in the preheater.
- To clarify the potential of CaO as an absorbent for SO_2 reduction.
- Be able to model the initial reaction between SO_2 and CaO.
- To test different methods for producing CaO with a large surface area from $CaCO_3$.
- To determine if CaO recirculating in the preheater tower influences SO_2 emission from the preheater .
- Constitution of a reactor model for preheater cyclone stages.
- To predict emission of SO_2 from a preheater tower, using kinetic knowledge obtained in this and previous studies.
- Evaluate the predicted emission against data from full scale plants.

1.3 Report Outline

In order to meet the objectives outlined above the thesis is divided into three main sections, whose content of which are outlined below.

- *Literature Study*
  The literature study is initiated with a description of how cement is produced and followed by a more detailed description of the preheater tower and SO_2 formation in it. Also common methods for dealing with SO_2 emissions are reviewed.
  The rest of the literature study is devoted to the absorption of SO_2, starting with a description of $CaCO_3$, CaO and $Ca(OH)_2$ and their properties, in order to be able to understand how these compounds interacts. SO_2 absorption on $CaCO_3$, $Ca(OH)_2$ and non-calcium containing species are reviewed in order to give a basic understanding of the capability of these compounds to absorb SO_2 in a cement preheater tower. The literature study is completed by a comprehensive review of the CaO/SO_2 reaction and the CaO/CO_2 reaction. The CaO/CO_2 reaction is included in the review because the conditions found in a preheater imply that carbonization of CaO will take place. The CaO/SO_2 literature study also focus on previously published reaction models.

- *Experimental Results*
  This part of the thesis is divided into four chapters, with the first chapter presenting the results obtained in the calcination experiments, where focus has been on producing CaO material with a large surface area. Before presentation of the SO_2 absorption results, calculations and measurements on mass and temperature gradients are carried out in order to understand how to interpret the experimental results for SO_2 absorption. After clarifying the influence of mass and temperature gradients the experimental results for SO_2 absorption on CaO are presented, outlining and explaining the influence of parameters such as CO_2 concentration, temperature, reaction time, surface area, etc.

- *Modelling and Evaluation*
  Kinetic modelling in this thesis concerns the CaO/SO_2 reaction when carbonization of CaO does not influence the results. It has been decided to omit the carbonization reaction due to a lack of data. Modelling of the CaO/SO_2 reaction is done by a time dependent grain model, which is chosen due to the very short reaction time and the mass transfer limitations that was shown to influence the observed results. The kinetic modelling leads to a parameter estimation and comparison with experimental data.
  The modelling part also contains the derivation of the preheater tower model, which introduce a new way of considering a cyclone as a reactor. The preheater tower model is finally evaluated against data from five full scale plants and a parameter study of five relevant parameters are conducted in order to determine their influence on the model.

Chapter 2

Cement and Cement Production

The annual global production of Portland cement constitutes about $1.6 \cdot 10^9$ tonnes [1], making cement one of the largest bulk chemicals produced in the world. Cement is manufactured in virtually all countries due to the geographic abundance of raw materials, with China as the largest producer in the world. Cement manufacturing is a highly energy-intensive process, and the industry consumes 2 % of the world's energy and emits 5 % of man-made CO_2 emission [4]. These figures clearly demonstrate that the cement industry is of great importance for the global society. This chapter will outline the composition of Portland cement and the most modern methods used for producing it, with a special focus on the preheater tower used for energy recovery.

2.1 Cement

Portland cement is the general name given to most of the cement types produced worldwide today. Minor variations in the composition can be found, if special properties are desired. Portland cement mainly consists of four different minerals, which comprise more than 90 wt%: $3CaO \bullet SiO_2$ (Alite), $2CaO \bullet SiO_2$ (Belite), $3CaO \bullet Al_2O_3$ (Aluminate) and $4CaO \bullet Al_2O_3 \bullet Fe_2O_3$ (Aluminateferrite). Gypsum, which is added to the final product, constitutes 4 to 6 wt% of Portland cement. The remaining part of the cement is made up of impurities, which are found along with the raw materials. Table 2.1 indicates the amount of different components in Portland cement as oxides. The table shows that CaO and SiO_2 by far constitute the major part of the final product. Typical values for the different components in the raw meal[1], here stated without impurities, is also shown. About one-third of the raw meal mass can be attributed to Loss On Ignition (LOI), which is almost exclusively due to the calcination of the $CaCO_3$ used as a precursor for forming CaO. This corresponds to the fact that the raw meal contains about 75 wt% of $CaCO_3$.
The mass loss in the calcination process corresponds to a raw meal to cement clinker ratio of

[1] The mixture of raw materials fed into the kiln system is called raw meal.

Components	content in clinker [5]	content in raw meal [5]	impurity limits [1,6]
	wt. %	wt. %	wt. %
CaO	63.76-70.14	≈43	
SiO_2	19.71-24.25	≈ 14	
Al_2O_3	3.76-6.78	≈ 4	
Fe_2O_3	1.29-4.64	≈ 5	
MgO	0-4.51		5
SO_3	0.2-2.07		4.5
K_2O	0.31-1.76		0.8 as $(NaO_2)_e$[2]
Na_2O	0.03-0.33		0.8 as $(NaO_2)_e$[2]
Mn_2O_3	0.03-0.68		0.5
TiO_2	0.21-0.52		
P_2O_5	0.02-0.27		0.22
CO_2	0.03-0.83		
H_2O	0.04-1.11		
Cl_2			0.1
LOI	0.09-1.56	≈ 34	3

Table 2.1: *Composition of Portland cement clinker and raw meal.*

about 1.5, if the raw meal is dry when fed into the kiln system. The raw meal composition stated in Table 2.1 is usually obtained by blending limestone and clay (clay being rich in Si, Fe and Al oxides). If needed, correctives like sand and iron ore can be added to the raw meal in order to achieve the correct composition.
In order to ensure the proper quality of the final product, the amount of certain minor components is limited. Column 4 in Table 2.1 shows some general upper limits for certain elements, but the exact amount that can be allowed depends on a wide range of factors such as what the cement will be used for, the amount of other impurities, production facilities and so on, which is why the acceptable amount must be determined from case to case. However, the limits stated in Table 2.1 cannot be exceeded significantly, and in many cases it is actually desirable to be well below these limits, since a higher market price is then attainable.

2.2 Cement Manufacturing

The four basic methods for producing cement are: wet, semi-wet, semi-dry and dry. Here, the focus will be on the dry method, which is the most commonly used today due to the relatively low energy consumption compared to other methods [5]. The dry method can be divided into the five subsections outlined below:

[2] $(NaO_2)_e$, the effective amount of alkali, is calculated as $0.658(\%K_2O) + \%Na_2O$.

- Quarrying
- Raw meal preparation
- Clinker burning
- Cement grinding
- Cement dispatch

The quarrying of raw materials usually takes place in open quarries situated close to the plant in order to minimise transportation costs. Raw meal preparation, which comprises grinding and blending, takes place in a number of steps in order to ensure that the raw meal consists of a homogeneous mixture of the raw materials, with no more than 15 w/ w % of the raw meal having a particle diameter larger than 90 μm [7]. Simultaneous with grinding and blending, the raw meal is dried using exhaust gas from the kiln system.
Clinker burning takes place in the kiln system outlined in Figure 2.1.

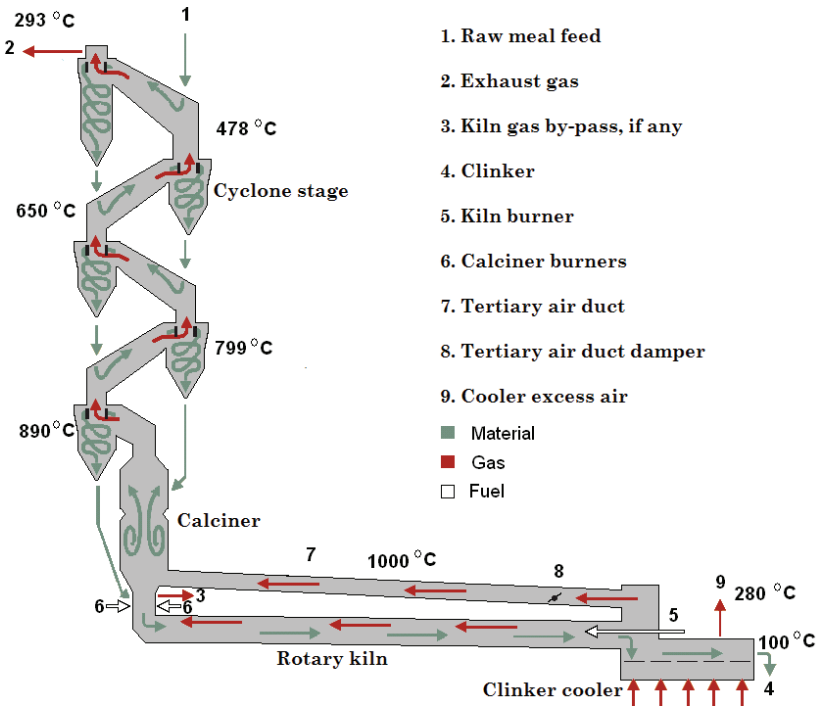

Figure 2.1: *Schematic drawing of a modern dry plant kiln system for cement production [8].*

A modern kiln system in a dry plant consists of a preheater tower with between four and six cyclone stages and a calciner. A cyclone stage consists of a riser duct and the cyclone itself. The cyclone stages are used for heat exchanging cold raw meal with hot gas from the calciner/rotary kiln. In the calciner, about 90 w/w % of the $CaCO_3$ is calcined before entering the rotary kiln,

where the cement clinker is then burned. When the clinker leaves the rotary kiln, they are rapidly heat exchanged with atmospheric air in the clinker cooler in order to recover energy and ensure correct clinker quality. The hot gas leaving the clinker cooler is used for combustion in the kiln and calciner burners, which consume 40 % and 60 % of the total fuel, respectively [5]. If the raw meal and /or fuel contain large amounts of chlorine and alkali metals, recirculation of these elements can make it necessary to introduce a kiln bypass through which a part of the kiln gas is removed in order to prevent coatings from building up in the calciner/rotary kiln. The exhaust gas from the preheater tower is used for drying the raw meal prior to entering the kiln system.

When the clinker are cold, they are ground down to particle sizes smaller than 100 μm in order to produce the final cement product, which is then stored in silos before being dispatched to the end-user. The energy needed to produce one kilogram of clinker in a modern cement plant, as described here, is 3-3.5 MJ/kg clinker [5]. This energy consumption is divided between 15 % electrical energy and 85 % fuel combustion [1].

Chapter 3

The Preheater Tower and SO_2 Formation/Reduction

The emission of SO_2 into the atmosphere is known to cause the formation of acid rain and smog. This is the main reason why industries emitting SO_2 are subject to legislation limits on emission levels, at least in the Western world. Dealing with legislation limits can be rather expensive for cement plants, which is why the availability of cheap SO_2 abatement methods with high efficiency levels is of great importance. This chapter discusses SO_2 emission and how it is formed. The chapter will begin with a detailed description of the preheater tower, followed by a description of known methods for dealing with SO_2 emission from cement plants.

3.1 The Preheater Tower

The idea of using a preheater tower consisting of cyclones for heat exchanging hot kiln gas with cold raw meal was used for the first time in the 1950s, with the calciner introduced about 20 years later. Besides the better utilisation of energy, the preheater tower also makes it possible to shorten the rotary kiln [9]. The preheater tower has various configurations; for instance, FLSmidth & CO. A/S offers six different basic designs [10]. The preheater tower operates as a non-ideal counter-current heat exchanger, where gas and raw meal are mixed and separated in every cyclone stage. Modern preheater cyclones are designed to minimise the pressure drop and height of the cyclone stages, which means that the highest separation efficiency is not necessarily obtained, resulting in large quantities of raw meal recirculating within the preheater tower [11]. However, the top cyclone is typically designed with a higher separation efficiency than the intermediate cyclones, so a minimum amount of raw meal escapes the preheater tower. The pressure drop over the preheater tower depends on the number of cyclone stages, but for modern low pressure cyclones this figure is in the order of 30 mbar [11]. The residence time of solid material in a cyclone stage has been measured to be about 8 s [12], while the gas residence

time in a cyclone stage is about 1-2 s [5].
The mass of air needed for combustion per mass of clinker is about 1 kg/kg [5]. However, the exhaust gas also includes CO_2 from the calcination process, false air and excess gas generated from combustion of fuels, which results in about 1.8 kg of exhaust gas per kg clinker [2]. The exhaust gas, in round numbers, contains 30 % CO_2, 5 % O_2 and balance N_2. The diameter of the cyclones depends on the production rate; for instance, a plant producing 2150 tonnes of clinker per day has a vessel diameter of 5.7 m [13]. The radiation heat loss from the cyclone stages to the surroundings constitute 2-3 % of the total energy required [14].
According to Duda [15], 80 % of the heat transfer in the cyclone stage takes place in the riser duct, while only 20 % occurs in the cyclone. Experiments carried out by Delong and Daohe [16] on cement raw meal showed that heat transfer took place exclusively in the riser duct, with a temperature difference between the particles and gas of about 30 °C. It is generally accepted that the heat exchange between gas and raw meal takes place almost instantaneously, which is why the cyclone itself is used mainly for separating solid material and gas [1].
A number of authors [2, 17–20] have modelled the cyclone part of the preheater tower. Of these authors, some [18–20] considered mass and energy balances only, while others [2, 17] also considered the cyclone as a reactor. Belot et al. [17] assumed that the cyclones were perfect stirred tank reactors, and stated that the simulation results were within the measurement uncertainty of the plant data (no data for SO_2 was mentioned). Hansen [2] assumed that the cyclone stages behaved like plug flow reactors, where solids and gas were mixed gradually. The separation of gas and solids was assumed to take place instantaneously in the outlet. Hansen [2] was able to satisfactorily estimate the pyrite oxidation in most cases, but the predicted emission of SO_2 was too high in all stated scenarios.

3.2 Formation and Emission of Sulphur Dioxide

The reduction of SO_2 emissions has been an important issue for the cement industry for a number of years, with the need for knowledge and methods to deal with SO_2 emission still growing due to tighter and tighter emission limitations, especially in Europe and northern America. For instance, the 2008 proposal from the Environmental Protection Agency (EPA) [21] suggests a limit of 0.6 kg of SO_2 per tonne of clinker, resulting in plants running with a high sulphur content in raw materials expecting to spend 5-7 % of the clinker sales price to deal with the proposed limits.
In a cement plant, SO_2 originates from both fuel and raw meal. The SO_2 from fuel is released in either the kiln burner or the calciner. However, SO_2 originating from the fuel does not constitute an emission problem in relation to exhaust gas, since the calciner and the bottom cyclone work as dry scrubbers, which in practice remove all SO_2 originating from the fuel. SO_2 originating from the raw meal evolves mainly in the preheater tower through the oxidation of pyrite and

organic sulphur impurities, with most of the sulphur found as pyrite inclusions [2]. The oxidation of sulphur species starts to take place between 300-600 °C [22], which in a preheater tower like that shown in Figure 2.1 corresponds to the two top cyclones. Of the sulphur entering with the raw meal, it is often assumed that 50 % will leave the preheater tower as SO_2 [23, 24]. However, the amount can range from 10 to 65% [23], leading to severely incorrect estimations of SO_2 emissions as a result. Salmento and Shenk [23] stated that, based on laboratory tests and plant measurements, they had developed a simple correlation for predicting SO_2 emission.
Bech and Gundtoft [24] noted, based on plant emission data, that an increased number of cyclone stages in the preheater tower also increased SO_2 emission, which they explained by establishing that less CaO reaches the top stages when the number of cyclone stages increases.
The decomposition of pyrite was reviewed by Hu et al. [25], who found that in an atmosphere containing oxygen, pyrite can decompose by direct oxidation (equation 3.1) or by the thermal decomposition of pyrite to pyrrhotite and sulphur, followed by subsequent oxidation to SO_2 and iron oxides (equation 3.2). At temperatures below 525 °C the dominating mechanism will be reaction 3.1, if the O_2 concentration is high enough; otherwise, reaction 3.2 will dominate the SO_2 formation.

$$2FeS_2(s) + 5.5O_2(g) \rightarrow Fe_2O_3(s) + 4SO_2(g) \tag{3.1}$$

$$2FeS_2(s) \rightarrow 2FeS_x(S) + 2(1 - 0.5x)S_2(g) \overset{O_2(g)}{\rightarrow} Fe_2O_3(s) + 4SO_2(g) \tag{3.2}$$

Below 600-650 °C iron sulphates may also be formed, slowing down oxidation due to pore blockage. However, this is only occuring if the gas phase concentration of SO_2 is high. Hu et al. [25] also concluded that even though the oxidation and thermal decomposition of pyrite are well understood, the literature lacks kinetic data and proper modelling.
The oxidation mechanism of pure pyrite particles and pyrite inclusions in shale was studied by Hansen [2] for conditions found in a preheater tower. He found that the oxidation of pyrite inclusions in shale started at 350 °C, whereas pure pyrite particle oxidisation first took place above 400 °C. Moreover, the oxidation rate of pyrite inclusions in shale increases significantly faster with temperature than the oxidation rate of pure pyrite particles. The difference was explained by the effect of impurities and smaller size of pyrite inclusions found in the shale. By using entrained flow reactor measurements, Hansen [2] found that pure pyrite particles self-ignited at about 525 °C, which was not observed for pyrite inclusions in shale due to the smaller pyrite crystal size. Hansen [2] finally concluded that great care must be taken when using results obtained on pure pyrite to model pyrite inclusions found in raw meals.

3.3 Sulphur Dioxide Reduction in Cement Plants

Methods for reducing SO_2 emission from cement plants have been an issue for a number of years, during which time a large number of patents and patent applications [26–36] have been submitted, with different approaches on how to solve SO_2 emission problems in cement production. The methods are by Cembureau [5] divided into three categories, as outlined below:

- **Reduction of precursors:** If less precursor for emission is fed into the kiln system, emissions will be reduced as a natural consequence. This can be done by intelligent mining, where areas with a high content of precursor in the quarry are avoided. Another possibility is to substitute one or more raw materials with some that contain less emission precursor. In general, the reduction of the precursor can be a fairly cheap way to deal with emission problems. However, if the precursor is evenly distributed and found in one of the main raw materials, this method is not applicable.

- **Primary reduction methods:** These methods cover solutions where emission problems are solved by making a minor change to the existing process, so that absorption is incorporated in the process. Miller and Hansen [37] summarised some of the primary methods that can be used such as using a calciner slip stream whereby a part of the calciner material is recirculated to the top stages of the preheater tower in order to absorb SO_2. By doing so, a SO_2 reduction of 25-30 % is possible when recirculating about 5 % of the calciner material. The injection of hydrated lime into the top stages of the preheater tower is another primary reduction method, which is able to reduce SO_2 emission by 45-70 %. However, the cost of hydrated lime makes the operating costs relatively high. In order to deal with the high material costs, a primary method where calciner material is hydrated before being added to the process is also described by Miller and Hansen [37].

- **Secondary reduction methods:** These are methods that rely on equipment installed as separate units in order to deal with emission problems. Often the cleaning units are well known from, for instance, power plants. The advantage of secondary units is that emission reduction is very high, often more than 90 %, which is why it can be necessary to implement a secondary reduction method if emission problems are severe. However, primary reduction methods or the reduction of precursors are preferable, especially due to the high capital investment costs connected with secondary reduction methods.

Chapter 4

Limestone, Quicklime and Slaked Lime

$CaCO_3$ (limestone), CaO(quicklime) and $Ca(OH)_2$ (slaked lime) are all related to SO_2 absorption in the preheater tower, whereby the physical properties of these three materials become key parameters in understanding how SO_2 is absorbed.
Calcium carbonate, often referred to as limestone, is a naturally occurring mineral, which covers about 10 % of the earth's land surface [38]. It is used as a raw material in a wide range of industries such as construction and building, agriculture, glass manufacturing and, of course, cement production. From limestone it is possible to produce CaO (quicklime), which is formed by the thermal dissociation of limestone, also known as calcination. Quicklime does not exist in nature because it will react and form limestone when exposed to CO_2 in the atmosphere. Quicklime also readily reacts with water to form $Ca(OH)_2$, also known as slaked lime, which is not naturally occurring either because it also easily reacts with CO_2 forming limestone. This chapter will outline the properties of limestone, quicklime and slaked lime.

4.1 Calcium Carbonate (Limestone)

Naturally occurring limestone is formed by either an inorganic or an organic route. The inorganic route involves the precipitation of $CaCO_3$ from sea water and inland waters [38]. The organic route is comprised of organisms which build shells and skeletons, or secrete carbonates. Most of the commercially available $CaCO_3$ is formed by the organic route [38]. According to Oates [38], there are several ways to characterise naturally occurring $CaCO_3$. The most interesting classification from a chemical point of view is the following, which is based on the content of $CaCO_3$.

- ultra-high-calcium (more than 97 % $CaCO_3$)
- high-calcium, or chemical-grade (more than 95 % $CaCO_3$)
- high purity carbonate (more than 95 % $CaCO_3$ + $MgCO_3$)

- calcitic (less than 5 % $MgCO_3$)
- magnesian (5-20 % $MgCO_3$)
- dolomitic (20-40 % $MgCO_3$)
- high magnesium dolomite (40-46 % $MgCO_3$)

When used for cement production, only limestones falling within the first four categories are suitable, because of the limitations placed on magnesium content in the final product.
Limestone used for cement production is found in two crystal forms, namely calcite (rhombohedral crystal structure) and aragonite (orthorhombic crystal structure). However, aragonite will slowly be converted into calcite in the presence of water or if the temperature is above 400-500 °C. For these reasons, the most commonly found crystal structure of limestone in nature is the calcite structure. Calcite will form dolomite ($CaMg(CO_3)_2$) in the presence of sea-water. However, such deposits will not be of relevance for cement manufactures. A third crystal structure called vaterite is also known. However, it is easily converted into calcite or aragonite when exposed to water, which is why it has no practical importance in relation to cement production.
All limestones are crystalline, with crystal sizes ranging from less than 4 μm to about 1000 μm in rare cases, and most limestones having an average crystal size around 2-4 μm. According to Boynton [39], very large variations in crystal size and shape can be observed within the same limestone. Figure 4.1 shows SEM images of different limestones, and it is clear that the limestones are made up of small crystals with different sizes and shapes. In natural limestones these crystals are normally non-porous. It should be noted that the limestone shown in Figure 4.1(b) was the parent limestone for most of the experiments in this thesis. From a chemical point of

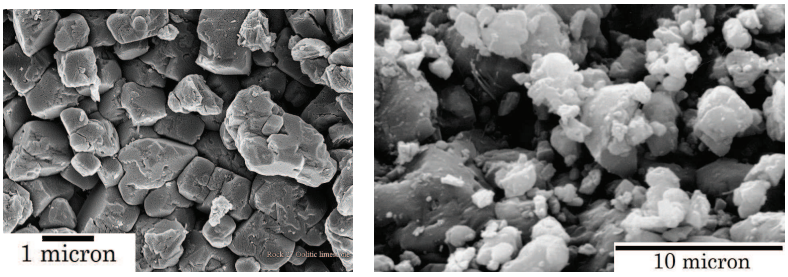

(a) Oolitic limestone, Pickering, North Yorkshire, England [40]

(b) Faxe Bryozo limestone, Fakse, Denmark [41]

Figure 4.1: *SEM images of different limestones (a) and (b).*

view, impurities contained in limestone are of interest, since they can influence reactivity, sintering and calcination behaviour [39]. In Table 4.1, the typical impurities found in limestones are listed. As highlighted in the table, the variation in impurities can be great, which is why limestone samples from different places are usually not identical.

Impurity	Typical range			Impurity	Typical range		
	low	high	unit		low	high	unit
Silica (as SiO_2)	0.1	2	w/w%	Copper	1	30	mg/kg
Alumina (as Al_2O_3)	0.04	1.5	w/w%	Fluoride	5	3000	mg/kg
Iron (as Fe_2O_3)	0.02	0.6	w/w%	Lead	0.5	30	mg/kg
sulphur (as $CaSO_4$)	0.01	0.5	w/w%	Mercury	0.02	0.1	mg/kg
Carbonaceous matter	0.01	0.5	w/w%	Molybdenum	0.1	4	mg/kg
Manganese (as MnO_2)	20	1000	mg/kg	Nickel	0.5	15	mg/kg
Antimony	0.1	3	mg/kg	Selenium	0.02	3	mg/kg
Arsenic	0.1	15	mg/kg	Silver	0.2	4	mg/kg
Boron	1	20	mg/kg	Tin	0.2	15	mg/kg
Cadmium	0.1	1.5	mg/kg	Vanadium	1	20	mg/kg
Chromium	3	15	mg/kg	Zinc	3	500	mg/kg

Table 4.1: *Impurities often found in limestone [38].*

When limestone is heated, sintering can take place if the partial pressure of CO_2 is high enough to prevent decomposition. According to Hu et al. [25], sintering was observed to start at 700 °C, which they state to be 167-328 °C above the Tammann temperature for $CaCO_3$. It has furthermore been observed that in the case of limestone higher CO_2 partial pressure prevents sintering [25].

4.2 Calcium Oxide (Quicklime)

Quicklime is not naturally occurring, so it must be prepared by the calcination of limestone according to reaction 4.1. The reported enthalpy for limestone calcination is 180 kJ/mol at 25 °C [38]. The partial pressure of CO_2 determines whether the calcination reaction takes place. In the literature the equilibrium pressure of CO_2 for reaction 4.1 is usually expressed in terms of a Clausius-Clapeyron relation, equation 4.2.

$$CaCO_3(s) \rightleftarrows CaO(s) + CO_2(g) \tag{4.1}$$

$$P_{eq,CO_2} = P_{0,CO_2} \cdot exp\left(\frac{-\Delta H_{vap,CO_2}}{R_{gas} \cdot T}\right) Pa \tag{4.2}$$

Here, P_{eq,CO_2} denotes the equilibrium pressure of CO_2, P_{0,CO_2} is the pre-exponential factor and $\Delta H_{vap,CO_2}$ is the enthalpy of the reaction. Table 4.2 summarises literature values for the pre-exponential factor and the enthalpy of vaporisation.
Quicklime is crystalline with large variations in grain size. Some quicklimes appear to be amorphous; however, according to Boynton [39], they are micro-crystalline, which can be difficult to observe by X-ray diffraction for very small crystals. The crystal structure of quicklime is cubic,

Author	P_{0,CO_2}	E_{eq}	P_{eq,CO_2} = 1atm	P_{eq,CO_2} = 0.3atm
		kJ/mol	°C	°C
Garcia-Labiano [42]	$4.15 \cdot 10^{12}$	170.2	894	820
Baker [43]	$1.22 \cdot 10^{12}$	159.1	901	820
Hu and Scaroni. [44]	$1.82 \cdot 10^{12}$	163.6	905	825
Silcox et al. [45]	$1.0 \cdot 10^{13}$	179.1	896	824

Table 4.2: *Parameters for calculating the equilibrium pressure of CO_2 above limestone.*

with a unit cell edge length of 0.4778 nm, while its skeletal density is 3340 kg/m^3. The particle density for most commercial quicklimes is 1.6-2.8 depending on the porosity, which normally lies between 18 and 54 % depending on the parent limestone and how the CaO has been produced. If CaO has not been heavily sintered, the porosity will be considerably greater than what is observed in the parent stone due to the smaller molar volume of CaO. Figure 4.2 shows SEM images of quicklime sintered to different degrees. From Figure 4.2(a), it is evident that the crystal size is approximately the same as that observed in Figure 4.1 and 4.1(b). In Figure 4.2(b), the grains have started to sinter, forming larger grains, while in Figure 4.2(c) the original structure has vanished.

The phenomenon of quicklime sintering has been studied by, for instance, Beruto et al. [46], who showed that it was possible to undertake long-time and low-temperature calcination using a vacuum, without any significant loss of surface area in the calcined product. Fuertes et al. [47] found a negative effect of temperature on surface area using long calcination times. Agnew et al. [48] found that at calcination times less than 1 s the degree of calcination, as well as the surface area, increased with temperature. When the calcination process was achieved without significant sintering, a bipartite pore system was observed [47, 49]. In the bipartite pore system the main pores were also found in the parent limestone. These pores have a diameter around 1 μm. The secondary pore system is situated within the original $CaCO_3$ grains and comprises small CaO crystals formed in the calcination process. In a non-sintered particle these crystals will form pores with a particle diameter of about 20 nm. However, the secondary pore system will rapidly increase in size as sintering of the CaO crystals becomes more pronounced. Glasson [50] found that components such as NaCl and Fe_2O_3 accelerated the sintering of CaO, resulting in a smaller surface area and larger CaO crystals. Fuertes et al. [47] showed that CO_2 in the gas phase strongly increases the sintering process, with the effect increasing with increasing CO_2 concentration. The negative effect of CO_2 was observed also by Borgwardt [51], who likewise found that water in the gas phase strongly increases sintering. He further observed that the sintering effect of CO_2 and water are additive. Borgwardt [52] observed that quicklime based on naturally occurring limestones sinters faster than pure CaO in N_2, which was explained by impurities in the parent limestone. Chen et al. [53] found that above 60 vol% CO_2 the effect upon sintering levels off. They also observed the time required to obtain a 100 % calcination increase

when the CO_2 content in the gas increases. When carrying out sintering experiments in nitrogen, Borgwardt [52] observed a sharp decline in surface area at about 850 °C, indicating that sintering had started, but which was 300 °C lower than what would be predicted from the Tammann temperature. Borgwardt [52] also observed that the decrease in surface area happened simultaneously with a decrease in porosity, as also observed by Bruce et al. [54], indicating that the particles were shrinking during the sintering process. Other authors [47] did not observe any shrinkage.

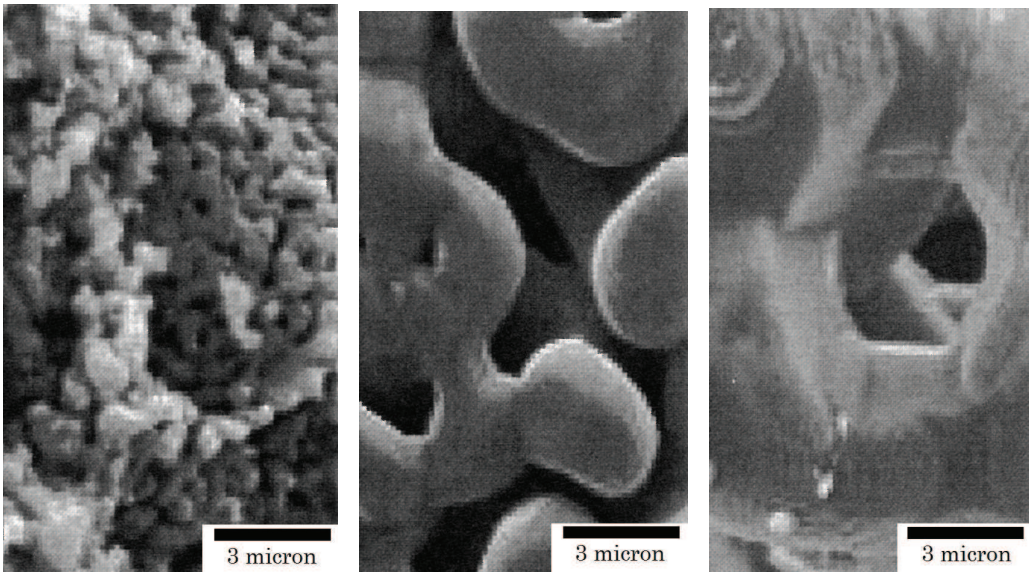

(a) Soft burnt CaO [55] (b) Medium burnt CaO [55] (c) Hard burnt CaO [55]

Figure 4.2: *SEM images of CaO, which is calcined for different periods of time. The calcination time increase from left to right.*

4.3 Calcium Hydroxide (Slaked Lime)

Slaked lime is formed when quicklime comes into contact with water or moisture, according to equation 4.3. The stability of $Ca(OH)_2$ depends on temperature, and the partial pressure of water and is often modelled by a Clausius-Clapeyron expression, equation 4.4. Table 4.3 summarises literature values for the calculation of the equilibrium pressure of water above $Ca(OH)_2$. From the table it is interesting to note that there is some disagreement about the parameters, which might be due to impurities in the quicklime used.

$$CaO(s) + H_2O(g) \rightleftarrows Ca(OH)_2(s) \tag{4.3}$$

$$P_{eq,H_2O} = P_{0,H_2O} \cdot exp\left(\frac{-\Delta H_{vap,H_2O}}{R_{gas} \cdot T}\right) Pa \tag{4.4}$$

Author	P_{0,H_2O}	$\Delta H_{vap,H_2O}$	P_{eq,H_2O} = 1atm
		kJ/mol	°C
Halstead and Moore [56]	$8.71 \cdot 10^{11}$	104.1	511
Matsuda et al. [57]	$1.93 \cdot 10^{13}$	138.2	599
Hartman et al. [58]	$1.11 \cdot 10^{12}$	109.4	538

Table 4.3: *Parameters for calculating the equilibrium pressure of H_2O above slaked lime.*

The crystal structure of $Ca(OH)_2$ is hexagonal symmetry [38] and consists of micro-crystalline agglomerates with a skeletal density of 2240 kg/m^3. The process of lime slaking is exothermic, with an enthalpy of 65 kJ/mol [55].
On the exposure of slaked lime to an atmosphere containing CO_2, it will react and form $CaCO_3$ [59]. Glasson [60] investigated the rate of hydration of CaO, finding that hydration was faster when the surface area increased. In all cases Glasson [60] found that it was possible to obtain 100 % hydration. The very low calcination temperature of $Ca(OH)_2$ means that the literature related to the subject concentrates on sintering of the CaO formed when slaked lime decomposes. The decomposition of $Ca(OH)_2$ was studied by Irabien et al. [61], who found that the evolved surface area was not affected up to 500 °C. At a calcination temperature of 500 and 600 °C the same decline in surface area was observed, while at 700 °C and higher temperatures the surface area declined as the temperature increased. The decrease in surface area observed at 500 and 600 °C might not be caused by sintering, but rather the formation of the cubic CaO structure.

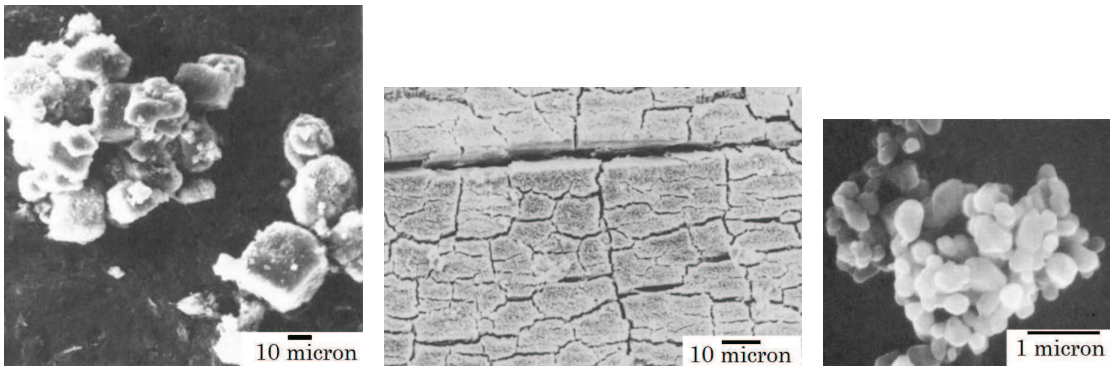

(a) $Ca(OH)_2$ [46] (b) CaO formed from $Ca(OH)_2$ at 395 °C [62] (c) CaO formed from $Ca(OH)_2$ at 800 °C [63]

Figure 4.3: *SEM images of $Ca(OH)_2$ and CaO derived from $Ca(OH)_2$.*

The SEM image of $Ca(OH)_2$ crystals in Figure 4.3(a) shows that these crystals have the same grain structure observed in both $CaCO_3$ and CaO. The SEM image of $Ca(OH)_2$ calcined at low temperatures (Figure 4.3(b)) shows a crystal surface with a number of slits in it and not the expected CaO crystal structure. This behaviour is explained [46] by the fact that CaO formed at low temperatures will maintain the crystal structure of $Ca(OH)_2$ until the CaO crystal has got time and/or the temperature is high enough for them to rearrange into the cubic form. Figure 4.3(c) shows the expected grain structure of CaO. Based on this evidence, it is doubtful whether slaked lime sintering will happen to any significant extent before it decomposes.

Chapter 5

SO_2 Absorption by $CaCO_3$, $Ca(OH)_2$ and Non-Ca Species in the Raw Meal

As outlined earlier, only a fraction of the formed SO_2 will escape the preheater tower and cause SO_2 emission. The SO_2 that does not escape must therefore be absorbed in the preheater tower. It is known from other industries that Ca species are well suited for the absorption of SO_2. This chapter will outline the literature about SO_2 absorption by $CaCO_3$ and $Ca(OH)_2$. Besides Ca species, raw meal typical also contains other species that might be of interest to SO_2 absorption, so these will also be reviewed here.

5.1 SO_2 Absorption by $CaCO_3$

As mentioned earlier, Hansen [2] was able to predict sulphur oxidation in preheater cyclones satisfactorily by using his model. For the absorption of SO_2, he used a rate expression based on experiments with SO_2 absorption on raw meal. However, it turned out that the kinetic was too slow, predicting an emission of SO_2 that was at least twice that observed.
The Fresults for SO_2 absorption obtained by Hansen [2], when modelling the preheater tower, led Hu et al. [64] to review the reaction between limestone and SO_2. They found the reaction order for SO_2 to range from 0.4 to greater than 1, without any clear trend for this behaviour when compared to the reaction conditions. The reaction order of O_2 was found to be 0 at high concentrations (concentrations were not specified). In some cases CO_2 was reported to influence the $CaCO_3/SO_2$ reaction, while in others it was not noted. In addition to these findings, it was established that water influenced the reaction positively. Hu et al. [64] explained the deviating results as a lack of basic understanding of the reaction mechanism. This lack of knowledge is also evident in the apparent activation energy, which at low conversions is reported to be between 10 and 160 kJ/mol. The activation energy observed at higher conversions varied even more, ranging from negative values up to 400 kJ/mol. Some of the observed variations in the

activation energy might be explained by impurities in the naturally occurring limestones used for conducting experiments. Hu et al. [64] recorded a large number of different additives that have been shown to promote the sulphation reaction. The promoting additives are primarily chlorides and alkali metals, originating from different salts. The explanations for their promoting effect can be divided into three categories: the formation of crystal lattice defects, formation of eutectics and pore enlargement, which is only of importance if pore diffusion is significant. Lattice defects and the formation of eutectics are discussed intensively by Hu et al. [64], who state that the promoting effect of additives is related to increased solid-state diffusivity. They further emphasise that an increased solid-state diffusivity is counteracted by increased sintering, which will reduce the reaction rate. Of the 62 different potential eutectics that Hu et al. [64] present, only a very few would be of interest in relation to cement production, because most pyrite will be oxidised before the temperature of the eutectic melting points is reached.

From the data collected by Hu et al. [64] it is clear that an increased surface area also results in a higher sulphation rate, which shows that the controlling mechanism is related to the interface between the gas phase and the interior of the particles used for the reaction. The product layer formed at higher degrees of conversions is porous, despite the larger molar volume of $CaSO_4$ compared to the initial molar volume of $CaCO_3$. The porous product layer is often explained by an outward flow of CO_2; however, according to Hu et al. [64], this explanation is questionable due to the net inward flow of gas.

The modelling of the $SO_2/CaCO_3$ reaction is also treated by Hu et al. [64]. The intrinsic reaction rate is often modelled as an n'th order reaction with respect to SO_2, incorporating the dependency of O_2 and other species into the rate constant. Hu et al. [64] do not mention that the rate constants, estimated by different authors, most often are based on data obtained when the intrinsic reaction must be considered completed. At higher conversions it is common to model the $SO_2/CaCO_3$ reaction with an unreacted shrinking-core model, with the limiting step being solid-state diffusion, indicated by the effective diffusion coefficient of 10^{-9} to 10^{-10} m^2/s at 850 °C, which is within the range normally observed for solid-state diffusion [65].

From the review by Hu et al. [64] it is clear that even though the $SO_2/CaCO_3$ reaction has been studied intensively over the years, the basic reaction mechanisms are still not well understood. In order to deal with this issue, Hu et al. [66–69] investigated the $SO_2/CaCO_3$ reaction at reaction times smaller than 1 second. They also carried out experiments at longer reaction times in order to study the initial period of $CaSO_4$ crystal growth. When studying the intrinsic kinetics they found that increasing SO_2 concentration increased the conversion rate, while CO_2 had the opposite effect. No effect of O_2 was observed. Hu et al. [68] suggested a new model for the intrinsic reaction, based on their results obtained at reaction times shorter than 1 second.

In experiments where a crystal growing phase was observed, the authors found that chlorides and alkali metal salts were able to increase the sulphation rate six to eight times compared to limestone without additives.

Experiments carried out in the crystal growth phase with three different limestones showed that the reaction order of SO_2 was about 0.2 in a dry atmosphere, while the addition of 7.5 % water increased the reaction order to 0.4. This is in accordance with the results obtained by other authors. Identical results for the reaction order of O_2 were observed. At O_2 contractions above 15 % the reaction order became 0. They found the reaction order of CO_2 to be -0.5, while no order for water was given, but a promoting effect was observed on the reaction order of O_2 and SO_2. Hu et al. [67] found the apparent activation energy to be around 100 kJ/mol. Based on these findings a new model [67] at long reaction times was proposed instead of the unreacted shrinking core model often used in literature.

5.2 Ca(OH)$_2$-SO$_2$-CO$_2$

By far most of the work carried out in relation to the $Ca(OH)_2/SO_2$ reaction was done below 100 °C [70–78]. This temperature is well below the exhaust gas temperature of approximately 300 °C observed in modern preheater towers. This literature survey of the reaction between $Ca(OH)_2$ and SO_2/CO_2 does not include these results, the main reason for which is that below 100 °C liquid water will affect the results.

In absorption experiments carried out by Bueno-Lopez and Garcia-Garcia [79] it was observed that the absorption capacity of $Ca(OH)_2$ was significantly higher at and above 450 °C than at 250 and 350 °C. The explanation given was that at 450 °C the reactant CaO was more reactive due to a larger surface area than in the parent $Ca(OH)_2$, which was the reactant at lower temperatures. The results obtained by Gorkem and Oguz [80] confirm this.
Yamamoto et al. [81] observed a characteristic two-stage reaction with a fast initial stage and a slow second stage. The second stage conversion being so slow that it can be considered a maximum conversion level. This behaviour was also observed by other authors [82, 83] conducting experiments below the decomposition temperature for $Ca(OH)_2$.
Experiments with different dopants were conducted at 350 °C by Yamamoto et al. [81], who found that neither Fe^{3+} nor chlorides improved the reaction; only NO^{3-} was found to promote the reaction. Also, NO and NO_2 have been found to promote the $Ca(OH)_2/SO_2$ reaction, which was explained by NO and NO_2 inhibiting the negative effect of CO_2 [84].
Li et al. [85] found a higher conversion of $Ca(OH)_2$ both below and above the decomposition temperature compared to the parent CaO. The explanation for this phenomenon was a larger surface area/pore volume of the $Ca(OH)_2$ sorbent.
In a CO_2-free atmosphere between 350 and 450 °C a higher temperature shows a positive influence on the conversion obtained after 1 hour of reaction [86]. In an atmosphere containing 12 % CO_2 Matsushima et al. [84]observed an optimum temperature at 350 °C, when studying the $Ca(OH)_2/SO_2$ reaction between 320 and 380 °C. The negative influence of CO_2 on the conver-

Component	Component to sulphur ratio
	mol/mol
CaO	48-501
SiO_2	16-162
Al_2O_3	2.6-27
Fe_2O_3	1.1-12
MgO	4.3-45
K_2O	0.7-7.5
Na_2O	0.2-2.1
Mn_2O_3	0.2-1.7
TiO_2	0.3-2.6
P_2O_5	0.1-0.8

Table 5.1: *Ratio between major species and sulphur in the clinker product. The values are based on the mass fractions given in Table 2.1, where the interval stated in this table is the largest value for the component divided by the range for sulphur stated in Table 2.1.*

sion was also observed by Fernandez et al. [86], who noted a smaller conversion at 350 °C when adding CO_2 to the reaction gas. Tseng et al. [82] stated that the initial reaction rate increases with increasing SO_2 concentration. However, in their paper this behaviour is difficult to see, and it appears that the initial rate is constant or even decreases with increased SO_2 concentration. Other authors [80] have only seen a small dependency of SO_2 concentration. The reaction product was reported [85, 86] as a mixture of $CaSO_3$ and $CaSO_4$ when oxygen is present. Fernandez et al. [86] did not observe any difference in the conversion obtained after one hour, conducting experiments with and without water at 350 and 450 °C.
Fernandez et al. [86] modelled their results using an exponential model to describe their breakthrough curves. The model took the negative effect of CO_2 into account. The temperature dependency of their model parameters did not fit an Arrhenius expression, which is why they fit the temperature dependency to an empirical expression.

5.3 SO_2 Absorption by Non-Calcium Containing Species

Table 5.1 highlights the molar ratio between major species in the clinker product and the sulphur content in the clinker product. Of the components shown in Table 5.1, CaO and its precursors ($CaCO_3$/$Ca(OH)_2$) are treated elsewhere. Ca species have naturally attained a lot of attention in understanding SO_2 absorption in preheater towers. However, other species might also be of interest if they are highly reactive towards SO_2 at the temperatures found in the top stages of a preheater tower. In order for these to have any significant impact, besides a potentially catalysing effect, a given component must be in reasonable excess and in a combination that

is reactive towards SO_2. The criterion of reasonable excess leads to the conclusion that manganese, titanium and phosphorous species do not significantly influence SO_2 absorption. Silica, aluminium and iron are found in a great variety of naturally occurring minerals, where magnesium, potassium and sodium can be incorporated as impurities in the crystal lattice [87,88]. The very large variation in makes it difficult to state anything general about these minerals. However, silicon oxides are normally considered inert in relation to SO_2 [89]. The reaction between SO_2 and the different minerals is a gas-solid reaction, and an indication for reactivity is the surface area of the mineral species, since a potential reaction has to proceed at or through the solid material surface. However, the surface areas for non-Ca species are highly dependent on the mineral, with values ranging from 10-360 m^2/g [87] making it difficult to state anything based on the surface area. The ability of some pure varieties, such as Fe_2O_3 and $NaHCO_3/Na_2CO_3$, to absorb SO_2 has been studied in the literature [90, 91], which found that SO_2 absorption took place with all species, even though the absorbed amount was low. Carbonate compounds such as Na_2CO_3 are of particular interest, since they would potentially be unaffected by the high CO_2 partial pressure found in the preheater tower. In this respect especially, magnesium carbonate is of interest, because it is an impurity in limestone or bound in dolomite, and a considerable amount of excess compared to sulphur might be present. Furthermore, $MgCO_3$ behaves like $CaCO_3$ (from a chemical point of view), with the calcination of $MgCO_3$ starting at about 430 °C [92] under the conditions present in a preheater tower. The sulphation of dolomite has been studied by different researchers [93–99], who observed a sulphation behaviour similar to that of limestone. Kaljuvee et al. [98, 99] found that CaO had a greater reactivity than dolomite. From their results it is evident that dolomite is more reactive towards SO_2 at 500 °C than limestone, but the difference is small. Regarding the reaction product, no authors have reported the formation $MgSO_3/MgSO_4$, not even at low temperatures where the reaction product is $CaMg_3(SO_4)_4$ [99]. Experiments carried out using pure MgO [100, 101] have shown that MgO does not react with SO_2 at temperatures below 625 °C, which also explain why $MgSO_3/MgSO_4$ are not observed in experiments with dolomite. That MgO seems to be inert towards SO_2 at low temperatures rules it out as a significant species for SO_2 absorption in preheater towers.

Based on the literature findings it must be concluded that only Ca species make a significant contribution to SO_2 absorption in the top stages of a preheater tower, with other species only exhibiting a catalytic effect.

Chapter 6

CaO Reactions

This chapter will focus on CaO reactions that take place in the top stages of the preheater tower, including the reaction between CaO and SO_2 and between CaO and CO_2. These reactions are of interest in order to understand the processes that influence the absorption of SO_2 in the top stages of the preheater tower. Furthermore, CaO has the potential of being a cheap solution for dealing with SO_2 emission. Literature approaches to model these reactions will also be reviewed in this chapter.

6.1 Reactions Between CaO-SO_2-CO_2

Reaction Time

The influence of reaction time upon the CaO/SO_2 reaction in a CO_2-free atmosphere was studied by a number of authors [102–107], with reaction times ranging from a few seconds up to hours. As the reaction time increased, the conversion of CaO also increased. The results obtained by Borgwardt and Bruce [105] show that the reaction is very fast in the initial period. In their case, two-thirds of the total conversion took place within the first 35 s, while a reaction time of 1000 seconds or more was required in order to obtain the maximum conversion. What in literature is referred to as the maximum conversion is always smaller than 1, because the conversion reaches a level from which it only increases very slowly. This level is explained by blockage of the pore system, due to the larger molar volume of the reaction product. That the conversion levels off when the pore system blocks is seen from the results presented by Gulllett and Bruce [108], who measured how the pore system developed as a function of conversion. From their results it is clear that the conversion rate decreases strongly when the pore system blocks.

Temperature

The temperature influence on the CaO/SO_2 reaction was investigated by Borgwardt and Bruce [105] using CaO particles smaller than 2 μm, with a surface area of 3 m^2/g in a temperature in-

terval from 800-1125 °C. Their results show that the conversion increase with temperature was as would be expected. The positive effect of increasing temperature was also experienced by Milne et al. [109] and Shi and Xu [110]. However, other authors [102, 107] observed that the effect of temperature upon the final conversion levels off or is even negative at about 1000 °C. The reason why these studies did not observe a continuously increasing effect of temperature is most likely due to sintering of the CaO particles used, because sintering is known to take place well below 1000 °C. The negative effect of sintering is avoided in the experiments by Borgwardt and Bruce [105], because their particles are heavily sintered before reaction with SO_2. In one study [111] the conversion was temperature-independent; however, the authors were able to explain the missing temperature dependency through large differences in CaO surface areas.

Surface Area

The effect of surface area was investigated by Borgwardt and Bruce [105] using CaO particles with a surface area between 2.1 m^2/g and 63 m^2/g. They found that the conversion increased by increasing the surface area, for both short and long reaction times. The positive effect of increased surface area was also reported in other publications [109, 111]. The reason in the literature for the positive effect of increasing the surface area is that the reaction is limited either by the initial reaction between CaO and SO_2 or by diffusion through the solid product layer formed. Nonetheless, if the particles are large enough [102], the limiting step will be pore diffusion and the conversion will be independent of the internal surface area.

SO_2 Concentration

One method used in the literature [103] to determine if pore diffusion was present was to evaluate the reaction order of SO_2. If pore diffusion was exclusively rate determining, a reaction order of one would be expected. Researchers [105,112,113] who had been using very small particles in order to eliminate pore diffusion observed that the reaction order with respect to SO_2 was lower than unity and was in the range from 0.49 up to a value of 0.7, with most of the values at about 0.6. In the paper written by Yang et al. [113] the reaction order obtained using a pure $CaCO_3$ source as a precursor was 0.59, while the addition of Fe_2O_3 increased the reaction order to 0.62. This difference was attributed to the catalytic oxidation of SO_2 to SO_3, although no effect was seen when using V_2O_5, which is known to be a strong catalyst for high-temperature oxidation. In their experiments with V_2O_5 and Fe_2O_3 Borgwardt et al. [112] did not find any effect when adding these compounds, which is why they excluded a catalytic effect. It should be noted that Borgwardt et al. [112] found the reaction order to be independent of whether the CaO precursor was $CaCO_3$ or $Ca(OH)_2$.

CaO Precursor

A number of authors [54, 108, 108, 111, 112] have tried to compare the two most common pre-

cursors for CaO, namely $CaCO_3$ and $Ca(OH)_2$. The results from Shih et al. [111] show (they do not comment on it) that the CaO derived from both precursors behaves identically, both for long and short time experiments, which in their case means one hour and 80 s, respectively. Borgwardt et al. [112] conclude that the intrinsic kinetics is independent of the precursor used for forming CaO. Bruce et al. [54] find that, at 1000 °C, CaO derived from $Ca(OH)_2$ has a higher conversion, but their data actually shows that the initial conversion observed is the same, which is why it can be derived from their results that CaO originating from $CaCO_3$ might sinter easier, perhaps due to a difference in its crystal structure (see section 4.3). Gullett and Bruce [108] compared CaO with a large surface area derived from $CaCO_3$ and $Ca(OH)_2$. Up to a conversion of 45%, they found no significant deviations between the two calcium oxides. At higher conversions they observed that a larger conversion for CaO derived from $Ca(OH)_2$ was possible, which they ascribed to the slit pore structure formed in CaO originating from $Ca(OH)_2$. The slit pores, they stated, allows for larger particle expansion than the pore structure formed when calcining $CaCO_3$.

Reaction Product and the Influence of O_2

The reaction between CaO and SO_2 can produce different products, depending on the temperature and atmosphere where the reaction takes place. Munoz-Guillena et al. [114,115] studied the reaction products formed when the reaction takes place within pure He or in a He atmosphere containing 5 vol% oxygen. They suggested that reaction 6.1-6.4 could take place depending on the available conditions.

$$CaO(s) + SO_2(g) \rightleftarrows CaSO_3(s) \tag{6.1}$$

$$CaSO_3(s) + 1/2O_2(g) \rightleftarrows CaSO_4(s) \tag{6.2}$$

$$4CaSO_3(s) \rightleftarrows 3CaSO_4(s) + CaS(s) \tag{6.3}$$

$$CaS(s) + 2O_2(g) \rightleftarrows CaSO_4(s) \tag{6.4}$$

When using a pure He atmosphere they found that up to 700 °C the product formed was $CaSO_3$. Above 700 °C they observed a decrease in CaO conversion. Above 777 °C the conversion started to increase again, which Munoz-Guillena et al. [114] explained by the formation of $CaSO_4$ and CaS according to equation 6.3. X-ray diffraction confirmed that only $CaSO_3$ was formed below 700 °C.

Using an atmosphere containing oxygen, Munoz-Guillena et al. [115] observed that only a small amount of oxygen was consumed at temperatures below 500 °C. Moreover, they observed that

SO_2 retention increased continuously with temperature without a decrease at 700 °C, as was observed using a pure He atmosphere. This was explained by $CaSO_3$ not disproportionating but being oxidised to $CaSO_4$, which in the experiments carried out by Munoz-Guillena et al. [115] did not decompose below 1287 °C. The products were investigated by X-ray diffraction, which showed that between 500 and 700 °C the product was a mixture of $CaSO_4$ and $CaSO_3$, while no $CaSO_4$ was found below 500 °. Above 700 °C, $CaSO_4$ was the only product.
Some authors [85, 116–119] have used IR spectroscopy in order to study the reaction products of the CaO/SO_2 reaction. In an oxygen-free atmosphere between 600 and 900 °C Allen and Hayhurst [119] observed the formation of $CaSO_4$, CaS and $CaSO_3$ up to 800 °C, whereas only $CaSO_4$ and CaS were formed above. Ghardashkhani and Cooper [118] observed the same products. Li and Sadakata [85] studied the products from the sulphation reaction in an oxygen-free atmosphere, finding both $CaSO_4$, CaS and $CaSO_3$. In addition, they found, below 450 °C, that the products were the same when adding O_2. When adding Al_2O_3 to the process, the oxidation of $CaSO_3$ and CaS to $CaSO_4$ was facilitated. That oxidation of $CaSO_3$ could be promoted by other species was also found by Ishizuka et al. [117], who found that NO had a promoting effect at 150 °C. Low et al. [116] studied the CaO/SO_2 reaction in both a vacuum and an oxygen atmosphere up to 750 °C. At low temperatures only $CaSO_3$ was formed, and up to 500 °C no significant changes in the IR-spectras were observed. At 550 °C the disproportionation of $CaSO_3$ into $CaSO_4$ and CaS started. Low et al. [116] also saw peaks that could not be accounted for, but when treating the samples with O_2 at 750 °C these bands vanished. The authors explained this phenomenon as the oxidation of species of the general form ${S_yO_x}^{-n}$ to ${SO_4}^{2-}$.
Allen and Hayhurst [119] studied the effect of oxygen between 600 and 900 °C, finding the reaction order of oxygen to be zero, from which they concluded that the sulphation reaction proceeds through reaction 6.1 without oxidation of SO_2 to SO_3 in the gas phase as an intermediate. The zero-order reaction kinetic with respect to oxygen is supported by other authors [93, 120], too, both of whom carried out experiments in an atmosphere containing CO_2.
When comparing the oxygen reaction order to the reaction product observations, it is reasonable to assume that the CaO/SO_2 reaction proceeds through reaction 6.1 with subsequent oxidation to $CaSO_4$, if the conditions are favourable for oxidation.

Influence of Water

Dennis and Hayhurst [121] investigated the influence of water vapour in the gas phase, but did not find any effect with water contents between 0 and 7 %.

Influence of Impurities

Borgwardt et al. [112] compared CaO, based on naturally occurring limestones to CaO, based on pure $CaCO_3$, and found that CaO originating from a naturally occurring limestone reached a higher conversion due to lattice defects. This was further investigated by grinding alkali(Li, Na,

K) sulphates with CaO before reaction with SO_2. The authors observed an improved reactivity towards SO_2, while no effect was seen when adding the alkali sulphates before calcination. They attributed the missing effect to a rapid decrease in surface area during the calcination process and observed a surface area 16 times smaller when adding alkali sulphates before calcination. No effect was forthcoming by adding Fe_2O_3 and V_2O_5. Shi and Xu [110, 122] found that the conversion could be promoted by adding fly ash to CaO. It was explained by adherence of small CaO particles to the fly ash surface. Stouffer and Yoon [123] found a positive effect of adding up to 2 wt% of Na_2CO_3 to limestone before calcination. The positive effect was explained by an increase in pore diameter caused by more pronounced sintering, which should prevent the pore mouth blocking and make pore diffusion easier. They conducted their experiments in 15 % CO_2 and observed a small effect when adding NaCl, but no effect when adding $CaCl_2$ and $FeCl_3$. Yang et al. [113] determined that 4 wt% Fe_2O_3 increased conversion, while V_2O_5 did not achieve the same result. When adding 19 wt% of fly ash, which resulted in 4 wt% Fe_2O_3 content, they saw the same effect as when adding 4 wt% of Fe_2O_3. The authors concluded that Fe_2O_3 might be the only effective additive in the fly ash they were using.
Partanen et al. [124] studied the simultaneous absorption of SO_2 and HCl, deducing that when HCl is present in the gas, SO_2 absorption increases, even when carbonisation takes place simultaneously. They cited the formation of a melted phase in the CaO particles, when reacted with HCl as the reason for their finding. Wang et al. also found that up to 2 wt% of Na_2CO_3 had a promoting effect on the CaO/SO_2 reaction, but the non-doped CaO showed a larger conversion in the first 30 minutes of reaction. They suggested that cations with valency other than Ca^{2+} and approximately the same ion radius should be efficient in promoting the CaO/SO_2 reaction, because these ions can form lattice defects through which the reaction can proceed. They showed that both the sulphates and carbonates of Li, Na and K promoted the reaction, but they did not show any non-promoting species.

Influence of CO_2 on the CaO-SO_2 Reaction

Hartman and Trnka [125] studied the CaO/SO_2 reaction between 170 and 580 °C using either 0 or 10% CO_2. When exposing the CaO to SO_2 for two hours, it was not possible to observe any difference in the absorption between the CO_2 and non-CO_2-containing atmosphere. When comparing the ability of CaO to absorb SO_2, H_2O and CO_2 they found that SO_2 absorption was not affected by the presence of water and that SO_2 absorption increased by increasing the temperature. The CO_2 absorption increased with temperature when no SO_2 was present, while with SO_2 the CO_2 absorption reached maximum at 520 °C. When investigating the effect of reaction time they found no difference between a CO_2 and a non-CO_2 containing atmosphere. Tullin and Ljungstrom [106] performed sulphation/carbonisation experiments in a TGA. In their experiments with simultaneous carbonisation and sulphation, they observed a large uptake of CO_2 in the first 15 minutes, after which the conversion with respect to CO_2 started to decrease.

The conversion with respect to SO_2 increased continuously during the 180-minute experiment, and no difference in sulphation was seen between a CO_2 and a non-CO_2-containing atmosphere. Iisa et al. [126] continued the work of Tullin and Ljungstrom [106] by observing the same trends. Borgwardt [103] investigated CaO derived from four different limestones using an atmosphere containing 10.5 % of CO_2. The temperature interval was 540 to 980 °C. It was only at the lowest temperature that the author observed an influence of CO_2 upon the sulphation reaction. Suyadal and Oguz [127] found that, in a 10 % CO_2 atmosphere, the CaO conversion with respect to SO_2 continuously increased between 200 and 900 °C. They also evaluated a reaction order of 0.7 at temperatures up to 500 °C, while the reaction order from 600 °C to 900 was 1.

6.2 Modelling of the CaO-SO_2 Reaction

A wide range of authors [54, 103–105, 111, 112, 119, 126, 128–132] have proposed models for the CaO/SO_2 reaction under various conditions, basically building on the work done by Levenspiel [133]. Here, the detailed aspects of the various models will be left out, with a focus on the general trends in the different modelling approaches. Figure 6.1 shows the general steps in the CaO/SO_2 reaction and illustrates the non-porous crystals of CaO. When t equals 0 the reaction has not yet started, and the surface of the crystals is in contact with the surrounding gas phase. Shortly after the reaction has started at $t \approx 0$ a thin layer of $CaSO_4/CaSO_3$ forms at the surface. In this initial step, it is, according to Wang et al. [134], generally accepted that the limiting step is the chemical reaction between CaO and SO_2 if pore and/or film diffusion are negligible. Some authors [111, 129] include this initial step in their modelling approach, whereas others [54, 112] omit it. However, even though it should be commonly recognised that the initial rate should be governed by the chemical reaction,it has not been possible to find any literature data that confirms this. Shih et al. [111] summarised values for the initial rate constant, finding values ranging from $2.6 \cdot 10^{-4}$ - $6.6 \cdot 10^{-2}$ m/s in a temperature interval from 750 to 980 °C. No regular tendency between these values is observed. When t opposes tau, there is consensus in the literature that the rate determining step is solid-state diffusion of SO_2 in the product, if pore and/or film diffusion are negligible. However, a wide range of modelling approaches have been introduced in order to account for the expanding product layer [130], as well as sintering phenomena [128]. When modelling solid-state diffusion it is common to assume that the reaction takes place at the $CaSO_4/CaO$ interface, as proposed by Bhatia and Perlmutter [129], meaning that the diffusing species are sulphur oxides. However, Hsia et al. [135, 136] found at 1300 °C, through the use of isotopes, that CaO was diffusing from the $CaO/CaSO_4$ interface to the $CaSO_4$/gas interface, where it reacted with SO_2 and oxygen. That the controlling mechanism, should be the diffusion of CaO in the product layer does not correspond with a reaction order of SO_2 different from zero.

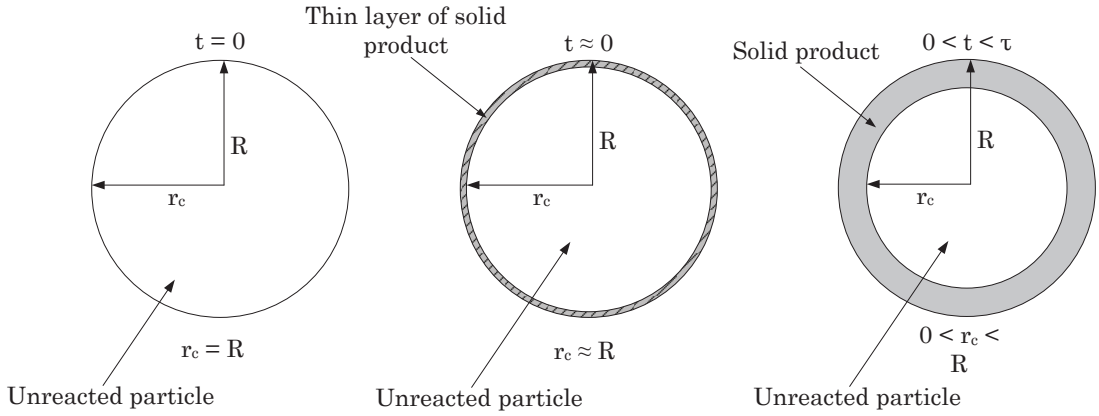

Figure 6.1: *Steps in modelling the CaO/SO_2 reaction.*

The temperature dependency of the solid-state diffusion coefficient is often modelled by an Arrhinus expression. Table 6.1 summarises the literature values for the pre-exponential factor and activation energy. The values for $D_{SO_2,s}$ at 800 °C show that the process is a solid-state diffusion process, since the values correspond to those found in the literature [65] for solid-state diffusion. Furthermore, they are significantly higher than what is typically observed for gas diffusion ($\approx 10^{-6}$) [65]. The values of both E_a and D_0 show that they depend strongly on the model and material used for fitting data. This is, amongst other things, seen from the two different values for E_a obtained by Milne et al. [130] and Borgwardt and Bruce [105] using the same data but different models, as well as the results produced by Shih et al. [111] using different materials.

Author	D_0	E_a	$D_{SO_2,s}$(800 °C)	Data
	m^2/s	kJ/mol	m^2/s	
Shih et al. [111]	$5.6{\cdot}10^{-9}$-$3.6{\cdot}10^{-6}$	80-137	$7.14{\cdot}10^{-13}$-$7.7{\cdot}10^{-13}$	own
Bhatia and Perlmutter [129]	$3.9{\cdot}10^{-6}$	120	$5.6{\cdot}10^{-12}$	Reference [103]
Marsh and Ulrichson [104]	$1.8{\cdot}10^{-6}$	149	$1{\cdot}10^{-11}$	own
Milne et al. [130]	$4.1{\cdot}10^{-9}$	107	$2.7{\cdot}10^{-14}$	Reference [105]
Borgwardt et al. [112]	$1.2{\cdot}10^{-5}$	138	$2.3{\cdot}10^{-12}$	own
Borgwardt and Bruce [105]	N.A.	153	N.A.	own

Table 6.1: *Literature values for calculating the diffusion coefficient for solid-state diffusion in the CaO/SO_2 reaction.*

6.3 Reaction Between CaO and CO_2

Reaction time

The CaO/CO_2 reaction is also observed [137–142] as a two-stage reaction with a fast initial stage

and a slow second stage, referred to as the maximum conversion, which is smaller than one. The explanation for the observed maximum conversion is pore blockage due to the larger molar volume of $CaCO_3$ compared to CaO. However, some authors [137,140] ascribe this maximum level to the formation of a critical product layer which marks the onset of solid-state diffusion and should be responsible for the very slow conversion rate observed when approaching maximum conversion. However, experiments [139] on nano-sized CaO crystals, which were smaller than the critical product layer, showed the same behaviour as observed for larger particles, questioning the idea of a critical product layer. Two of the very few authors who have studied the carbonisation reaction at residence times less than 1 minute are Bhatia and Perlmutter [142]. They observed a sigmoid-shaped conversion curve comprising, according to the authors, the following three stages of reaction: initial nucleation, rapid reaction and then a slower second stage reaction. However, although their results appear as if they might be limited by gas phase diffusion, it is evident that the initial reaction is very fast, with an observed conversion of 50 % or more in less than 1 minute. Other authors [137,139,141] observed that the maximum conversion was obtained within 5 minutes, with most of the carbonisation taking place during the first minute or two. Sun et al. [143] observed a conversion above 50 % within 15 s at 700 °C.

Temperature

Symonds et al. [144] studied the effect of temperature on the carbonisation reaction, establishing that maximum conversion was independent of temperature between 580-700 °C. Gupta and Fan [145] and Bhatia and Perlmutter [142] observed that the maximum conversion increased with increasing temperature in the interval from 400 to 650 °C. Several authors [142–144,146,147] reported the carbonisation reaction rate increased with temperature. The activation energies obtained from the different studies range from about 30 kJ/mol up to about 240 kJ/mol. A part of this discrepancy is most likely caused by the lack of a reaction mechanism/model for the reaction itself. Dedman and Owen [148] observed a higher maximum conversion as well as a faster reaction rate when increasing the temperature. Their experiments were conducted between 100 and 600 °C.

CO_2 Concentration

Sun et al. [143] found the reaction order with respect to CO_2 to be zero order when the partial pressure of CO_2 was about 0.1 atm higher than the equilibrium pressure. When the difference was smaller than 0.1 atm the reaction was observed to be first order in CO_2. For CO_2 partial pressures above 0.2 atm, Kyaw et al. [146] found the carbonisation reaction to be zero order between 400 and 800 °C. The zero-order kinetic was also observed by Bhatia and Perlmutter [142], who stated that it is only when close to the equilibrium concentration of CO_2 that the reaction order should be different from zero. Oakeson and Cutler [149] observed that the effect of CO_2 levelled off when the partial pressure became significantly higher than the equilibrium pressure.

Dedman and Owen [148] also observed a reaction order of zero for CO_2, while Mess et al. [147] found that the reaction order of CO_2 was not fixed at 850 °C, at long reaction times and above 900 °C they found the reaction order to be first order.

CaO Precursor

When comparing different CaO precursors, Gupta and Fan [145] did not find any relation between the precursor and the observed conversion rates. The naturally occurring limestone showed the lowest value for the maximum conversion.

Surface Area

Bhatia and Perlmutter [142] observed an increased conversion rate with increased internal surface area. Barker [140] found that, after the initial period of carbonisation, the surface area was similar to that of the $CaCO_3$ precursor and more than 70 times smaller than the surface area of the CaO starting material. This difference in surface area clearly indicates that pore plugging occurs when carbonisation takes place. Some authors [137, 150] studied the reaction in calcination/carbonisation cycles, and it is evident that conversion is related to the surface area of the used CaO.

Water

The possibility of improving carbonisation by hydrating CaO, followed by decomposition of the formed $Ca(OH)_2$, has shown that CaO originating from $Ca(OH)_2$ is more reactive towards CO_2 [151–153]. Sun et al. [153] found that the gas phase concentration of water did not affect the carbonisation reaction.

Impurities

Symonds et al. [144] found that CO and H_2 in the gas phase promoted the reaction rate, which occurred through the formation of more CO_2 at the solid/gas interface due to the water-gas shift reaction. Manovic and Anthony [152] found in their cyclic calcination/carbonisation experiments that Na_2CO_3 promoted carbonisation in the first couple of cycles. The effect was explained by enhanced product layer diffusion, which was counteracted by sintering when the number of cycles increased. Al_2O_3 showed the opposite effect as a dopant. The authors also found that CaO derived from natural limestones exhibited different behaviours with respect to CO_2 absorption, which they ascribed to differences in impurities. In fluidised bed experiments, Salvador et al. [154] observed that both Na_2CO_3 and NaCl had a negative effect on the carbonisation process, while in TGA experiments only NaCl had a negative influence. Sun et al. [143] investigated a wide range of additives, finding that only Al_2O_3 had a substantially promoting effect, while chlorides especially showed a negative effect, which was most likely due to sintering of the used CaO.

models

Sun et al. [143] assumed that the reaction is the limiting step. Based on this model they estimated an activation energy of 29 kJ/mole independent of the reaction order of CO_2. Kyaw et al. [146] used the same model as Sun et al. [143], obtaining an activation energy of 78 kJ/mole. Bhatia and Perlmutter [142] found, for the fast initial reaction between CaO and CO_2, that the activation energy should be 0, based on measurements between 550 and 725 °C. Barker [140] supported this for temperatures up to 900 °C. At higher conversions they assumed solid-state diffusion in the product layer to be rate determining, observing that below 515 °C the activation energy was 89 kJ/mole and above this temperature the value abruptly increased to 179 kJ/mole. Based on the observed change in activation energy, Bhatia and Perlmutter suggested a reaction mechanism where CO_3^{2-}/O^{2-} was the diffusing species. Diffusion of these species in the product layer is also suggested by Oakeson and Cutler [149], who found an activation energy of 121 kJ/mole for solid-state diffusion. Dedman and Owen [148] estimated an activation energy of 40 kJ/mole for solid-state diffusion, while Mess et al. [147] estimated the activation energy to be 238 kJ/mole.

Chapter 7

Literature Summary

The previous chapters outlined modern cement production and potential SO_2 emission problems, as well as candidates for SO_2 absorption, with a special focus on calcium-containing species. The most common way to produce Portland cement today is by using the dry process, which is preferred because it is less energy-intensive compared to other methods. The kiln system in the dry process is made up of a preheater tower, a rotary kiln and a clinker cooler. SO_2 emission from this kiln system originates exclusively from the oxidation of sulphur compounds in the top cyclones of the preheater tower. At the temperatures found in the top stages, the raw meal is only capable of absorbing about 50 % of the formed SO_2, which in practice can lead to emission problems. In order to handle emission problems a number of methods which integrate the emission reduction into the plant have been patented, but none of these has turned out to be as efficient as a separate desulphurisation unit.

In the literature, several approaches to modelling the preheater tower have been published, and it has been possible to model the formation of SO_2 in the top stages well. However, modelling the absorption of SO_2 in the preheater satisfactorily has not yet been possible. Based on the literature review concerning non-calcium species' capability to absorb SO_2, it is concluded that these species do not contribute significantly to the absorption of SO_2, which is why calcium species must be considered the main absorbents for SO_2. The calcium species that are of interest in relation to SO_2 absorption are $CaCO_3$, CaO and $Ca(OH)_2$. Especially $CaCO_3$ and CaO are of interest when modelling the absorption of SO_2 in the preheater tower, since 75 w/w % of the raw meal is $CaCO_3$ and CaO, which recirculates inside the preheater tower, is believed to contribute significantly to SO_2 absorption. However, in order to model the absorption processes of these species it is necessary to understand the initial kinetics for the reactions at relevant conditions. When reviewing the literature the amount of relevant data for the initial kinetic is extremely limited for the $CaCO_3/SO_2$ reaction, and non-existent for the CaO/SO_2 reaction, at least when CO_2 is present in the gas phase. The limited amount of data concerning the initial kinetic for these two essential reactions shows clearly the need for data and relevant kinetic modelling in order to be able to estimate SO_2 absorption in the preheater tower. Although $Ca(OH)_2$ is not

naturally present in the top stages of the preheater tower, it has attracted a considerable amount of attention in relation to dealing with SO_2 emission. However, at temperatures above 100 °C little work has been done in connection with the ability of $Ca(OH)_2$ to absorb SO_2. In order to use the full potential of this compound dealing with SO_2 emissions, data and knowledge about this compound's capability to absorb SO_2 in a CO_2-containing atmosphere is required.

Chapter 8

Set-ups, Experiments and Materials

The experimental work conducted in this thesis focuses on the reaction between CaO/SO_2 at reaction times shorter than 1 second. In order to achieve this an entrained flow reactor, where it is possible to obtain these short reaction times, was utilised. From the literature it is known that large surface areas result in higher conversion rates for the CaO/SO_2 reaction. In order to obtain large surface areas a number of different methods for the calcination of $CaCO_3$ were attempted. This chapter outlines the experimental equipment along with the experimental procedures. Furthermore, the utilised materials are described here.

8.1 Entrained Flow Reactor

Figure 8.1 shows a schematic drawing of the entrained flow reactor used for studying the reaction between different calcium-containing species and SO_2/CO_2. The reactor consists of a 14.95 m long tube of Fe-Cr-Ni-based high temperature-resistant alloy. It is possible to inject SO_2 and CO_2 at four different points, marked V1-V4. The reactor tube is located horizontally in the oven, with a slope downwards of 1°, and it contains seven U-bends in order to fit into the oven. The pipes for injecting SO_2 and CO_2 are dimensioned in order to ensure that the gases have reached the reactor temperature when injected. The reactor oven is electrically heated and controlled by a thermostat, which ensures a constant reactor temperature. An electrical preheater is used for preheating the main gases, which are nitrogen or compressed air. If conducting experiments with a wet gas, steam is added to the main gas before it enters the preheater. Solid material is then fed from the loss in weight particle feeder, which is situated in an airtight bin. Blockage of the feeding string is avoided by letting nitrogen through the particle feeder. The use of nitrogen to facilitate the feeding of solid material ensures an inert atmosphere around the particle feeder. Preheated gas and solid material are mixed before entering the reactor oven. In the reactor oven, gas and solid material are brought up to reactor temperature, before SO_2 and CO_2 are injected. Just before the reactor outlet, about 2 % of the gas is sampled for analysis. When collecting gas for analysis the set-up does not discriminate between gas and solid material, which is why it is

necessary to separate solid material and gas outside the reactor oven by using a filter, which is heated in order to ensure that water does not condense. In the reactor outlet the remaining solid material and gas are separated and the gas is discarded while the solid material is collected in a particle container for further analysis. Temperature and pressure are measured at the places marked T and P, respectively. All gas flows to the reactor are controlled by mass flow controllers. The set-up is evaluated in Appendix A. In the evaluation it was found, based on experiments, that the gas sampling method and the injection of solid material do not influence the observed results. It is further concluded that the reactor can be considered isothermal. A thorough literature-based analysis of the reactor tube configuration has led to the conclusion that it is reasonable to assume that particles follow the gas flow.

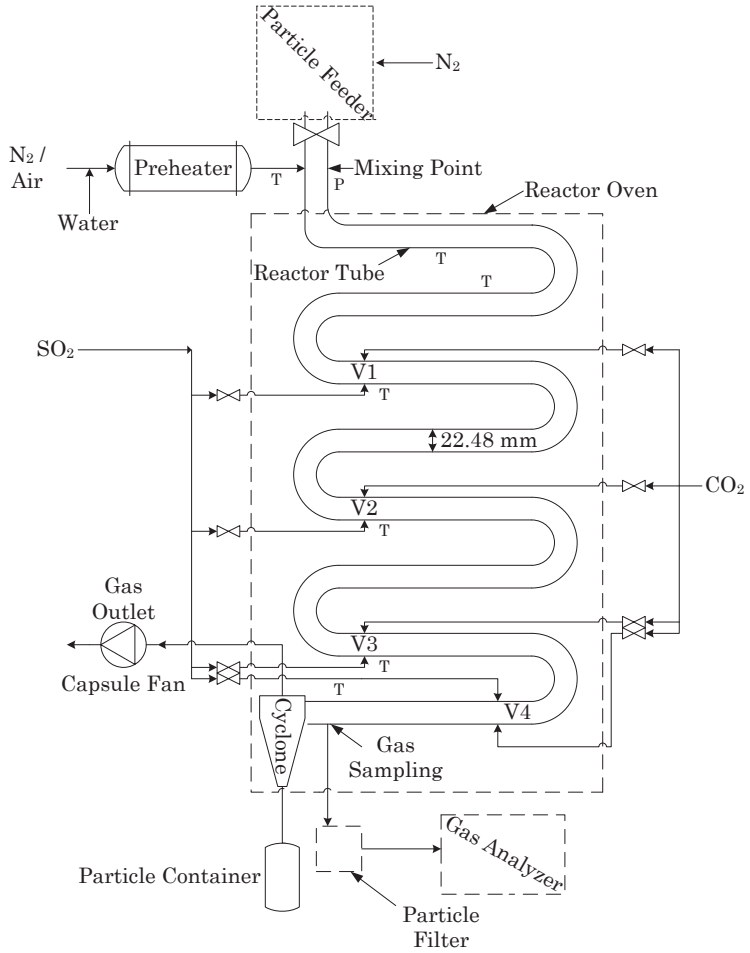

Figure 8.1: *Sketch of the entrained flow reactor used for studying the reactions between calcium-containing species and SO_2/CO_2.*

8.2 Experimental Procedure

Initially, the reactor temperature is allowed to stabilise. Next, the main gas is supplied and the preheater temperature adjusted, so that the reactor tube is isothermal from V1 and forward. Then CO_2 and SO_2 are added to the reactor through one of the inlet valves V1-V4; the valve used depends on the required reaction time. Next, the valve situated between the particle feeder and the reactor tube is opened, and nitrogen from the feeder is mixed with the main gas. The SO_2 concentration is adjusted to the correct value and allowed to stabilise, before the addition of water (if it is used). When a stable SO_2 concentration is obtained, the injection of particles starts. The injected amount of particles depends on the amount of SO_2 absorbed by the particles, which should absorb enough SO_2 to minimise measurement uncertainties. However, the absorption must not be so high that the SO_2 concentration changes significantly. In practice, feed rates between 0.2 and 2.5 kg/hr are reasonable. When a stable SO_2 concentration has been obtained for 3-5 minutes, particle feeding is stopped and the SO_2 concentration is allowed to stabilise again. Finally, the particle container is emptied and the content is stored in a sealed container for later analysis. In the experiments, a SO_2 concentration of 1000 ppm was used if nothing else was stated. In general, atmospheric air was used as a balance gas due to practical causes. The use of atmospheric air as a balance gas meant that the reaction gas would contain small amounts of CO_2. However, no influence upon the results was observed when using atmospheric air as a balance gas.

During experiments the reactor pressure was kept at an atmospheric pressure of $\pm$20 mbar by the capsule fan, shown in Figure 8.1. From practical experience it turned out that a linear gas velocity in the isothermal part of the entrained flow reactor around 20 m/s was optimal. Assuming that all gases are ideal gases, the total gas flow can be calculated from equation 8.1.

$$\nu_{amb} = \frac{\pi D_{tube}^2 \upsilon_{gas}}{4} \frac{T_{amb}}{T_{reac}} \quad \frac{m^3}{s} \tag{8.1}$$

In equation 8.1: ν_{amb} is the gas flow at ambient temperature, D_{tube} is the diameter of the reactor tube, υ_{gas} is the linear velocity in the isothermal part of the reactor, T_{amb} and T_{reac} the ambient and the reactor temperatures, respectively.

8.3 Materials

Gases:

The purity of the concentrated gases (N_2, CO_2 and SO_2) was at least 99.2 %, and they were supplied from gas cylinders. Air was supplied through the pressurised air line in the experimental facility building, and it comprised dry atmospheric air. Pure steam was supplied by evaporating demineralised water.

Limestones, Quick Limes and Slaked Limes:
The quicklimes and slaked limes used for conducting the experiments were based on three naturally occurring limestones and produced in-house. One quicklime and one slaked lime were bought. Raw meals and hot meals[1] used for conducting the experiments were supplied by FLSmidth & CO A/S and originated from different cement production facilities around the world. Additives used were chemically pure substances. Table 8.1 and 8.2 show the chemical composition of the different materials on an oxide basis, along with the surface area, porosity and particle size distribution. In the following, the three limestones in Table 8.1 are named Faxe, Hole and Obajana, while the commercial CaO and $Ca(OH)_2$ are named commercial CaO and Commercial $Ca(OH)_2$, respectively.

[1] Hot meal is a calcined raw meal.

Material	Faxe Bryozo Limestone	Hole Limestone	Obajana Limestone	CaO	$Ca(OH)_2$
Composition [w/w%]				Commercial	Commercial
CaO	53.20	42.44	49.98	96.00	73.56
SiO_2	0.49	12.22	2.57	1.00	0.6
MgO	0.43	3.1	1.06	0.90	0.73
Al_2O_3	0.02	2.33	0.29	0.25	0.29
Fe_2O_3	0.03	1.2	0.14	0.25	0.11
K_2O	0.01	0.65	0.18	0.01	0.02
Na_2O	0.00	0.26	0.02	0.00	0
TiO_2	0.00	0.15	0.03	0.00	0.01
Mn_2O_3	0.01	0.03	0.00	0.01	0.01
P_2O_5	0.02	0.03	0.00	0.02	0.01
SrO	0.05	0.02	0.32	0.05	0.02
LOI	43.50	36.53	41.83	1.00	24.82
Total $CaCO_3$	97.16	76.58	92.56	/	/
Available CaO	/	/	/	/	67.12
Surface Area [m^2/g]	0.8	0.6	0.2	3.2	17.6
Porosity [%]	8.5	3.6	1.2	18	NaN
Particle distribution d(10%, 50%, 90%) [μm]	55, 145, 216	2.1, 12, 229.3	28, 115, 207	15, 108, 167	1.68, 6.98, 18.92

Table 8.1: *Composition of limestones and commercial CaO and $Ca(OH)_2$ used for the experiments.*

Material	Plant F	Plant H	Plant F	Plant H
Composition [w/w%]	Raw Meal	Raw Meal	Hot Meal	Hot Meal
CaO	42.48	/	61.94	/
SiO_2	13.91	/	20.21	/
MgO	1.82	/	2.52	/
Al_2O_3	3.58	/	4.99	/
Fe_2O_3	1.68	/	2.76	/
K_2O	0.87	/	1.42	/
Na_2O	0.23	/	0.33	/
TiO_2	0.20	/	0.27	/
Mn_2O_3	0.05	/	0.08	/
P_2O_5	0.16	/	0.22	/
SrO	0.06	/	0.09	/
LOI	34.87	/	3.19	/
Total $CaCO_3$	75.93	/	/	/
Available CaO	/	/	32.77	/
Surface Area [m^2/g]	5.5	8.0	4.1	7.8
Porosity [%]	13.5	/	34.7	37.1
Particle distribution d(10%, 50%, 90%) [μm]	1.16, 10.24, 97.67	/	0.61, 3.27, 75.85	/

Table 8.2: *Composition of raw meals and hot meals used for the experiments.*

8.4 Calcination of $CaCO_3$

Calcination of limestone is a delicate matter if sintering, and thereby loss of surface area, are to be avoided. From the literature it is known that larger surface areas result in higher reaction rates for the CaO/SO_2 reaction. Therefore, a method by which the calcination of limestone is possible with a minimum loss of surface area is desired. In this section the methods used will be outlined, while the results of the experiments will be discussed in Chapter 10. In order to avoid sintering when calcining limestone, both temperature and CO_2 concentration should be kept as low as possible. When dealing with CaO, and especially CaO with a large surface area, it is essential to minimise contact with atmospheric air as much as possible in order to avoid hydration and carbonisation. For this reason, calcined products are always stored in sealed containers or under controlled atmospheric conditions.

- **Fluid Bed Calcination**: Figure 8.2 shows a schematic drawing of the fluidised bed set-up used for calcination. Initially the set-up was heated to 850 °C (lower temperatures have turned out to be inefficient). The primary gas flow was 17.5 Nl/min of atmospheric air, while the secondary air flow was 10 Nl/min. When the temperature was stable, 400 g of limestone was added and allowed to calcine for 50 minutes. Subsequently, the calcined product was blown into the particle container. When calcining in the fluidised bed, Faxe limestone was used.

- **Vacuum Calcination**: Figure 8.2 shows the set-up used for vacuum calcination. The idea of using vacuum calcination was strongly inspired by the papers published by Beruto et al. and Ewing et al. [46, 155, 156] around 1980. The principle in vacuum calcination is that CO_2 concentration is very low, which is why the temperature can also be lowered. The experiments were carried out by placing a sample of $CaCO_3$ into an airtight container, which was subsequently connected to a vacuum pump and placed in a cold oven. The oven was heated to the temperature set point (650 or 750 °C), while a vacuum was created in the container. The sample was held at the temperature set point for up to 24 hours and was subsequently cooled to ambient temperature under vacuum conditions. When increasing the pressure again, it was done by N_2. The vacuum pump used maintained a vacuum of 30 ± 10 Pa in the airtight container, and the limestone used was Faxe.

- **Fixed Bed Calcination**: Figure 8.2 shows the fixed bed set-up. Here, the limestone was placed in one end of the ceramic tube outside the oven and positioned by the two porous plugs. Afterwards, the ceramic tube was placed into the oven and the gas flow switched. The calcination process took place for up to two hours and 15 minutes, after which the ceramic tube was removed from the oven and allowed to cool down with the gas flow switched. The temperature interval used was 700-800 °C, while the gas flow was set at 10 to 15 Nl/min (either nitrogen or pressurised air). The mass loading ranged from 2 to 5 g.

In some experiments a pump was connected to the gas outlet in order to see whether it was possible to obtain a faster removal of CO_2 from the $CaCO_3$ bed. The limestone source was Faxe.

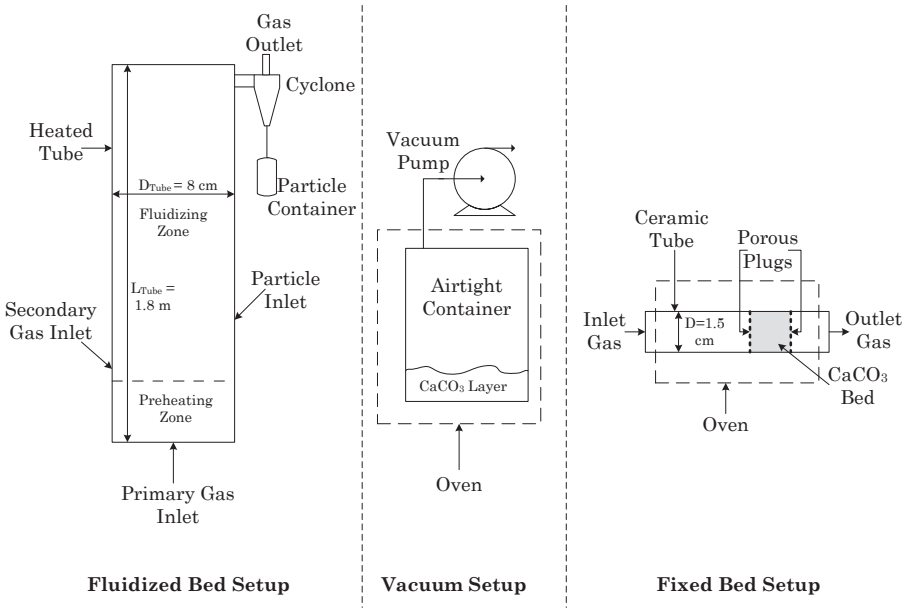

Figure 8.2: *Schematic drawing of three of the four reactors used for calcinating limestone containing materials.*

- **Flash Calcination**: When conducting flash calcination the entrained flow reactor shown in Figure 8.1 was used, with a temperature set point for the reactor between 750 and 850 °C. The linear velocity in the isothermal part was 20 m/s, while the limestone feed rate was 200 or 500 g/hr. The calcined product was collected in the particle container, which was frequently emptied. When carrying out calcination in the entrained flow reactor, the gas flow was comprised by pressurised air, which enters exclusively through the preheater. For the flash calcination experiments all three limestones described in section 8.3 were used.

Chapter 9

Data Treatment and Definition of Calculated Parameters

This chapter defines the conversion with respect to SO_2, the calcium species fraction and the mass fraction. It is also outlined how these important dimensionless numbers are calculated from experimental data obtained in the entrained flow reactor and TGA measurements.

9.1 Conversion With Respect to SO_2

Figure 9.1 shows a typical SO_2 measurement, with the horizontal lines indicating the steady-state levels used for calculations. The difference in SO_2 concentration with and without particle injection is due to SO_2 absorption by the injected material. The steady-state levels are used for calculating an average SO_2 concentration before, during and after particle injection. The calculations are made by a Matlab program specially designed for the purpose (Appendix G outlines the program algorithm). Besides calculating SO_2, steady-state values for all other logged parameters are also calculated, taking into account any time delay between the parameter and SO_2 concentration. The standard deviations for the steady-state values are calculated simultaneously by the Matlab program.
Equation 9.1 defines the conversion with respect to SO_2 as the moles of SO_2 absorbed per moles of base compound. The use of different bases is convenient when dealing with different materials and partly calcined particles.

$$X_{SO_2/basis} = \frac{n_{SO_2}}{n_{basis}}, \qquad n_{basis} = n_{Ca},\, n_{CaO},\, n_{Ca(OH)_2},\, n_{CaCO_3} \tag{9.1}$$

The definition stated in equation 9.1 is rewritten to equation 9.2, which can be used to calculate the conversion from the steady-state values obtained in the entrained flow reactor experiments.

$$X_{SO_2/basis} = \frac{-\Delta x_{SO_2} \cdot P \cdot \nu_{amb}}{R_{gas} \cdot T_{amb}} \frac{M_i}{W_p \cdot Q_{i/m_{tot}}} \tag{9.2}$$

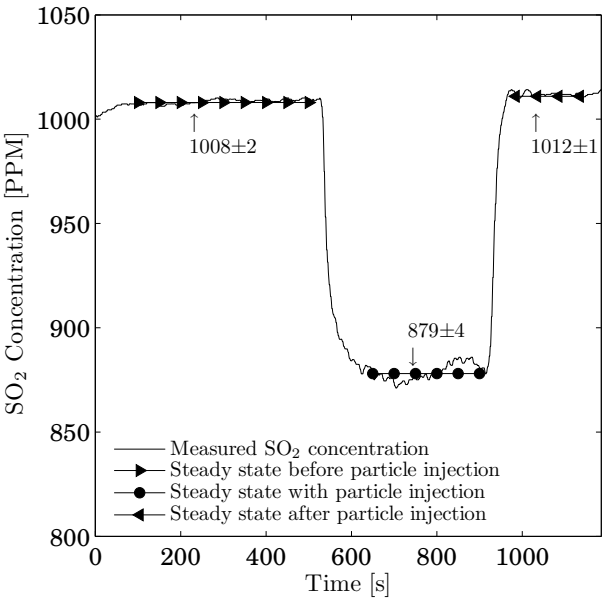

Figure 9.1: *Example of a steady-state interval for a SO_2 measurement obtained in the entrained flow reactor.*

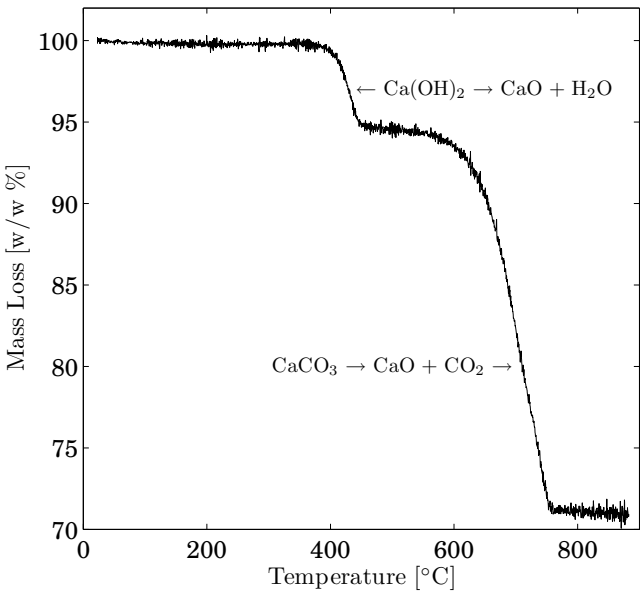

Figure 9.2: *TGA plot of a sample that contains $Ca(OH)_2$, $CaCO_3$ and CaO.*

In equation 9.2, Δx_{SO_2} is the steady-state mole fraction with particle feeding minus the average SO_2 mole fraction, before and after particle feeding. M_i is the molar mass of the compound on which the mass fraction ($Q_{i/m_{tot}}$) is based.

9.2 Mole and Mass Fraction of Calcium Species

Figure 9.2 shows a TGA measurement with the two drops in mass caused by the decomposition of $Ca(OH)_2$ and $CaCO_3$. At temperatures above 800 °C no mass loss is observed, because all the $Ca(OH)_2$ and $CaCO_3$ has decomposed to CaO, which is why the sample is constituted exclusively by CaO plus impurities such as SiO_2. The mass fraction of CaO at this temperature is easily determined from the tables in section 8.3. The mass of $CaCO_3$ and $Ca(OH)_2$ in the sample is determined from the mass losses due to CO_2 and H_2O, respectively.
Equation 9.3 shows the definition of the mole fraction for component i. The mole fraction is calculated from the TGA data by calculating the moles of $Ca(OH)_2$ and $CaCO_3$ equal to the loss in moles of H_2O and CO_2, respectively. The moles of Ca are equal to the moles of CaO found at 800 °C. In case i is CaO, the moles of CaO should be calculated by subtracting the moles of $Ca(OH)_2$ and $CaCO_3$ from the moles of Ca calculated at 800 °C.

$$x_{i/Ca} = \frac{n_i}{n_{Ca}}, \qquad i = CaO,\, Ca(OH)_2,\, CaCO_3 \tag{9.3}$$

The mass fraction of component i is defined in equation 9.4. The moles of CaO, $CaCO_3$ or $Ca(OH)_2$ are calculated as above and multiplied by the molar mass of component i, and then

divided by the total sample mass used in the TGA experiment.

$$Q_{i/m_{tot}} = \frac{m_i}{m_{tot}} = \frac{n_i \cdot M_i}{m_{tot}} \qquad i = CaO,\, Ca(OH)_2,\, CaCO_3 \tag{9.4}$$

Chapter 10

Calcination Results

This chapter presents the results of the four calcination methods (fluid bed, vacuum, flash and fixed bed). The discussion is based on mercury porosimetry measurements, which is why it should be noted that surface area is proportional to the reciprocal of pore size, meaning that smaller pores results in a larger surface area. Figure ordinate axes in this chapter are "Log differential intrusion", which is a measure for the amount of pores at a given pore diameter.

10.1 Vacuum Calcination

Figure 10.1 shows pore size distribution for Faxe limestone calcined under vacuum at 680 °C for different periods. The figure shows that the pore-system becomes bipartite with an enlargement of the primary pore-system, which also exists in the parent limestone. The secondary pore-system evolves around 0.08 μm independent of the calcination time. It is clear that the number of pores, in the secondary pore-system, increase with calcination time and thereby also calcination degree, while the pore enlargement of the primary pore-system is similar in all three cases. This shows that the enlargement of the primary pore-system is faster than the formation of the secondary pore-system. Vacuum calcination at lower temperatures (580-630 °C) was also tried, but a secondary pore-system was not observed, since the temperature was too low for the initiation of the calcination process. If the secondary pore-system pore size is compared to the results by Beruto et al. and Ewing et al. [46, 155, 156] it is seen that they obtain a pore diameter about 10 times smaller. This difference is most likely caused by the $CaCO_3$ source. In the literature [46, 155, 156], were experiments conducted using a pure $CaCO_3$ source, while a natural Faxe limestone (containing significantly more impurities) was used here. The difference in vacuum conditions are not the reason, since Ewing et al. [156] conducted experiments with a CO_2 partial pressure up to 1200 Pa, at temperatures similar to ours, obtaining a secondary pore diameter whcih was about 10 times smaller.

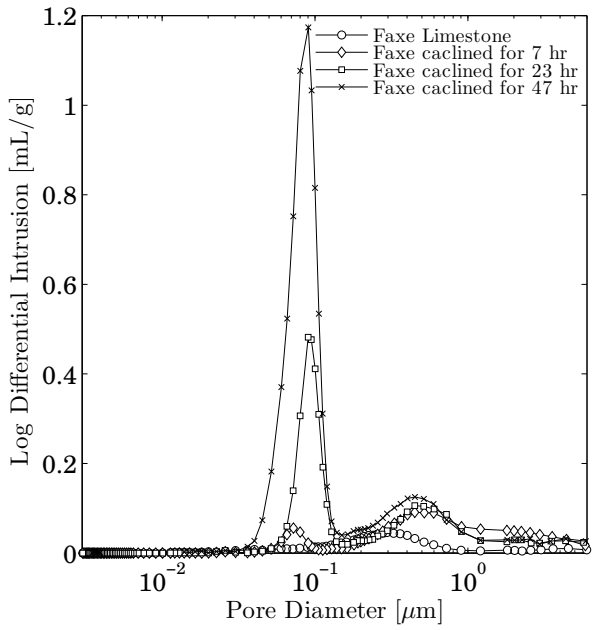

Figure 10.1: *Pore size distribution for Faxe limestone calcined under vacuum at 680 °C.*

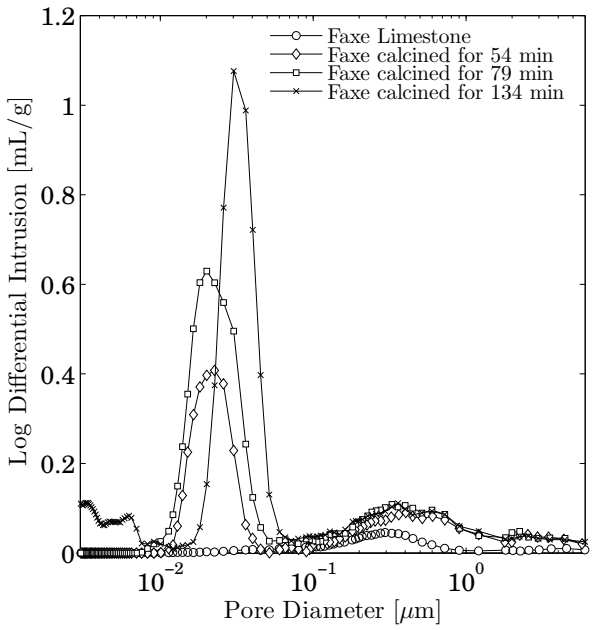

Figure 10.2: *Pore size distribution for Faxe limestone calcined in a fixed bed at 800 °C.*

10.2 Fixed Bed Calcination

Figure 10.2 shows pore size distribution for Faxe limestone calcined in the fixed bed set-up at 800 °C. The same behavior as in the vacuum calcination is observed here, with an enlargement of the primary pore-system independent of calcination time and a secondary pore-system which increase with calcination time and calcination degree. In this case, the secondary pore-system evolves around a pore diameter of 25 nm, with a tendency to larger pores when the calcination time increase. The increase observed below 10 nm for Faxe calcined in 134 min is most likely, judged from the shape of the curve, due to a measuring error. Variation of calcination conditions, within the earlier stated intervals, has not shown any effect on the development of the secondary pore-system.

10.3 Flash Calcination

Figure 10.3 shows pore size distribution for Faxe limestone flash calcined in less than one second at different temperatures. It is clear that the primary pore-system enlargement is faster than development of the secondary pore-system. This is seen from that the primary pore-system is at 800 and 850 °C and the secondary pore-system develope around a diameter of 8 nm. At 750 °C, the enlargement of the primary pore-system is smaller than in the two other cases and the formation of a secondary pore-system incipient at about 8 nm.

Figure 10.4 shows pore size distribution for Hole, Faxe and Obajana limestone, flash calcined at

850 °C. It is clear that the secondary pore-system in all cases evolves around 8-10 nm, while the primary pore-system evolves in different manners, with almost no primary pore-system in calcined Obajana limestone compared to Hole and Faxe, with the calcined Faxe limestone showing the smallest pores in the primary pore-system. If the number of pores in the secondary pore-system for Obajana are compared to the results for Hole and Faxe it is noteable that Obajana shows a less developed secondary pore-system, which is also reflected in the mole fraction of CaO in the calcined product, which is 26.6 % compared to 51.7 and 45.7 % for Hole and Faxe, respectively. What cause a lower content of CaO is uncertain since no apparent difference can be observed between the parent limestones in table 8.1, but the difference shows that the calcination kinetics of limestones strongly depends on the starting material.

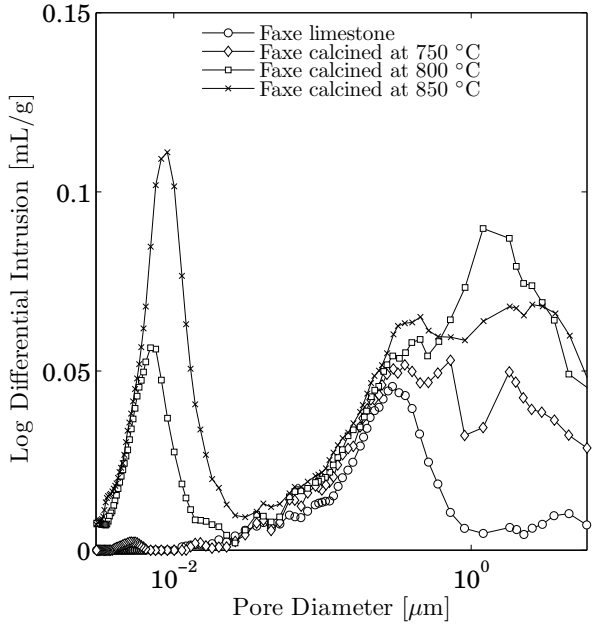

Figure 10.3: *Pore size distribution for Faxe limestone flash calcined in less than one second.*

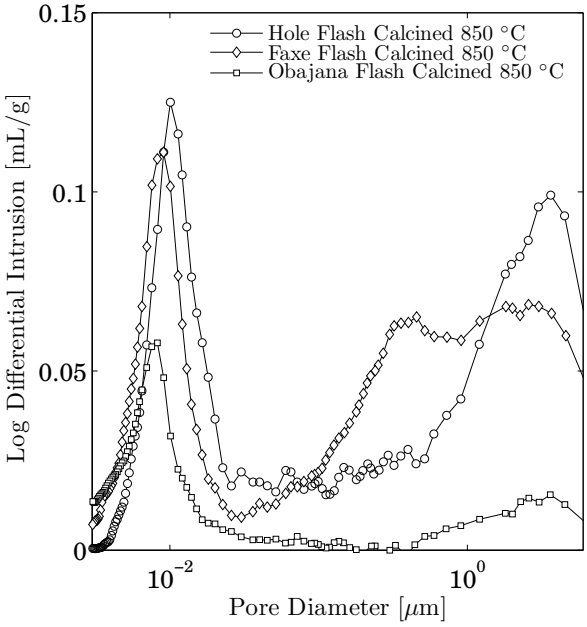

Figure 10.4: *Pore size distribution for Hole, Faxe and Objana limestone, flash calcined at 850 °C.*

10.4 Comparison of Calcination Methods

Figure 10.5 shows pore size distribution for all 4 methods tried. Here, it is observed that the product which originating from fluid bed calcination has a very broad distribution compared to the other methods. The primary system is more pronounced for the fluid bed calcination which is probably due to a higher degree of sintering. Furthermore, it is seen that flash calcination results in the secondary pore-system with the smallest pore diameter, while the vacuum calcination results in the largest. Fabrication of CaO for experiments with SO_2 was carried out by flash calcination and calcination in the fluid bed.

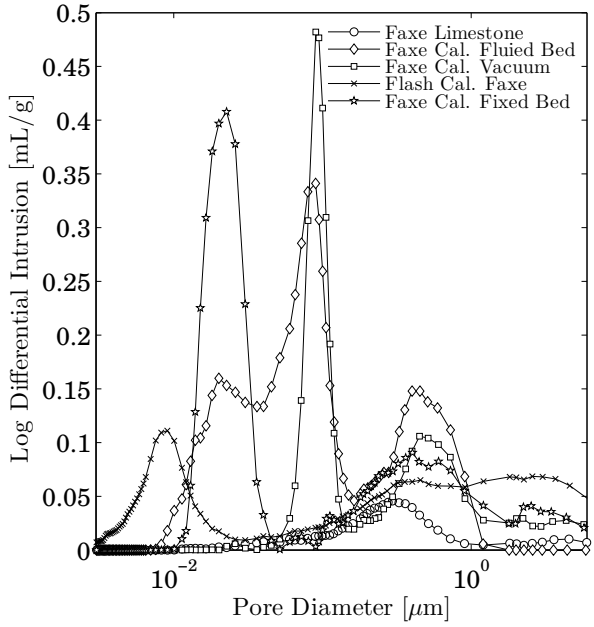

Figure 10.5: *Comparison of pore size distribution obtained from different methods of calcining.*

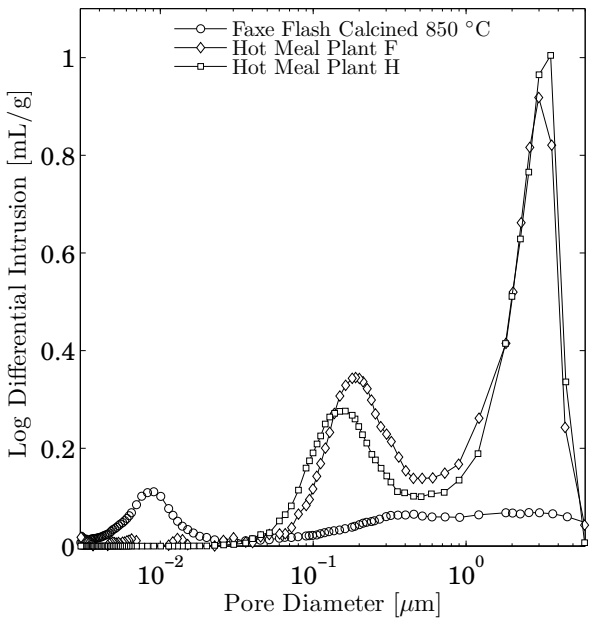

Figure 10.6: *Pore size distribution for the hot meals obtained from plant F and H. The pore size distribution for the flash calcined Faxe limestone is shown for comparison.*

Table 10.1 summarises the properties of those calcines that have been used for experiments with SO_2 absorbtion. As seen from the table, is it only bought material which is fully calcined. The surface area of the calcined materials are significantly larger than surface area observed in the parent limestones (see table 8.1). Therefore, it is reasonable to assume that the increase in surface areas are due to the calcination process and it can be assumed that only CaO is found at the surface.

The Materials, 5xFaxe 850, 2xFaxe 850, 2xFaxe$_{Na_2CO_3}$ 850 and 2xFaxe$_{CaCl_2}$ 850, is Faxe limestone where flash calcination has been repeated. The repeated flash calcination is also seen from the larger mole fraction of CaO in thier calcines. The subscripts Na_2CO_3 and $CaCl_2$ denotes that 2 w/w % of these species were added to the limestone. They were added as a water solution and excess water was evaporated before calcination. It is noteworthy that both species apparently promotes the calcination process, seen by a higher content of CaO in the doped calcines compared to the non-doped calcines.

Material	Cal. Method	$x_{CaO/Ca}$	$Q_{m_{CaO}/m_{tot}}$	A_{BET}	A_{BET}	Porosity
		mol/mol	kg/kg	m^2/g solid	m^2/g CaO	%
Faxe 750	F.C.	12.1%	6.9%	9.9	143.8	14
Faxe 800	F.C.	25.8%	15.4%	15.7	102.0	21
Faxe 850	F.C.	45.7%	30.2%	27.1	89.8	31
Obajana 850	F.C.	26.6%	15.1%	16.8	111.4	-
Hole 850	F.C.	51.7%	28.8%	14.2	49.3	-
2xFaxe 850	F.C. twice	60.2%	42.2%	36.2	85.8	-
2xFaxe$_{CaCl_2}$ 850	F.C. twice	74.0%	51.3%	-	-	-
2xFaxe$_{Na_2CO_3}$ 850	F.C. twice	81.8%	66.4%	-	-	-
5xFaxe	F.C. five times	81.8%	68.9%	-	-	-
Faxe 900	F.C.	20.1%	12.3%	-	-	-
Faxe commercial	Bought	100%	96%	3.2	3.2	18
Faxe FB	Fluid Bed	87.5%	76.3%	20.1	26.3	52

Table 10.1: *Characterization of partly calcined limestones used for studying the reaction between CaO and SO_2. F.C. denotes that the material has been flash calcined.*

10.5 Hot Meals

Figure 10.6 shows pore size distribution in hot meals from plant F and H along with the distribution for Faxe limestone flash calcined at 850 °C. The large amount of pores observed in the primary pore-system are to some extend caused by void between the fine particles that comprises the hot meals. The secondary pore-system for both hot meals seems to evolve between 100 and 200 nm, which is a considerably larger pore diameter than observed for the flash calcined limestone. It was expected that hot meals were comparable to the flash calcined limestone, since the calciner unit in a cement plant works as a flash calciner with a residence time of a few seconds. However, the secondary pore-systems evolves differently, with pronounced sintering of the hot meal CaO and only little or no sintering of the CaO obtained from flash calcination. The pronounced sintering of the hot meals is caused by the combustion of fuels, which leads to zones with a temperature considerably higher than the approximately 850 °C observed in the outlet of the calciner unit. Sintering is further accelerated by CO_2 and water in the calciner, both known to promote sintering. The pronounced sintering is also seen from the surface areas (see table 8.2), which in the case of plant F hot meal only is 15 % of the surface area found in the flash calcined Faxe limestone. The corresponding value for plant C hot meal is 29 %. When comparing raw meal and hot meal surface areas (see table 8.2), is it remarkable that raw meal surface areas are larger than hot meal surface areas. This is the opposite of the result from the calcination experiments, where a large increase in surface area was observed for calcines.

Chapter 11

Mass and Temperature Gradients

When evaluating experimental data it is of great importance to know whether the observed results are influenced by mass and/or temperature gradients. Here, both phenomena will be evaluated. The equations and constants used can be found in Appendix B

11.1 Mass Diffusion Limitations

The Weisz-Prater modulus (see Appendix B) compares the observed rate of reaction to the rate at which diffusion in a porous material takes place. According to Levenspiel [133], a Weisz-Prater modulus smaller than 0.15 indicates that the results are not influenced by internal diffusion limitations. Similar to the Weisz-Prater modulus for evaluating internal diffusion limitations, external diffusion limitation can be evaluated by Mears criterion. According to Scott Fogler [157], external diffusion can be neglected if Mears criterion is smaller than 0.15.
Figure 11.1 shows the particle diameter at which the Weisz-Prater modulus is equal to 0.15 as a function of the measured CaO conversion for three different CaO materials, while Figure 11.2 shows a similar plot for Mears criterion. Thus, the particle diameters shown in Figure 11.1 and 11.2 are the largest diameter in each experiment where diffusion limitations can be ruled out.

From Figure 11.1 it is evident that the particle diameter at which internal diffusion limitations are negligible is smaller than 25 μm. In the case of external diffusion, Figure 11.2 shows that it will begin to influence the results at particle diameters between 10 and 70 μm. Comparing these critical diameters to the particle distributions, for the three different CaO materials, in Figure 11.3, it is evident that internal diffusion will influence the results for at least 85 w/w % of the particles, while the corresponding number for external diffusion is 80 w/w %.

In order to verify the calculated results, the reaction product from an experiment with Faxe 850 was fractionated and the sulphur content subsequently determined. Table 11.1 summarises the results. The actual concentration gradients were studied by slicing a sample of Faxe 750 particles

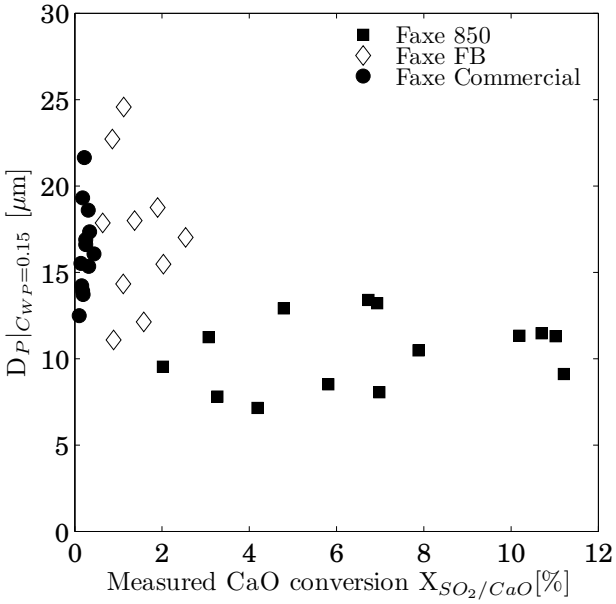

Figure 11.1: *Particle diameters at which the Weisz-Prater modulus (C_{WP}) is equal to 0.15 as a function of the measured CaO conversion for three different CaO materials.*

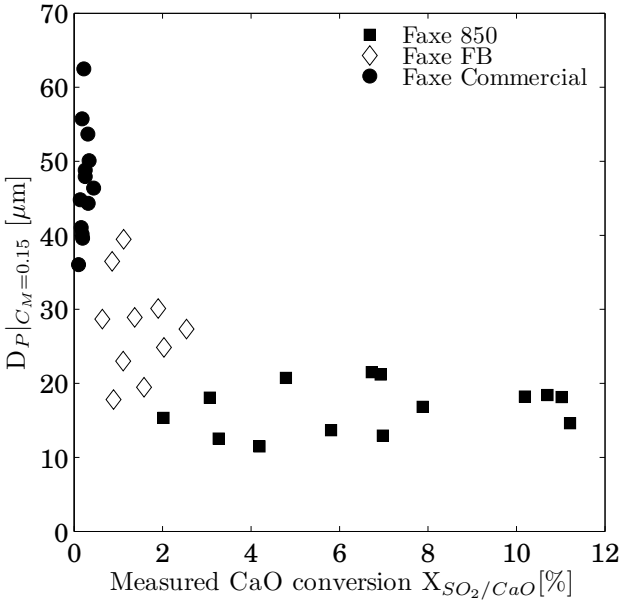

Figure 11.2: *Particle diameters at which Mears criterion (C_M) is equal to 0.15 as a function of the measured CaO conversion for three different CaO materials.*

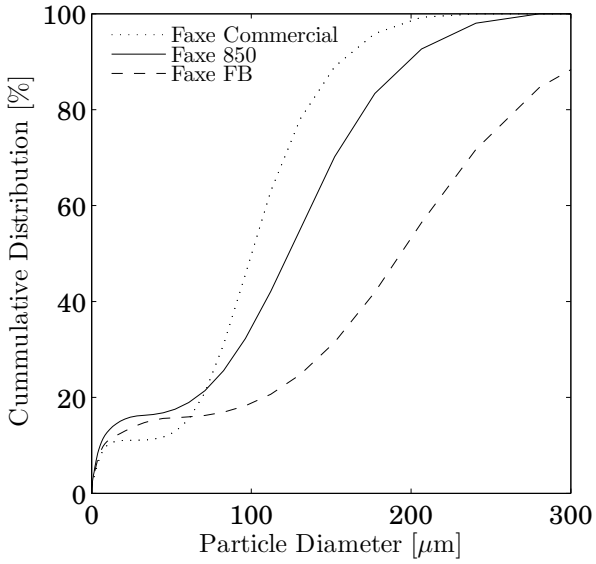

Figure 11.3: *Particle size distribution for the three CaO materials used for evaluating diffusion limitations.*

and subsequently mapping the cross-sectional sulphur content by EDX. Figure 11.4 shows the results for three different particles, all of which had a diameter around 80 μm.

The results in Table 11.1 and Figure 11.4 confirm the Weisz-Prater modulus and Mears criterion calculations, showing that diffusion limitations can not be ruled out when interpreting experimental results.

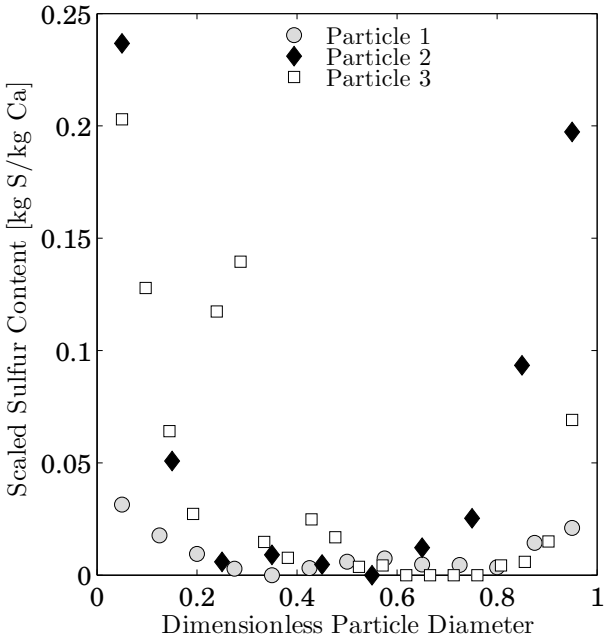

Figure 11.4: *Scaled sulphur content as a function of the dimensionless particle diameter.*

Particle size	sulphur content
μm	w/w %
0-32	4.35
32-90	1.05
90-150	0.33
150-∞	0.25

Table 11.1: *Measured sulphur content in Faxe 850 reacted with SO_2 at 517 °C for 0.08 s in atmospheric air.*

11.2 Temperature Gradients

The high conversions observed here, within an extraordinarily short time, can result in a particle temperature considerably higher than the bulk gas temperature due to the exothermic reactions taking place. In order to clarify this question, an energy balance for a spherical particle was established, as outlined in Appendix B.

Figure 11.5 and 11.6 show the deviation between bulk gas temperature and the particle temperature as a function of the observed reaction rate for SO_2 and CO_2. The particle temperature is here evaluated in the core, where the temperature is highest. When calculating Figure 11.5 and 11.6, it is assumed that the reactions take place in an outer shell, which is 20 % of the particle radius.

The highest observed reaction rate for the SO_2/CaO reaction is 5500 mol/m^3/s, whereas for the carbonisation reaction it is $2{\cdot}10^4$ mol/m^3/s. Comparing these numbers to Figure 11.5 and 11.6 it is evident that the deviation between bulk gas temperature and particle temperature will be up to 0.6 %. A temperature difference of this size is negligible, which is why the assumption of an isothermal reaction is valid.

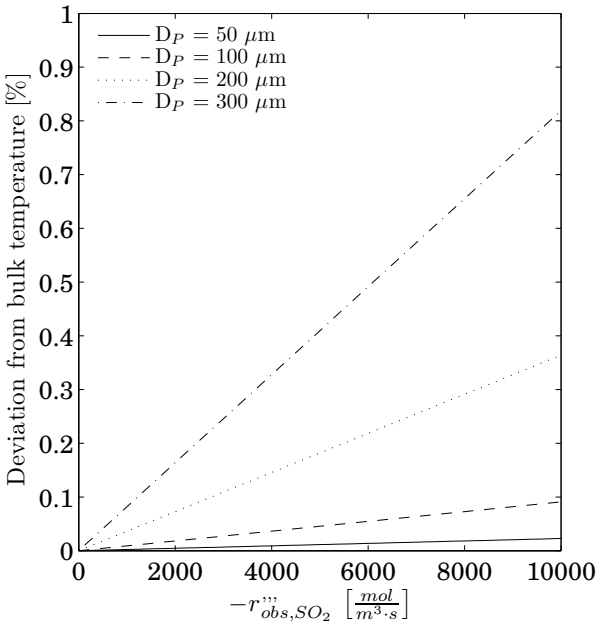

Figure 11.5: *Deviation between core temperature and bulk gas temperature as a function of the observed reaction rate for the CaO/SO_2 reaction.*

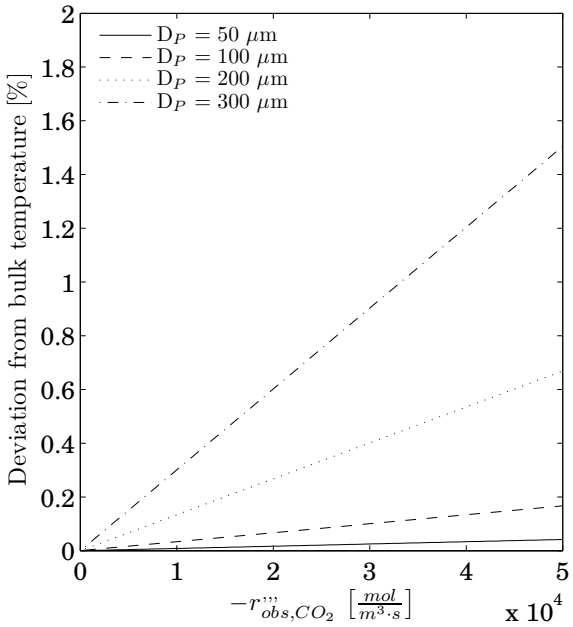

Figure 11.6: *Deviation between core temperature and bulk gas temperature as a function of the observed reaction rate for the CaO/CO_2 reaction.*

Chapter 12

SO_2 Absorption on CaO

Here, the experimental results for SO_2 absorption on the calcines discussed are presented. This chapter will outline the experimental results obtained when investigating SO_2 absorption on the calcines, described earlier in Chapter 10. In the interpretation of the results, it should be kept in mind that both external and internal mass transfer have been shown to influence the observed results. If nothing else is stated, the SO_2 concentration was 1000 ppm in the experiments.

12.1 The Influence of Surface Area

Figure 12.1 shows the CaO conversion as a function of the surface area for different calcines of Faxe limestone when reacted with SO_2. It is evident that the CaO conversion increases with surface area, while a positive effect of temperature is in general also observed. It is also seen that an increase in surface area can compensate for a lower reaction temperature. The positive effect of increasing surface area was also reported in the literature [105,109,111].
In Chapter 11 it was shown that the observed results are heavily influenced by diffusion limitations. The positive effect of surface area upon CaO conversion shows that external diffusion does not exclusively limit the reaction rate, since CaO conversion would then depend purely on the external surface area, which is similar in all experiments with Faxe 750, 800 and 850. From Figure 12.1 it is evident that for experiments at 441 °C and 517 °C the positive effect of surface area seems to level off. That the CaO conversion levels off for very large surface areas is a consequence of external diffusion resistance limiting the transfer of SO_2. However, when the data points obtained between 573 and 590 °C are considered together (the small variations in temperature are considered negligible), the CaO conversion appears to increase at least linearly with surface area. Contrary to the results at lower temperatures, the observed conversion at 590 °C does not seem to level off. Considering the gas phase diffusion coefficient for SO_2, it only increases with a factor of about 1.5 from 441 to 590 °C. This increase is less than the increase observed in conversion, which is why an increase in SO_2 diffusivity can not explain the observed behaviour alone.

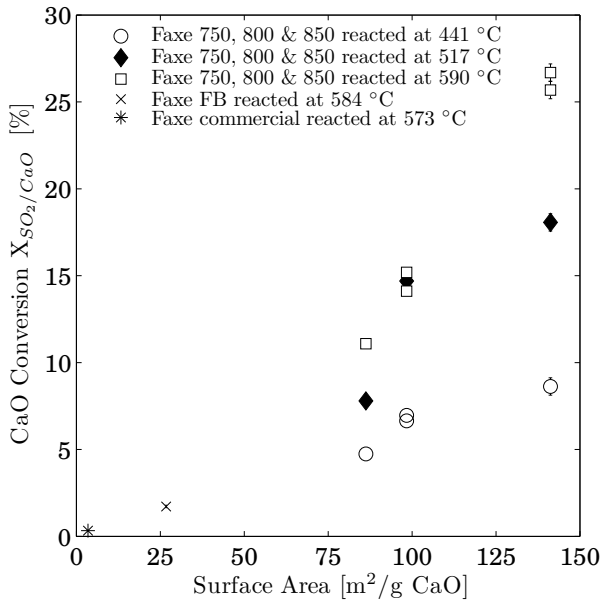

Figure 12.1: *CaO conversion as a function of surface area. For partly calcined Faxe limestones reacted for 0.36 s in atmospheric air.*

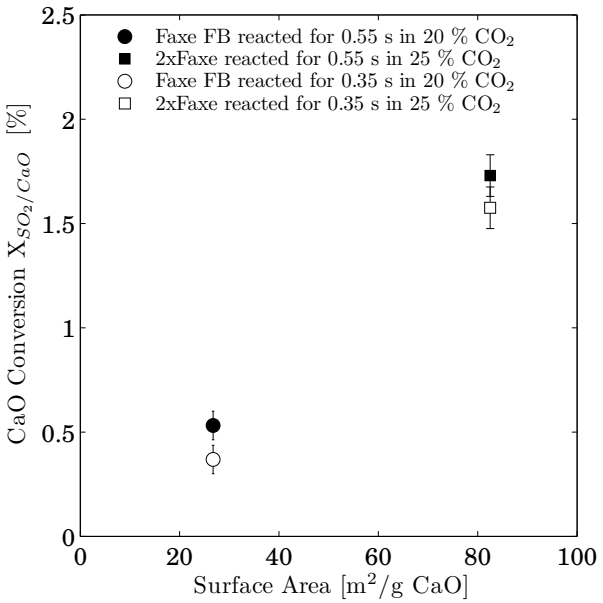

Figure 12.2: *CaO conversion as a function of surface area. For partly calcined Faxe limestones reacted in a CO_2 atmosphere containing 20 to 25 % CO_2 at 535 °C.*

Figure 12.2 shows the CaO conversion as a function of surface area for two differently calcined Faxe limestones. The calcines were reacted with SO_2 for 0.35 s or 0.55 s in a gas containing either 20 or 25 % of CO_2. If these CaO conversions are compared to those obtained in Figure 12.1, it is noteworthy that considerably lower CaO conversion results when CO_2 is present in the reaction gas. From the figure, it is seen that a higher surface area leads to higher CaO conversion, even though the sulphation is suppressed by CO_2. Furthermore, it is noticeable that an increase in reaction time from 0.35 s to 0.55 s only has a very small effect on CaO conversion, indicating that most of the reaction takes place within less than 0.35 s.

12.2 The Influence of Mass Fraction of CaO in Material

Figure 12.3 shows the CaO conversion as a function of the CaO mass fraction in the calcined material. The CaO conversion decreases as the mass fraction of CaO in the material increases, while the decrease in CaO conversion is caused by a smaller surface area of CaO per mass of CaO, as seen from the secondary axis, which indicates that a smaller fraction of the CaO molecules will be found as surface molecules, whereby less CaO will be available for reaction with SO_2.

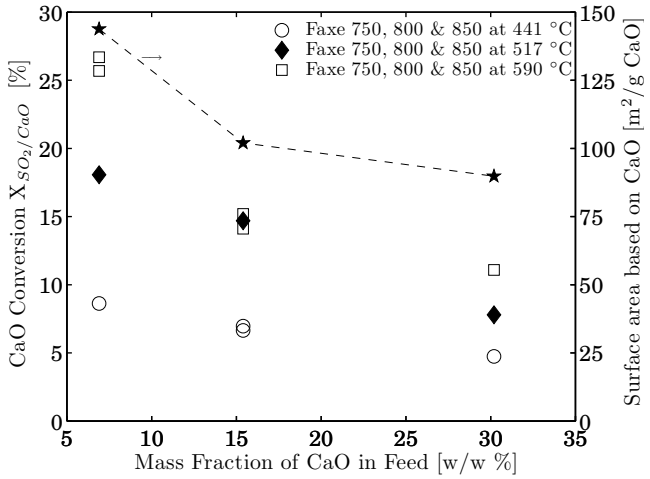

Figure 12.3: *CaO conversion as a function of the mass fraction of CaO in the used particles. Reaction time 0.36 s in atmospheric air.*

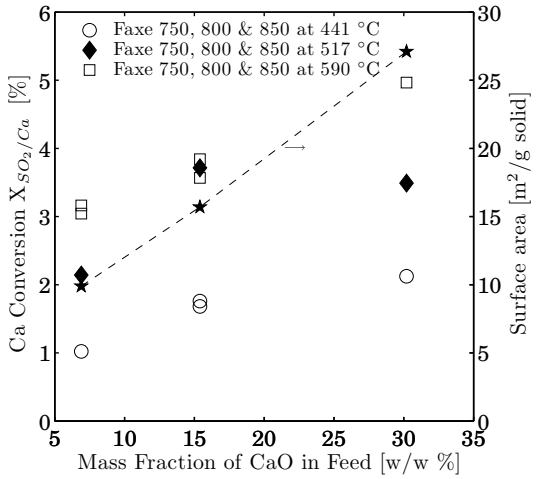

Figure 12.4: *Ca conversion as a function of the mass fraction of CaO in the used particles. Reaction time 0.36 s in atmospheric air.*

Figure 12.4 shows the conversion calculated as the moles of SO_2 absorbed per mole of Ca. At 590 °C and 441 °C a continuous increase in Ca conversion is observed, which is in accordance with the behaviour observed for the surface area of the particles, which also increase with increasing mass fraction of CaO. At 517 °C the Ca conversion has a maximum at a mass fraction of 15 w/w %. What causes this maximum is uncertain, yet if the point is omitted it is evident that the trend is the same as observed at 441 and 590 °C.

In experiments with uncalcined Faxe limestone at 600 °C and a reaction time of 0.35 s, Hu et al. [68] found a Ca conversion of 0.08%, which is 63 times smaller than observed here, with a CaO mass fraction of 30.2 %.

The higher reactivity observed is caused either because more CaO is available at the gas/solid interface and/or the CaO/SO_2 reaction is faster than the $CaCO_3/SO_2$ reaction. Since the surface area in our experiments is about 34 times greater, at least part of the increased conversion must be due to a higher reactivity of CaO compared to $CaCO_3$. Our results are shown to be limited by diffusion, giving a lower rate than what is actually possible. It is therefore expected that the true kinetic rate of the CaO/SO_2 reaction is more than a factor of 1.8 faster than the $CaCO_3/SO_2$ reaction rate. Nonetheless, it can be concluded from the results that the CaO/SO_2 is faster than the $CaCO_3$ reaction.

12.3 The Influence of Reaction Time

Figure 12.5 shows that the CaO conversion increases with reaction time. The difference in CaO conversion among the three calcines is due to the difference in surface area in the starting material (see Table 10.1). The slope of the lines interconnecting the measurement points can be

interpreted as an apparent reaction rate. When doing so it is noticed that, in all cases, the reaction rate is fastest within the first 0.08 s. Hereafter, the rate levels off and the increase in conversion becomes linear from 0.18 s and forward. That the initial reaction of the SO_2/CaO reaction is fast is further illustrated in that more than 50 % of the observed CaO conversion, in all cases, takes place within the first 0.18 s, which comprises less than one-third of the total reaction time. From the data in Figure 12.5 it can be calculated that the apparent rate, calculated as a CaO conversion per second, within the first 0.08 s ranges from 1.07 s^{-1} for Faxe 750 to 0.4 s^{-1} for Faxe 850. Thus, all CaO would be converted in less than a second for Faxe 750, if the initial reaction rate controlled the entire CaO conversion.

Borgwardt and Bruce [105] conducted experiments at 800 °C using CaO particles with a surface area of 63 m^3/g. They performed their first measurement after 3 seconds of reaction. From their data an apparent initial reaction rate of $6.2{\cdot}10^{-2}$ s^{-1} was calculated. The initial reaction rate observed in our experiments is 6.5-17 times larger than what Borgwardt and Bruce [105] observed at a reaction temperature about 300 °C higher. Initial reaction rates so much higher than what has been observed at a significantly higher temperature indicate that the initial rate can be significantly underestimated if determined from experimental data obtained after more than 1 second. In fact our data makes it reasonable to assume that diffusion limitations will be present in the initial phase of any SO_2/CaO experiment, unless using extreme conditions such as very low temperatures and extremely small particles.

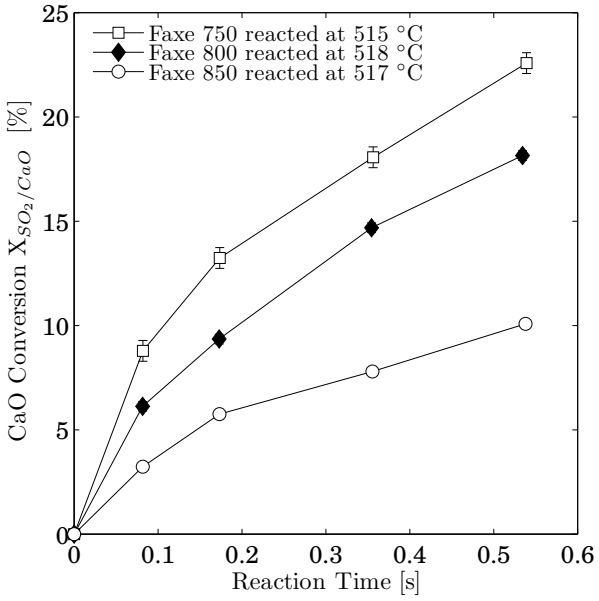

Figure 12.5: *CaO conversion as a function of the reaction time for partly calcined Faxe limestone with different amounts of CaO. The experiments were conducted in atmospheric air.*

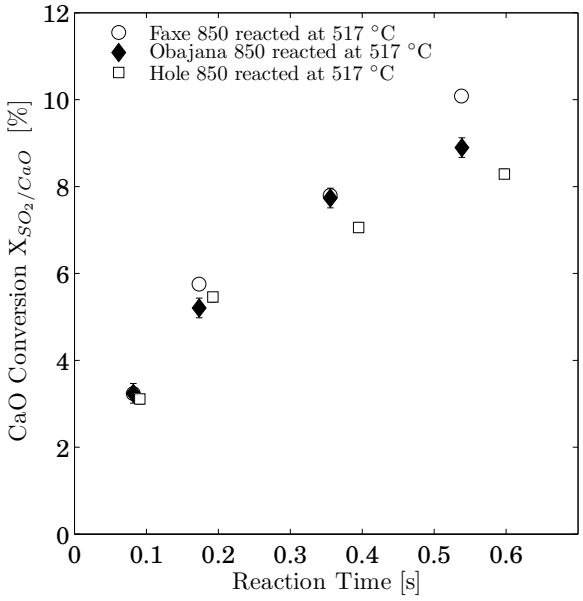

Figure 12.6: *CaO conversion as a function of the reaction time for three different partly calcined limestones containing different amounts of CaO. The experiments were conducted in atmospheric air.*

Figure 12.6 shows the CaO conversion as a function of the reaction time for calcines of Hole, Faxe and Obajana limestones. The parent limestone was in all cases flash calcined under the same conditions, but the calcination resulted in different CaO contents and surface areas, as seen from Table 10.1. From Figure 12.6 it is evident that the CaO conversions for calcines prepared at the same conditions are similar, even though the CaO content and surface areas are different.
The similar conversions observed here may be caused by natural impurities found in the parent stones, influencing the initial reaction kinetics in different manners. Consequently, species promoting sintering and thereby a decrease in surface area promote the CaO/SO_2 reaction, whereby they counteract the decrease in surface area. On the other hand, species which enhance the calcination process and thereby the formation of surface area inhibit the CaO/SO_2 reaction. That calcines of different limestones appear to behave identically is contrary to the literature [112], where the reactivity of different calcines was different.
The full line graphs in Figure 12.7 show the conversion of CaO into sulphur species (left axis), while the dotted graph shows the unconverted fraction of the initial CaO (right axis), both plotted as a function of reaction time. The CaO conversion is considerably smaller than in atmospheric air. Furthermore, a negative effect of temperature is observed in Figure 12.7. From the experiments in atmospheric air, a linear increase in CaO conversion is observed after 0.18 s. Here, the reaction rate decreases continuously when increasing the reaction time. In fact, the reaction is almost completed after 0.35 s at 534 °C . The fraction of unconverted CaO in the partly calcined limestone decreases remarkably fast, reaching a constant level of about 55 % after 0.35 s. TGA measurements show that the decrease is due to an uptake of CO_2 about 25 times larger than the SO_2 uptake. Furthermore, BET measurements show that after 0.35 s only 10 % of the internal surface area found in the starting material is left. From these results it is obvious that free CaO will react extremely fast with CO_2, if exposed to a CO_2 concentration higher than the equilibrium concentration. The negative effect of higher temperatures is a consequence of the fast uptake of CO_2, while the partly calcined limestone used has a bipartite pore-system with a main pore diameter of about 500 nm and a secondary pore diameter about 10-20 nm. In such a bipartite pore-system, the majority of the surface area is situated in the secondary pore-system. Furthermore ,both the CaO/CO_2 and the CaO/SO_2 reaction rates will increase with temperature, but since the molar volume of $CaCO_3$ is about 2.5 times that of CaO, the secondary pore-system blocks up faster at higher temperature levels, so the surface area available for reaction with SO_2 will decrease even faster. The reduction in surface area with a decreasing fraction of unconverted CaO is supported by the BET measurements.

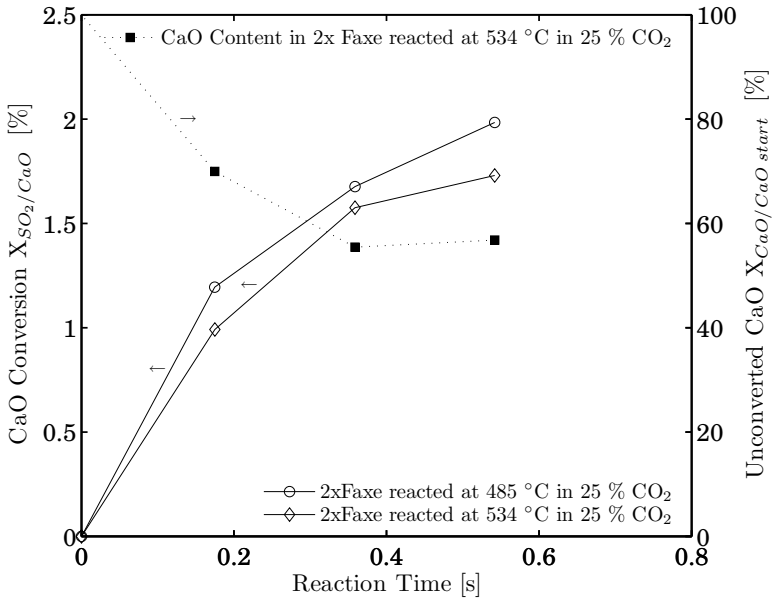

Figure 12.7: *CaO conversion as a function of the reaction time for partly calcined Faxe limestone, when the reaction gas contains 25 % CO_2.*

The large uptake of CO_2 begs the question as to whether SO_2 reacts with CaO or $CaCO_3$. This is important, since the initial rate of the SO_2-$CaCO_3$ is slower than the initial kinetic of the SO_2/CaO reaction, as concluded earlier. The experimental results show that the CaO/SO_2 reaction only contributes to the observed CaO conversion to sulphur species until the particles are saturated with CO_2. At a temperature of 534 °C , the CaO/SO_2 reaction only takes place within the first 0.35 s. At longer reaction times, the dominating mechanism for SO_2 absorption is the SO_2/$CaCO_3$ reaction, which is also reflected in the levelling off of the reaction rate after 0.35 s at 534 °C .

12.4 The Influence of CO_2 on the CaO/SO_2 Reaction

Figure 12.8 shows the CaO conversion as a function of CO_2 concentration in the reaction gas. It should be noted that these experiments were conducted with Faxe limestone calcined in a fluid, meaning that the CaO content is considerably larger than in the flash calcined limestones, while the surface area is smaller due to more pronounced sintering (see Table 10.1). The CaO conversion decreases when the CO_2 concentration increases. It is also apparent that the effect of increasing the reaction time levels off as CO_2 concentration increases. The negative effect of increasing CO_2 concentration is due to the carbonisation reaction which, at partial pressures higher than the equilibrium pressure, competes with SO_2 for any available CaO. When the CO_2 concentration increases, the effect upon the CaO conversion seems to level off and approaches a

zero order reaction with respect to CO_2. That the CaO-CO_2 reaction should be zero order with respect to CO_2 is supported by literature findings [142, 143, 146, 148, 149].
The effect of increasing reaction time levelling off is due to saturation of the material with CO_2, as also seen in Figure 12.7. The results in Figure 12.8 add to this, in that the rate at which saturation with CO_2 takes place depends on CO_2 concentration.

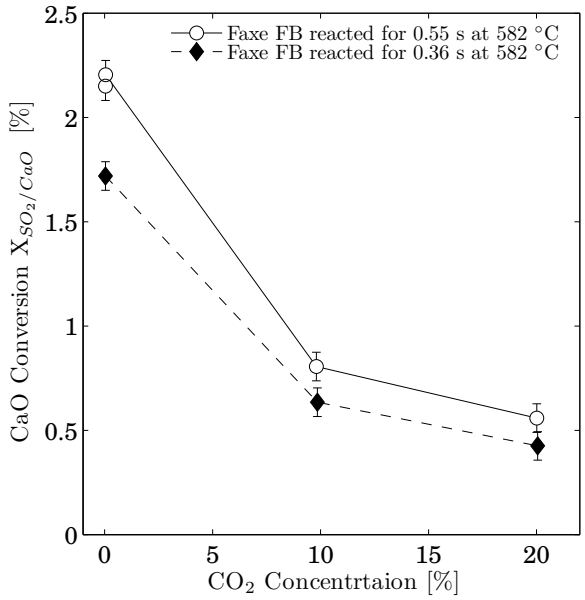

Figure 12.8: *CaO conversion as a function of CO_2 concentration in the reaction gas for partly calcined Faxe limestone.*

The results presented here contradict those found in the literature [103, 106, 125, 126], where no CO_2 effect was determined. The main reason for this discrepancy may be the reaction time used, which was significantly longer in the experiments reported in the literature. At the short reaction times used here, CO_2 will occupy sites that otherwise could react quickly with SO_2, and thereby CO_2 slows down the reaction. Conversely, at long reaction times the controlling mechanisms will be diffusion and reaction in a product layer of $CaCO_3$, $CaSO_3$ and $CaSO_4$. No discernible effect of CO_2 is observed, because the reaction between the formed $CaCO_3$ and SO_2 is much faster than the diffusion rate of SO_2 to the unreacted CaO core. The results presented here show clearly the pitfalls of predicting short reaction time outcomes solely from data gathered from long reaction time experiments.

12.5 The Influence of Temperature

Figure 12.9 shows CaO conversion as a function of reaction temperature for three different Faxe calcines. The CaO conversion in all cases increases with temperature, as would be expected. It is also observed that the slope of the data series increases with increasing surface area. This difference in inclination is a consequence of the CaO conversion being dependent on the surface area. If the reaction were controlled exclusively by pore diffusion, however, no difference in inclination would be expected.

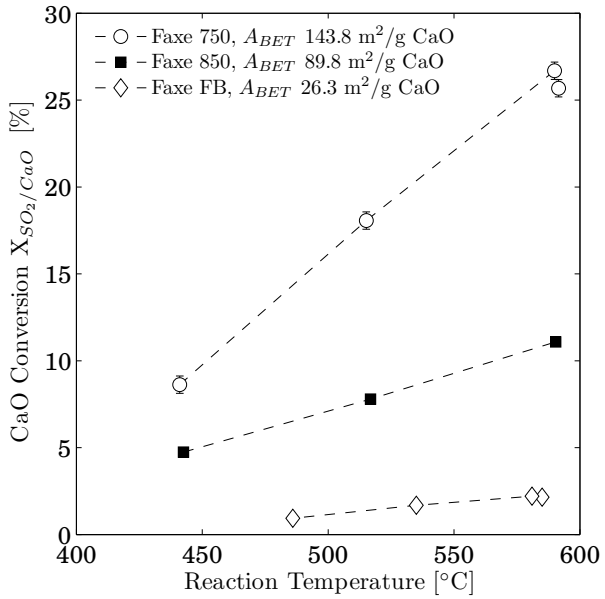

Figure 12.9: *CaO conversion as a function of reaction temperature. The experiments were carried out in atmospheric air, with a reaction time of 0.36 s.*

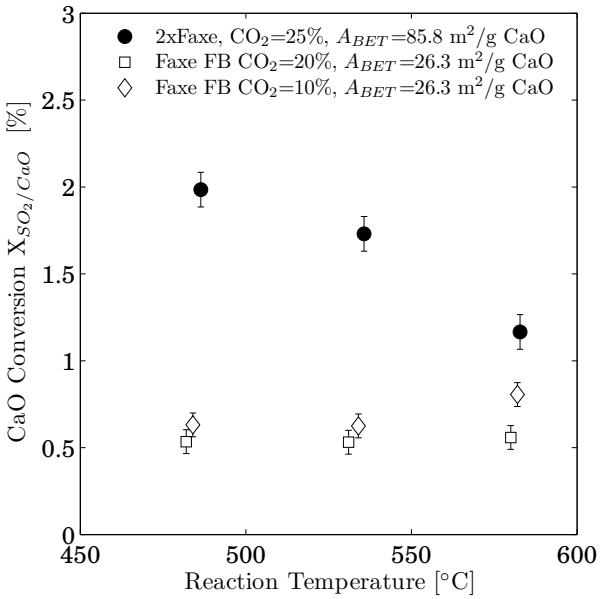

Figure 12.10: *CaO conversion as a function of reaction temperature. The experiments were carried out in different CO_2 concentrations, with a reaction time of 0.55 s.*

Figure 12.10 shows CaO conversion as a function of temperature when the reaction gas contains CO_2. Considering the Faxe FB results, there are no effects of increasing the temperature when the reaction gas contains 20 % CO_2, while a small increase is observed at the highest temperature for 10 % CO_2 in the reaction gas. In the case of 2xFaxe the temperature has a negative effect on the CaO conversion when 25 % of CO_2 is present in the reaction gas. Observing no effect, or even a negative effect of temperature, is different from the results in Figure 12.9, which were obtained in atmospheric air. The trends observed in Figure 12.10 are related closely to the pore size distributions in the two calcines. Figure 10.5 shows that flash calcined limestones, like 2xFaxe, have a secondary pore-system containing pores with a significantly smaller diameter than in Faxe FB. Thus, blockage of the secondary pore-system in 2xFaxe, and thereby a reduction of the reactive surface area, will increase faster with temperature than the reaction rates

of SO_2/CaO and SO_2/$CaCO_3$, here resulting in a negative temperature effect. The larger pore diameters found in Faxe FB result in that the temperature effect on pore blockage and on the SO_2/CaO and SO_2/$CaCO_3$ reaction rates cancel each other out in the case of 20 % CO_2 in the reaction gas. At 10 % CO_2, the temperature dependency of the reactions is apparently a little bit stronger than that of pore blockage, allowing a small increase in CaO conversion. In the literature [125, 127] only a positive temperature effect was reported, which is most likely due to longer reaction times and the more sintered CaO material used.

12.6 The Influence of Additives

From the literature it is known that the rate of CaO conversion can be increased by adding small amounts of different salts. Figure 12.11 shows the CaO conversion for Faxe limestone which has been flash calcined twice. Comparing the non-doped calcined limestone to limestones where 2 w/w % of either Na_2CO_3 or $CaCl_2$ have been added before calcination, we see that Na_2CO_3 seems to improve CaO conversion, while $CaCl_2$ seems to inhibit the process. The positive effect of Na_2CO_3 was also reported in the literature [123], although no effect of $CaCl_2$ was actually claimed. The positive effect, which is only evident for reaction times above 0.18 s, occurs, according to Stouffer and Yoon [123], because larger pores are formed during calcination. The larger pores should prevent pore blockage and thereby make more material available for reaction. It is also possible that Na compounds react directly with SO_2, since an Na conversion of 6 % has been observed when reacting pure $NaHCO_3$ with SO_2 at 534 °C in 25 % CO_2. The negative effect observed of $CaCl_2$ happens because this species promotes sintering and thereby the loss of reactive surface. However, more pronounced sintering also highlights that the reaction is less affected by pore blockage due to the carbonisation reaction. That sintering should be more pronounced for 2x$Faxe_{CaCl_2}$ is indicated by the linear increase in CaO conversion after 0.18, which was also observed when reacting CaO in atmospheric air, where pore blockage does not affect the results. For 2xFaxe and 2x$Faxe_{Na_2CO_3}$ a contentious decrease in the conversion rate is observed, which is most pronounced for 2xFaxe.

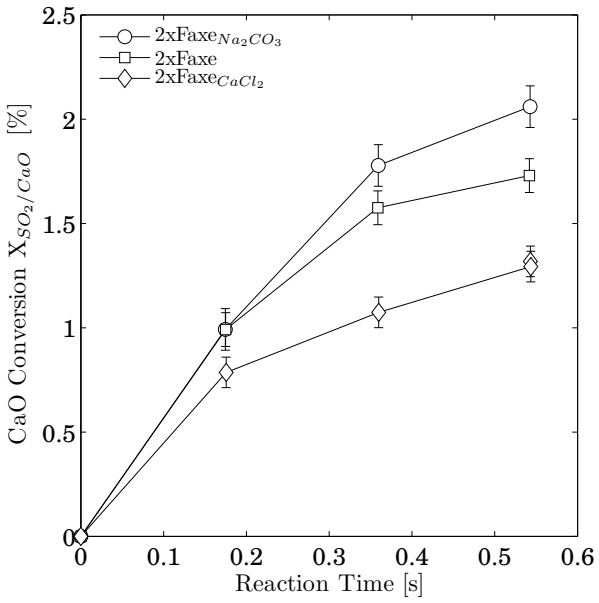

Figure 12.11: *CaO conversion as a function of the reaction time for Faxe limestone calcined twice, with and without additives. In all, 2 w/w % of the different additives was added before calcination. The reaction temperature was 534 °C and CO_2 content 25 %.*

12.7 The Influence of Oxygen and the Reaction Product from the CaO/SO_2 Reaction

Figure 12.12 shows the CaO conversion as a function of reaction temperature for CaO particles reacted with SO_2 in either an O_2 rich or O_2 poor atmosphere. Up to 590 °C there are no differences in the CaO conversions, indicating that up to this temperature oxygen concentration does not affect the reaction. At 640 °C the CaO conversion is higher in the oxygen-rich atmosphere than in the oxygen-poor. This difference becomes even more pronounced at 740 °C.
That oxygen does not affect the reaction below 600 °C indicates that the formed product(s) is stable. Above 640 °C the difference in CaO conversion occurs because the formed product in an oxygen-rich atmosphere is oxidised to $CaSO_4$, which is stable at these temperatures, while in the oxygen-poor atmosphere the product is unstable and decomposes. The observations here are in agreement with the literature [114, 115].

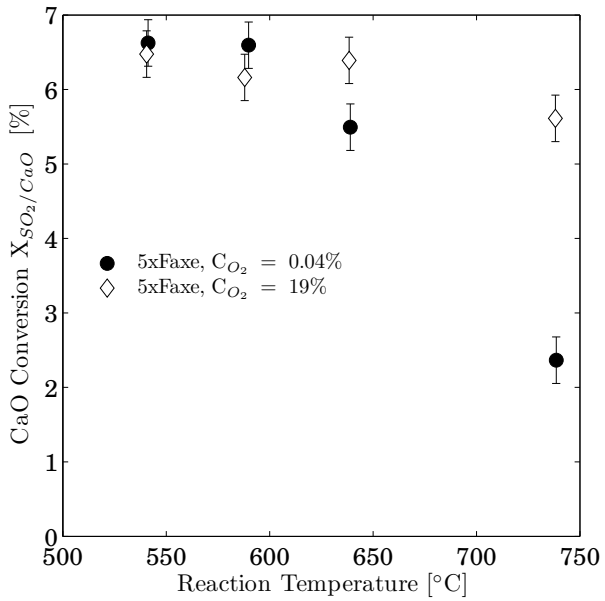

Figure 12.12: *CaO conversion as a function of the reaction temperature for either an oxygen-rich or oxygen-poor atmosphere. Reaction time 0.53 s.*

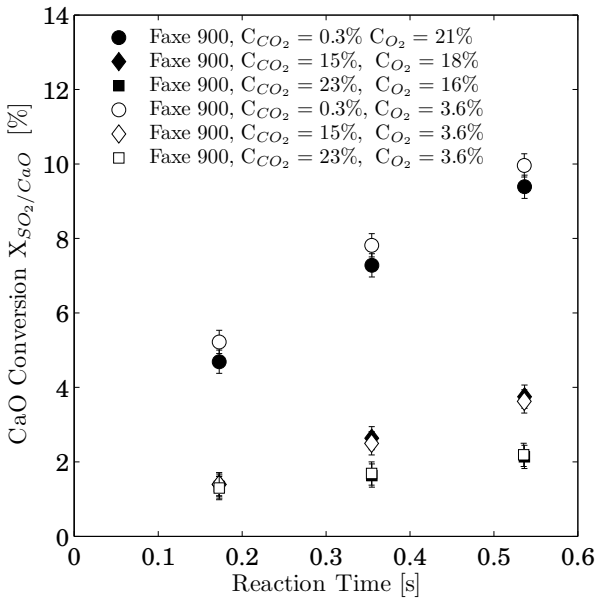

Figure 12.13: *CaO conversion as a function of the reaction time for Faxe reacted in different CO_2/O_2 concentrations at 544 °C.*

Figure 12.13 shows the CaO conversion as a function of the reaction time for CaO reacted in different concentrations of O_2 and CO_2. The O_2 concentration of 3.6 % is similar to that found in preheater towers, while the O_2 concentration between 16 and 21 % corresponds to atmospheric air as a balance gas. It is not possible to distinguish between points obtained in different O_2 concentrations when the CO_2 concentration is the same; nevertheless, a significant decrease in conversion is observed when the CO_2 concentration increases. Based on Figures 12.12 and 12.13 it can be concluded that the CaO/SO_2 reaction is zero order with respect to oxygen, with or without CO_2 in the gas phase, and below 600 °C, which is the temperature of interest in relation to SO_2 absorption in preheater towers.

Figure 12.14 shows the IR spectra recorded for Faxe 750 and the reaction product for Faxe 750 reacted with SO_2 at 515 °C and 590 °C. It is apparent that absorption peaks not found in the starting material are observed at 1100-1200 cm^{-1}, 900-1050 cm^{-1} and 650 cm^{-1} for Faxe 750 reacted at 590 °C. For Faxe 750 reacted at 515 °C only the peak at 900-1050 cm^{-1} is clear. Careful study of the figure reveals that a weak peak at 1000-1200 cm^{-1} is also present for the reaction product at 515 °C. The peak found at 650 cm^{-1} for the reaction product at 590 °C seems to be present only as a very weak peak at 515 °C, if present at all. In general, then, the peaks which differ from the reaction starting material are weaker at 515 °C than at 590 °C.

Comparing the three peaks observed for Faxe 750 reacted at 590 °C to the observations by, for instance, Ghardashkhani and Cooper [118], we find that the peaks at 650 cm^{-1} and 900-1050 cm^{-1} are due to the presence of $CaSO_3$, whereas the peak at 1100-1200 cm^{-1} is due to the presence of

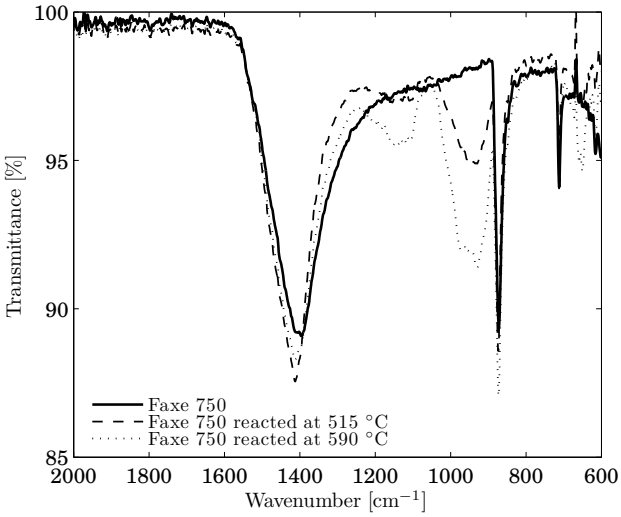

Figure 12.14: *IR spectrum for Faxe 750 and the reaction product of Faxe 750 reacted at different temperatures for 0.35 s in a CO_2-free atmosphere.*

$CaSO_4$. Thus, at 590 °C the SO_2/CaO reaction product is a mixture of $CaSO_3$ and $CaSO_4$. At 515 ° the near disappearance of the peak at 100-1200 cm^{-1}, combined with the presence of a peak at 900-1050 cm^{-1}, indicates that the product is basically $CaSO_3$ with traces of $CaSO_4$. Generally, peaks are weaker at 515 °, accounting for the disappearance of the peak at 650 cm^{-1}.
If the intensities of the peaks are taken as an indication of the amount of a given product, the dominating product will, in both cases, be $CaSO_3$. The reaction product at both temperatures is a mixture of $CaSO_3$ and $CaSO_4$, with the main product being $CaSO_3$, corresponds well with the findings by other authors [85, 116–119] using IR measurements to identify their reaction products.

Chapter 13

Summary of Experimental Results

The experimental part of this thesis focused on how CaO react with SO_2 at reaction times shorter than 1 second. It was shown that the observed results were limited by external and internal mass transfer. The experiments further demonstrated that the addition of CO_2 to the reaction atmosphere strongly inhibits the conversion with respect to SO_2 This inhibition occurs because CO_2 reacts with CaO and forms $CaCO_3$, which then reacts slower with SO_2 than CaO. In addition, $CaCO_3$ also causes pore blockage, resulting in a serious reduction of reactive surface area. The CaO experiments indicated that increased surface area has a positive effect on CaO conversion. Increasing temperature showed a positive effect in experiments conducted in atmospheric air, while no effect or even a negative effect were observed at high concentrations of CO_2. One explanation for this phenomenon is that a reduction in surface area counteracts the positive effect of temperature. A number of attempts were made to produce calcines with a large surface area. It transpired that flash calcination at low temperatures resulted in the largest surface area, but in general it is difficult to produce calcines from $CaCO_3$ with a large surface area because the calcination process needs relatively high temperatures and CO_2 promotes sintering of the formed CaO.

Based on the experiments, the following conclusions in relation to cement plants can be reached. In the literature it has been stated that CaO recirculating in the preheater can influence SO_2 emission. Based on the results obtained it is evident that CaO recirculating in the preheater does not contribute to SO_2 absorption in the top cyclones, where SO_2 formation takes place, because any CaO experiencing carbonating conditions will react instantaneously with CO_2 and form $CaCO_3$, with a significant decline in the SO_2 absorption rate as a consequence. That CaO does not contribute is further supported by the very low specific surface area of hot meal (Table 8.2). The low surface area also explains why the recirculation of calcined material to the top stages is not an ideal solution for dealing with SO_2 emissions.

Chapter 14

Modelling of the CaO/SO_2 Reaction

The experimental results show that a model for the CaO/SO_2 reaction in atmospheric air must take the following phenomena into account:

- Gas film diffusion of SO_2
- Diffusion of SO_2 in the interior of the particle
- Reaction between CaO and SO_2 in the interior of the particle. Here it is assumed that the reaction product is $CaSO_3$. It is chosen as the reaction product because, as discussed in section 12.7, $CaSO_3$ appears to be the main product of the reaction.

A model which can describe the observed CaO conversion when CO_2 is present in the reaction gas must take the phenomena listed above into account for CO_2 and its product, too. Furthermore, pore blocking caused by the formation of $CaCO_3$ and the $CaCO_3/SO_2$ reaction must be included in a model describing SO_2 absorption when CO_2 is present in the reaction gas. Achieving this requires a larger amount of data than available here for the $CaO/CO_2/SO_2$ reaction system. Therefore, only the CaO/SO_2 reaction in atmospheric air will be considered.
A suitable model must take the phenomena listed above into consideration. A model which can do that is the grain model, as used by, for example, Hartman and Coughlin [132].

14.1 Gas Phase Diffusion

Figure 14.1 illustrates how a CaO particle is built up. The particle structure can be divided into two levels, the first of which consists of clusters of non-porous CaO grains. These clusters were, before calcination, non-porous grains of $CaCO_3$ which in the calcination process become a porous cluster of non-porous CaO grains. The void between the clusters of CaO grains is denoted the primary pore-system. The second level is comprised of clusters of CaO which are approximately the same size as the originally non-porous $CaCO_3$ grains. The void between the non-porous CaO grains is denoted the secondary pore-system. It is here assumed that internal

diffusion limitations are situated exclusively within the primary pore-system. This is justified by the fact that the size of the CaO clusters is significantly smaller than the superior particle.

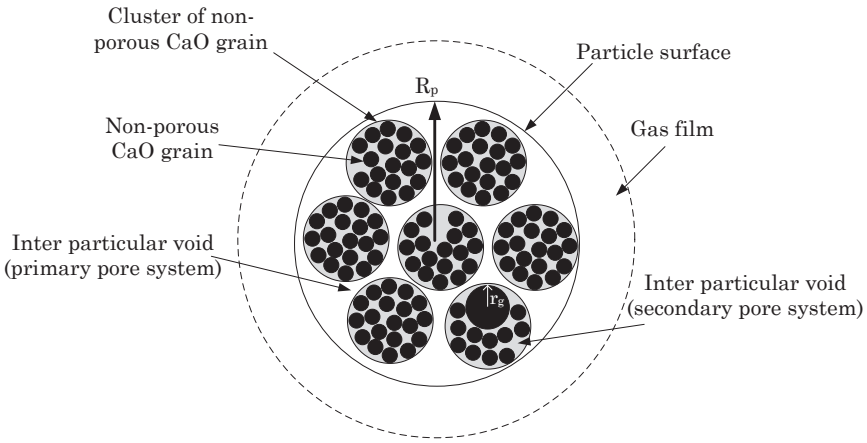

Figure 14.1: *Schematic drawing of how a CaO particle is build up.*

Equation 14.1 expresses diffusion in the primary pore-system, assuming that the large particles are spheres and concentration gradients exist only in the radial direction.

$$\frac{\partial C_{SO_2}}{\partial t} = \frac{1}{R^2}\frac{\partial}{\partial R}\left(D_{e,SO2}(R)\cdot R^2\frac{\partial C_{SO_2}}{\partial R}\right) + r_{SO2}(R) \tag{14.1}$$

When using the grain model, Hartman and Coughlin [132] assume that the diffusion of SO_2 in the interior of the particle is a pseudo steady-state process. However, comparison between a pseudo steady-state model and a time-dependent model has shown that this assumption is not valid in this instance.
The initial and boundary conditions for equation 14.1 are as follows:

$$C_{SO_2} = 0 \;\; at \;\; t = 0 \tag{14.2}$$

$$\frac{\partial C_{SO_2}}{\partial R} = 0 \;\; at \;\; R = 0 \tag{14.3}$$

$$D_{e,SO_2}(R)\frac{\partial C_{SO_2}}{\partial R}\Big|_{R=R_p} = K_{g,SO_2}\cdot\left(C_{SO_2,bulk} - C_{SO_2,R_{surface}}\right) \;\; at \;\; R = R_p \tag{14.4}$$

The Robin boundary condition in equation 14.4 accounts for diffusion limitations in the gas film surrounding the particle. In the modelling approach used by Hartman and Coughlin [132] it was assumed that the SO_2 concentration at the particle surface was equal to the bulk concentration. However, as shown in Chapter 11, this is not a valid assumption here.
Equation 14.1 and its boundary conditions are made dimensionless by introducing the following

dimensionless variables: $\tau = \frac{t}{t_r}$, $Z = \frac{R}{R_p}$, $X_{SO_2} = \frac{C_{SO_2}}{C_{SO_2,bulk}}$ resulting in the dimensionless equation 14.5 for the diffusion of SO_2 in the gas phase, with the dimensionless initial and boundary conditions described by equation 14.6-14.8.

$$\frac{\partial X_{SO_2}}{\partial \tau} = \frac{t_r}{R_p^2}\frac{1}{Z^2}\frac{\partial}{\partial Z}\left(D_{e,SO2} \cdot Z^2 \frac{\partial X_{SO_2}}{\partial Z}\right) + \frac{t_r}{C_{SO_2,bulk}} \cdot r_{SO2} \tag{14.5}$$

$$X_{SO_2} = 0 \;\; at \;\; \tau = 0 \tag{14.6}$$

$$\frac{\partial X_{SO_2}}{\partial Z} = 0 \;\; at \;\; Z = 0 \tag{14.7}$$

$$\frac{\partial X_{SO_2}}{\partial Z}\,|_{Z=1} = \frac{K_{g,SO_2} \cdot R_p}{D_{e,SO_2}} \cdot (1 - X_{SO_2,Z=1}) = Bi_m \cdot (1 - X_{SO_2,Z=1}) \;\; at \;\; Z = 1 \tag{14.8}$$

It is noted that in the Robin boundary condition (14.8) a mass transfer Biot number (Bi_m) appears when the equation system is made dimensionless.

14.2 CaO/SO_2 Reaction

The CaO/SO_2 reaction at the CaO grains is assumed to proceed through a shrinking core model with the diffusion of SO_2 in the solid product layer and reaction with CaO at the interface between the solid product layer and the unreacted core, as illustrated in Figure 14.2.

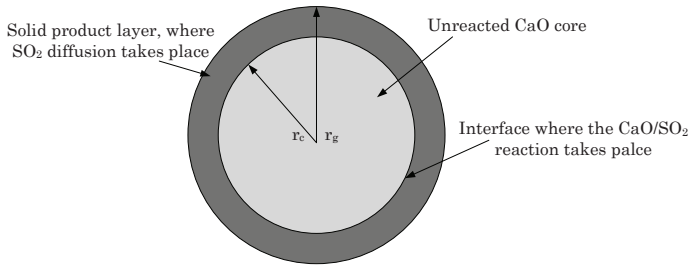

Figure 14.2: *Schematic drawing of how the CaO/SO_2 reaction takes place in solid CaO grains.*

Diffusion in the solid product layer is assumed to be a pseudo steady-state process, where only a concentration gradient in the radial direction exists. It is further assumed that the CaO grains are small enough to experience a uniform concentration of SO_2 at the surface, equal to the gas concentration at position R where the grain is located. Moreover, no gas film exists around the solid grains.

Equation 14.9 describes the diffusion of SO_2 in the solid product layer with the boundary conditions stated in equation 14.10 and 14.11

$$0 = \frac{\partial}{\partial r}\left(r^2 \frac{\partial C_{SO_2,g}}{\partial r}\right) \quad r_c < r < r_g \tag{14.9}$$

$$C_{SO_2,g} = C_{SO_2} \quad at \quad r = r_g \tag{14.10}$$

$$D_{SO_2,s} \cdot \frac{\partial C_{SO_2,g}}{\partial r}\,|_{r=r_c} = K_{SO_2/CaO} \cdot C_{SO_2,c} \quad at \quad r = r_c \tag{14.11}$$

Here, $C_{SO_2,g}$ is the SO_2 concentration in the solid product layer, $D_{SO_2,s}$ is the solid-state diffusion coefficient for SO_2 in the solid product layer, $K_{SO_2/CaO}$ is the reaction constant for the CaO/SO_2 reaction and $C_{SO_2,c}$ is the SO_2 concentration at the interface between the solid product layer and the unreacted core.
The boundary condition in equation 14.11 states that the CaO/SO_2 reaction is a first-order reaction with respect to SO_2. In the literature [105, 112, 113] some authors have obtained reaction orders other than one. However, since no data is available for the reaction order at very short reaction times for single grains, a reaction order of one with respect to SO_2 is chosen. Another reason for not using a reaction order from the literature is that the extremely fast initial reaction observed here raises doubts about whether the literature data was actually obtained under conditions where diffusion limitations could be excluded (see section 12.3).
Equation 14.9 is a homogeneous differential equation, which can be solved analytically with the concentration at the interface at $r = r_c$ given by equation 14.12.

$$C_{SO_2,c} = \frac{C_{SO_2} \cdot D_{SO_2,s}}{D_{SO_2,s} + K_{SO_2/CaO} \cdot r_c \cdot \left(1 - \frac{r_c}{r_g}\right)} \tag{14.12}$$

The rate at which the unreacted core shrinks is equal to the rate at which SO_2 is consumed at the product layer/unreacted core interface and can be expressed by equation 14.13.

$$\overline{\rho}_{CaO} \cdot \frac{\partial r_c}{\partial t} = -K_{SO_2/CaO} \cdot C_{SO_2,c} = \frac{C_{SO_2}}{\frac{1}{K_{SO_2/CaO}} + \frac{r_c}{D_{SO_2,s}} \cdot \left(1 - \frac{r_c}{r_g}\right)} \tag{14.13}$$

which has the following initial condition.

$$r_c = r_g \quad at \quad t = 0 \tag{14.14}$$

Equations 14.13 and 14.14 are made dimensionless by introducing the dimensionless variable $Y = \frac{r_c}{r_g}$, resulting in the following dimensionless equations:

$$\frac{\partial Y}{\partial \tau} = -\frac{t_r \cdot C_{SO_2,bulk}}{\overline{\rho}_{CaO}} \cdot \frac{X_{SO_2}}{\frac{r_g}{K_{SO_2/CaO}} + \frac{r_g^2}{D_{SO_2,s}} \cdot Y \cdot (1 - Y)} \tag{14.15}$$

$$Y = 1 \quad at \quad \tau = 0 \tag{14.16}$$

Based on geometrical considerations it can be demonstrated that the consumption of SO_2 in the gas phase relates to the shrinking core radius through equation 14.17, where ϕ_{int} denotes the porosity when the reaction starts.

$$r_{SO_2} = \frac{3 \cdot (1 - \phi_{int}) \cdot r_c^2 \cdot \overline{\rho}_{CaO}}{r_g^3} \cdot \frac{\partial r_c}{\partial t} \tag{14.17}$$

This leads to the following dimensionless expression for the SO_2 consumed by the reaction.

$$r_{SO_2} = -\frac{3 \cdot (1 - \phi_{int}) \cdot C_{SO_2,bulk} \cdot Y^2 \cdot X_{SO_2}}{\frac{r_g}{K_{SO_2/CaO}} + \frac{r_g^2}{D_{SO_2,s}} \cdot Y \cdot (1 - Y)} \tag{14.18}$$

14.3 CaO Conversion

The conversion of a single CaO grain ($X_{SO_2/CaO,g}$) is, in dimensionless terms, described by equation 14.19.

$$X_{SO_2/CaO,g} = 1 - Y^3 \tag{14.19}$$

The conversion of an entire particle ($X_{SO_2/CaO}$), with radius R_p, is calculated by integrating over the particle radius, as expressed by equation 14.20

$$X_{SO_2/CaO} = \frac{3}{R_p^3} \int_0^{R_p} R^2 \cdot X_{SO_2/CaO,g} dR = 3 \cdot \int_0^1 Z^2 \cdot (1 - Y^3) dZ \tag{14.20}$$

14.4 Input Parameters

Effective Pore Diffusion Coefficient, D_{e,SO_2}

The effective pore diffusion coefficient is calculated from equation 14.21. When calculating this coefficient, Knudsen diffusion is neglected because the average primary pore diameter is about 0.5 μm.

$$D_{e,SO_2} = \frac{\phi(Y)}{\tau_p} \cdot D_{SO_2} = \frac{\phi(Y)}{\tau_p} \cdot 1.1 \cdot 10^{-5} \left(\frac{T}{273.15} \right)^{1.81} \quad \left[\frac{m^2}{s} \right] \tag{14.21}$$

The expression for D_{SO_2} is taken from Massman [158]. The tortuosity factor (τ_p) has been investigated by different authors [159–162], who found that a value for materials such as $CaCO_3$ and CaO of 1.5 is suitable.

As the reaction proceeds, the particle porosity will decrease due to the larger molar volume of $CaSO_3$ compared to CaO. In order to account for this, the porosity is written as a function of the grain conversion, as seen in equation 14.22.

$$\phi(Y) = 1 - \frac{\rho_{CaO} \cdot (1 - \phi_{int})}{M_{CaO}} \cdot \left(V_{CaO} + \left(1 - Y^3 \right) \cdot (V_{CaSO_3} - V_{CaO}) \right) \tag{14.22}$$

Here, V_{CaO} and V_{CaSO_3} denotes the molar volume of CaO and $CaSO_3$, respectively.

The value of V_{CaO} is, according to Wang and Bjerle [131], 16.76·10^{-6} m^3/mole, while the value of V_{CaSO_3} is estimated from Arai et al. [163] at 45.45·10^{-6} m^3/mole.
Equation 14.22 does not distinguish between pore sizes, and in the calculations made here it is assumed that porosity is equally distributed within the particles. In order to account for pore blockage, equation 14.22 is subjected to the following conditions.

$$\phi(Y) = \begin{cases} 1 - f(Y) & if \quad f(Y) < 1 \\ 0 & if \quad f(Y) \geq 1 \end{cases}$$

SO_2 Bulk Concentration, $C_{SO_2,bulk}$
The bulk concentration of SO_2 is calculated from equation 14.23, assuming that the reaction gas is an ideal gas.

$$C_{SO_2,bulk} = x_{SO_2,bulk} \cdot \frac{P}{R_{gas} \cdot T} \tag{14.23}$$

Reaction Time, t_r
The reaction time is set equal to 0.6 s. This reaction time covers all reaction times used, while still ensuring a good time discretisation using as few calculations as possible.

Grain Radius, r_g
Since no size distribution for the grain radius is known, an average grain radius is used. It is calculated from equation 14.24 using the BET surface area.

$$r_g = \frac{3}{\rho_{CaO} \cdot A_{BET}} \tag{14.24}$$

Particle Radius, R_p
The particle radius is used as a discrete function, meaning that the CaO conversion is calculated for a finite number of particle sizes and subsequently weighted in accordance with the mass fraction of material found at a given size. The calculations are based on five different particle radii, which have been found to give satisfactorily results.

Mass Transfer Biot Number, Bi_m
The mass transfer Biot number which appears in equation 14.8 can be rewritten, as shown in equation 14.25.

$$Bi_m = \frac{K_{g,SO_2} \cdot R_p}{D_{e,SO_2}} = \frac{K_{g,SO_2} \cdot R_p}{D_{SO_2}} \cdot \frac{\tau_p}{\phi(Y)} = \frac{Sh}{2} \cdot \frac{\tau_p}{\phi(Y)} \tag{14.25}$$

The Sherwood number appearing in equation 14.25 is here set equal to 2, since the experiments were conducted under the assumption that the particles are spherical and at rest compared to

the gas, and that they do not interact.

Solid-State Diffusion Coefficient and CaO/SO_2 Reaction Constant, $D_{SO_2,s}$ and $K_{SO_2/CaO}$
The solid-state diffusion coefficient for SO_2 in the product layer, as well as the reaction rate constant for the SO_2/CaO reaction, are both used as fitting parameters.

14.5 Solution of Model

The dimensionless model, which consists of equation 14.5, 14.15 and 14.18, as well as the appertaining initial and boundary conditions, combine to make up a partial differential equation system. In this thesis it is solved by the partial differential equation solver (*pdepe*) in Matlab, which uses a Finite Difference Method for solving partial differential equation systems. The numbers of discretisation points for the particle radius are chosen as 50, whereas the time discretisation consists of 62 points, with a refined discretisation in the initial phase of the reaction. From the solution of the equation system an overall particle conversion for each particle size is calculated from equation 14.20 by using the trapezoidal method.
As stated earlier, $D_{SO_2,s}$ and $K_{SO_2/CaO}$ is to be estimated from the experimental data obtained by investigating the CaO/SO_2 reaction. In order to achieve this the Matlab function *fminbnd* is used. The *fminbnd* function minimises a function, allowing the user to state upper and lower boundaries for the parameter to be estimated. Here, the possibility of excluding negative values is used, since they do not make sense from a physical point of view. The function that *fminbnd* is to minimize is the sum of squares expressed by equation 14.26. Here, the last summation shows that the conversion of each particle size is to be weighted and summed in order to obtain the average conversion, which is the one that is measured.

$$SS = \sum_{p=1}^{n} \left(X_{SO_2/CaO,measured} - \sum_{i=1}^{m} Q_{i,particle} \cdot X_{SO_2/CaO,calc.} \right) \tag{14.26}$$

14.6 Estimation of the Reaction Constant, $K_{SO_2/CaO}$

Figure 14.3 shows the normalised sum of squares as a function of the reaction constant, and Figure 14.4 shows the normalised solid-state diffusion coefficient as a function of the reaction constant. The normalisation is undertaken by dividing all data points in a data series by the smallest value in the data series. In this manner the normalised value of the smallest value will become 1 and all other values will be 1 or larger. In the case of the normalised sum of squares the best fit to data will thus be found at a normalised sum of square value of 1.

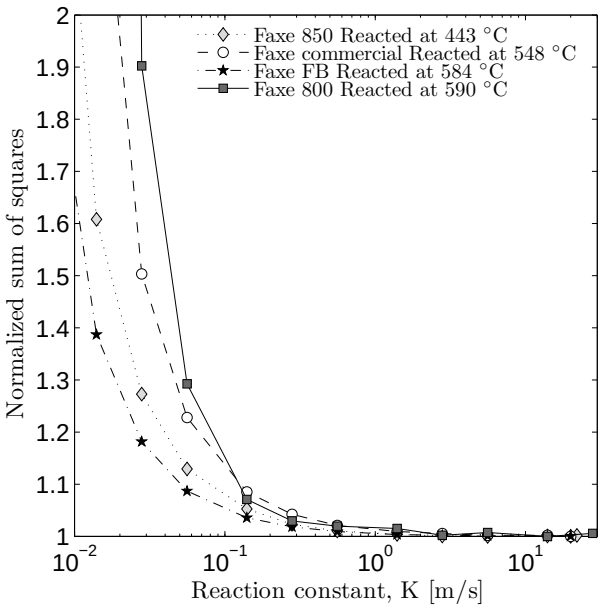

Figure 14.3: *Normalised sum of squares as a function of the reaction constant.*

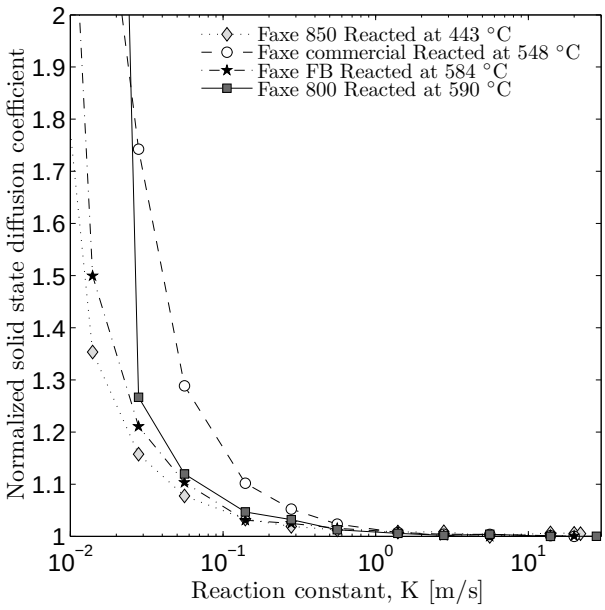

Figure 14.4: *Normalised solid-state diffusion coefficient as a function of the reaction constant.*

It is apparent that the normalised sum of squares for all four data series, even though they are obtained at different temperatures and with different calcines, approaches 1 when $K_{SO_2/CaO}$ increases and it is 1 when the reaction constant is above 3 m/s. That the normalised sum of squares approaches a minimum value when $K_{SO_2/CaO}$ increases indicates that the reaction constant cannot be determined from our data, since diffusion within the solid product layer is exclusively rate-determining. Considering Figure 14.4 the same behaviour is observed, with the normalised diffusion coefficient approaching a constant value if the reaction constant becomes larger than 1 m/s. This behaviour also indicates that the conversion is determined by solid-state diffusion in the grain product layer. From equation 14.15 it is evident that both $K_{SO_2/CaO}$ and D_{s,SO_2} enter into the denominator of the second term. In order to determine at what value of Y the solid-state diffusion is becoming dominating, the two terms are put equal, resulting in equation 14.27.

$$\frac{r_g}{K_{SO_2/CaO}} = \frac{r_g^2}{D_{s,SO_2}} \cdot Y \cdot (1 - Y) \tag{14.27}$$

This equation is solved for Y, using a value for r_g of 10^{-8} m, corresponding to a surface area of 90 m^2/g. D_{s,SO_2} is put equal to $2{\cdot}10^{-13}$, based on data from Bhatia and Perlmutter [129], at 590 °C. The value of $K_{SO_2/CaO}$, on the basis of Figure 14.3, is chosen as 10 m/s. Using these numbers for solving equation 14.27 it can be established that Y is equal to 0.999998, which corresponds to a CaO conversion of $6 \cdot 10^{-4}$ %. This result implies that up to a conversion of $6 \cdot 10^{-4}$%, $r_g/K_{SO_2/CaO}$ will be the dominating term. At higher CaO conversions the $r_g^2/D_{s,SO_2}$ term will dominate the CaO conversion rate. Comparing the calculated CaO conversion to the results in Figure 12.5, it is evident that, in all cases, the measured CaO conversion is at least 5000 times

higher than the one calculated. This shows that the term $r_g/K_{SO_2/CaO}$ is irrelevant when fitting the reaction model to the experimental data, using a large value for $K_{SO_2/CaO}$. Furthermore, it explains why both the normalised sum of squares and normalised solid-state diffusion coefficient approach a constant value when $K_{SO_2/CaO}$ increases.
Assuming that the chemical reaction between CaO and SO_2 controls the CaO conversion for all CaO surface molecules, the mole fraction of CaO, which is controlled by the chemical reaction, can be estimated from geometrical considerations. Here it is assumed that the spherical CaO grains are made up of cubic unit cells of CaO, which have an edge length of $2.4{\cdot}10^{-10}$ m and contain four CaO molecules. Thus, the fraction of CaO molecules situated at the surface is calculated by dividing the CaO edge length by the grain radius and then multiplying by 1.5. The CaO material used for the experiments shown in Figure 12.5 has an average CaO grain radius, calculated from equation 14.24, of between $6.4 \cdot 10^{-9}$m and $1.05 \cdot 10^{-8}$m. This corresponds to, that 3.5-5.6% of the CaO molecules are found as surface molecules. Which is why it would be expected, at least at short reaction times, that the SO_2/CaO reaction would contribute significantly to the observed CaO conversion. From Figure 14.3 it can be concluded that the best fits to data are found when the reaction constant is so large that the chemical reaction is insignificant in the model. Since the best fit of data seems to be at large values of $K_{SO_2/CaO}$, this constant is put equal to 10 m/s and assumed temperature-independent.

14.7 Estimation of the Solid-State Diffusion Coefficient, D_{s,SO_2}

In order to increase the number of data points used for estimating the solid-state diffusion coefficient, it is assumed that the temperature dependency of D_{s,SO_2} follows an Arrhenius expression, since we are considering diffusion in an essentially massive product layer. This means that D_{s,SO_2} can be expressed as seen in equation 14.28.

$$D_{s,SO_2} = D_0 \cdot exp\left(-\psi \cdot \frac{T_{ref}}{T}\right) \tag{14.28}$$

Here, ψ is equal to $E_a/(R \cdot T_{ref})$. In this way data series obtained at different temperatures, but at otherwise similar conditions, can be fitted to the model simultaneously, with D_0 and ψ as temperature-independent parameters that need to be estimated. The reference temperature (T_{ref}) is here chosen as 773 K. This way of estimating D_{s,SO_2} increases the number of data points in each data series about three times, while the number of fitting parameters increase from one to two, making the influence of potential outliers smaller.
Figure 14.5 shows the normalised sum of squares as a function of the activation energy for the five data series fitted to the model. The normalised sum of squares is also here calculated by dividing the data series by the smallest sum of square value, meaning that the minimum sum of square is found at 1.

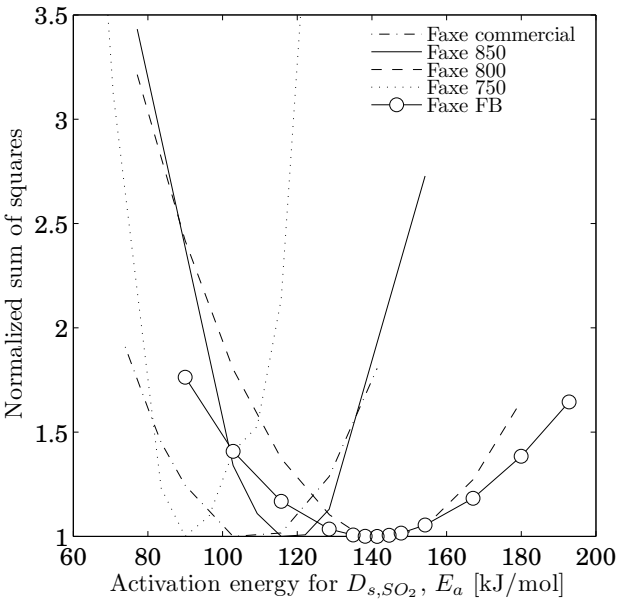

Figure 14.5: *Normalised sum of squares as a function of the activation energy for D_{s,SO_2}.*

CaO Source	D_0
	m^2/s
Faxe Commercial	$1.990 \cdot 10^{-5}$
Faxe 850	$1.109 \cdot 10^{-4}$
Faxe 800	$1.923 \cdot 10^{-5}$
Faxe 750	$7.340 \cdot 10^{-7}$
Faxe FB	$7.457 \cdot 10^{-5}$

Table 14.1: *Values obtained for D_0 when fitting the model using an activation energy of 115 kJ/mole.*

This figure shows that the minimum value for the normalised sum of squares is situated between 90 and 140 kJ/mol depending on the material used. It would have been expected that the different calcines, which originate from the same limestone, would have similar reaction properties compared to SO_2 and thereby similar activation energies, which appears not to be the case. However, it is also noted that most data series have a large range, where the normalised sum of squares does not deviate much from the minimum value observed. Considering an activation energy of 115 kJ/mol, only Faxe 750 has a normalised sum of squares value larger than 1.5.
Table 14.1 shows the values obtained for D_0 when fitting the model using an activation energy of 115 kJ/mol. It is here observed that the D_0 values for the different calcines (except Faxe 750) are within an order of magnitude, with the value for Faxe 750 about two orders of magnitudes lower. The pre-exponential factor in an Arrhenius expression can be interpreted as the number of occurrences which result in the process taking place. If the values of D_0 is interpreted in this context, an explanation for the different values observed for D_0, at an activation energy of 115 kJ/mole, can be due to that solid-state diffusion initiates easier at certain surface sites than at others.
The large deviation among the activation energies is also seen in the activation energies reported in the literature [104, 105, 111, 112, 129, 130], which range from 80 and 153 kJ/mol (Table 6.1). In addition, the range for the D_0 values obtained here is in agreement with those reported in the literature [104, 105, 111, 112, 129, 130], where values between $1.2{\cdot}10^{-5}$ m^2/s and $5.6{\cdot}10^{-9}$ m^2/s were reported.
What is also observed here, but not in the literature, is that a wide range of activation energies

gives almost equally good fits to the different data series.

14.8 Simulation Results

Figure 14.6-14.8 shows experimental data and model results for Faxe 750, Faxe 850 and Faxe FB, respectively. In the modelling of the data series an activation energy of 115 kJ/mol and the material-specific value of D_0 from Table 14.1 were used.

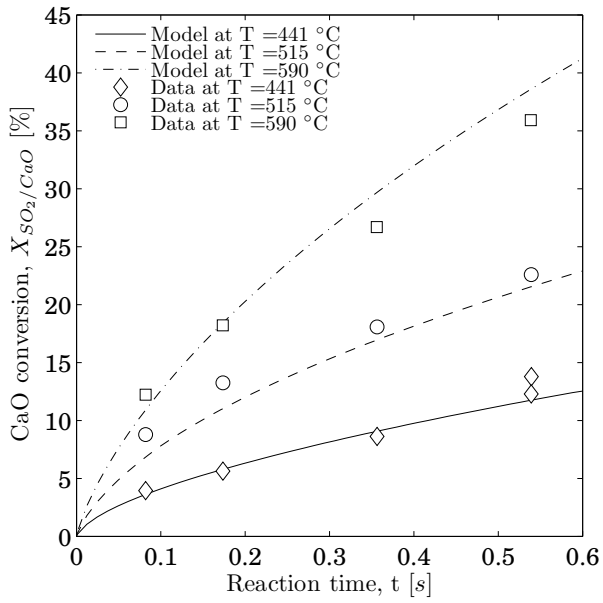

Figure 14.6: *Experimental observed conversion and conversion predicted by the model for Faxe 750.*

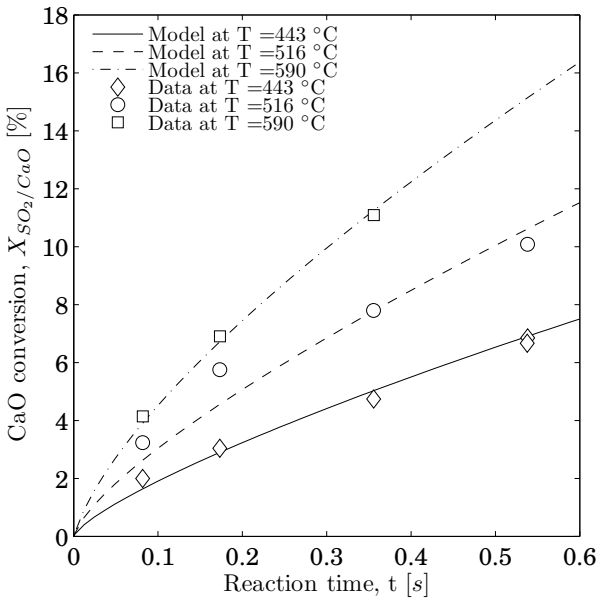

Figure 14.7: *Experimental observed conversion and conversion predicted by the model for Faxe 850.*

Figure 14.6-14.8 shows that the model predicts all data series very well, even though E_a are fixed and only D_0 is estimated. Especially the good agreement between measured and simulated conversion in Figure 14.6 should be noted, since the normalised sum of square value for Faxe 750 was the largest.

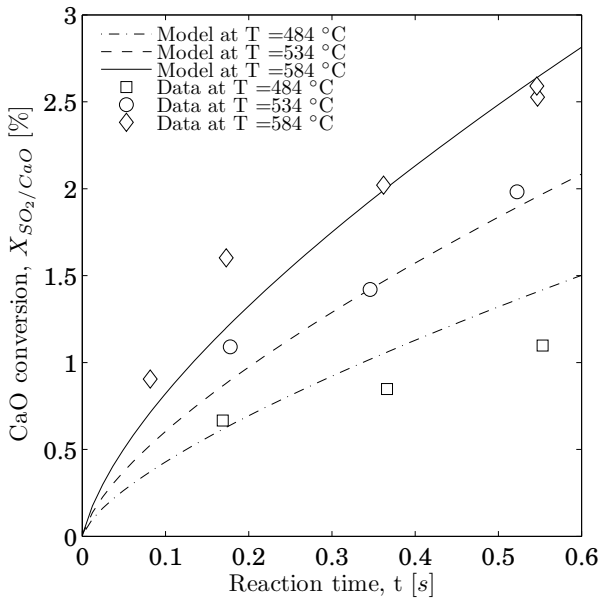

Figure 14.8: *Experimental observed conversion and conversion predicted by the model for Faxe FB.*

14.9 Summary

The experimental results showed that the model had to account for both external and internal diffusion as well as chemical reaction. It was decided to focus on the CaO/SO_2 reaction and leave out the CaO/CO_2 reaction, since only a limited amount of data was available. The modelling was based on the grain model of Hartman and Coughlin [132], with reaction between CaO and SO_2 at the interface between the product layer and the unreacted core of CaO. The modelling showed that the conversion only depends on the solid-state diffusion of SO_2 in the product layer $CaSO_3$, even though calculations showed that the chemical reaction should be important for the observed CaO conversions. Thus, the only fitting parameter of any influence for the calculated CaO conversion turned out to be the solid-state diffusion coefficient. Even though the calcines used were based on the same limestone, activation energies between 90 and 140 kJ/mole were obtained. However, a careful analysis of the data fitting showed that an activation energy of 115 kJ/mole could describe all data series very satisfactorily. The variations in activation energies are similar to what is reported in the literature, which could give reason to believe that some of the variation among the literature activation energies could be due to uncertainties in the experimental data used for its estimation.

That the chemical reaction turned out to be insignificant, although it should not be the case, shows that the surface processes taking place in the CaO/SO_2 reaction are not well understood.

Chapter 15

Modelling a Preheater Tower

Predicting emissions caused by the oxidation of species such aspyrite and carbonaceous matter is a major challenge due to the extremely complicated flow pattern in preheater cyclones. In this chapter a model for predicting emissions from a preheater tower will be established and validated against SO_2 emission data from full-scale plants.

15.1 Model Boundaries

Figure 15.1 shows a preheater tower, with the dotted line showing the model boundary. The model boundary encapsulates four cyclone stages, but will be established for a preheater tower with N number of cyclone stages, noting that N refers to the number of cyclone stages included in the model and not to the total number of cyclone stages, which are N+1. A cyclone stage includes the riser duct and the cyclone, and they are numbered from the top downwards. The calciner and calciner cyclone stage are omitted because the high temperature (about 850 °C) and the large amount of $CaO/CaCO_3$ lead to instantaneous absorption of any SO_2 formed. The model consists of the following three parts, which are solved independently and in the sequence stated.

- Total mass balance
- Energy balance
- Cyclone stage model, with reactions

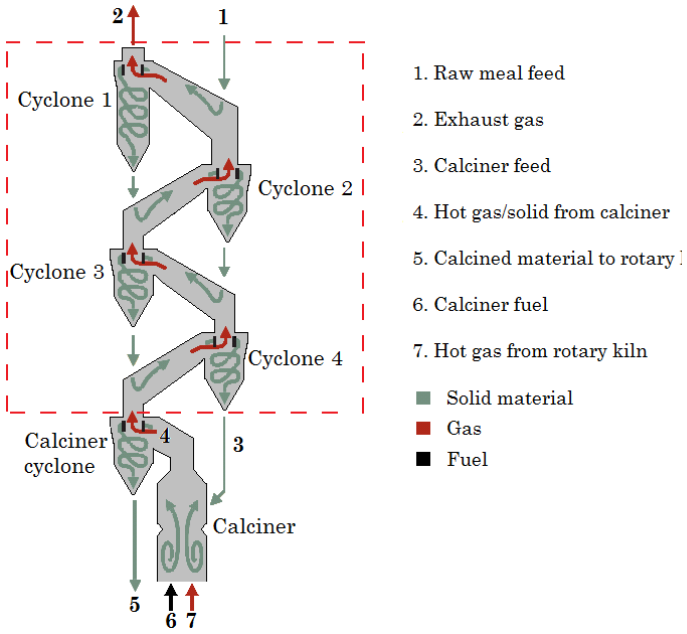

Figure 15.1: *Outline of the boundary for modelling a preheater tower. The dotted line shows the model boundary.*

15.2 Total Mass Balance

Figure 15.2 shows a schematic drawing of cyclone stage j with relevant inlet and outlet streams. It is assumed that gas only goes upwards, i.e. from higher to lower numbered cyclone stages, whereas solids can travel both upwards and downwards. A total mass balance for both gas and solids for cyclone stage j is established according to the general balance in equation 15.1. It is here assumed that the amount of gas and solid are constant, which can be justified because only minor compounds like pyrite and carbonaceous matters react in the top stages of the preheater, and since they in total often constitute less than 1 w/w % of the raw meal it is reasonable to assume that oxidation is negligible. It is well known that calcined raw meal can recirculate from the calciner cyclone to the bottom cyclone, where it can then carbonate. However, when setting up the total mass balance it is assumed that this reaction has taken place before the calcined material enters the bottom cyclone. Finally, it is assumed that all cyclones are airtight, meaning that false air does not affect the gas flow.

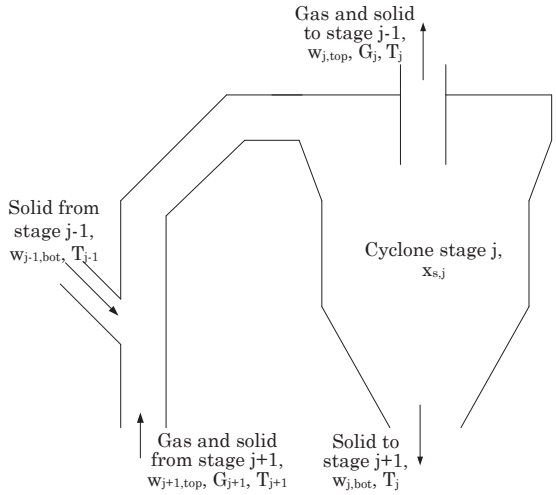

Figure 15.2: *Schematic drawing of cyclone stage j, with relevant inlet and outlet streams and temperatures.*

$$In = Out + Accumulated \tag{15.1}$$

When setting up the total mass balance, it is assumed that the system is at steady state, which results in the accumulated term being equal to 0.
Since gas only goes upwards, the total gas mass balance becomes:

$$G_{j+1,top} = G_{j,top} \tag{15.2}$$

Solid material enters stage j as part of the gas flow from stage $j+1$, as well as from the bottom of stage $j-1$, and it leaves stage j through the top and bottom. The fraction of solid material leaving stage j through the bottom is defined by the cyclone separation efficiency ($x_{s,j}$). This results in a mass balance for the solid material comprised by equation 15.3 and 15.4.

$$w_{j+1,top} + w_{j-1,bot} = w_{j,bot} + w_{j,top} \tag{15.3}$$

$$w_{j,bot} = x_{s,j} \cdot (w_{j+1,top} + w_{j-1,bot}) \tag{15.4}$$

A degree of freedom analysis for the solid mass balance shows that, in a preheater tower containing N cyclone stages, $2+N$ parameters must be specified. The parameters specified here are the raw meal feed to cyclone 1, the solid material flow from the calciner cyclone to the bottom cyclone and the separation efficiency for each cyclone stage. When specifying the separation efficiency all components are assumed to behave identically.

15.3 Energy Balance

In order to calculate a temperature profile for the preheater tower, an energy balance is established for cyclone j based on equation 15.1. Again, it is assumed that the system is at steady state and that the temperature changes caused by chemical reactions are negligible. The temperature in the bottom cyclone can be influenced significantly by the exothermic reaction between CaO and CO_2. However, as a starting point this is neglected. Furthermore, it is assumed that there is no heat loss to the surroundings.
The In term in the energy balance is given by equation 15.5, while equation 15.6 describes the out term. Here, it is assumed that gas and solids leave cyclone stage j at the same temperature. In equations 15.5 and 15.6 i denotes the component considered, and H denotes the enthalpy of the component at a given temperature, which can be obtained from reference works such as Ishan Barin [164] and the National Institute of Standards and Technology [165]. Values for the species considered here are found in Appendix F.

$$In = \sum_{i=1}^{n} (w_{i,j+1,top} H_i(T_{j+1})) + \sum_{i=1}^{n} (G_{i,j+1,top} H_i(T_{j+1})) + \sum_{i=1}^{n} (w_{i,j-1,bot} H_i(T_{j-1})) \tag{15.5}$$

$$Out = \sum_{i=1}^{n} (w_{i,j,top} H_i(T_j)) + \sum_{i=1}^{n} (G_{i,j,top} H_i(T_j)) + \sum_{i=1}^{n} (w_{i,j,bot} H_i(T_j)) \tag{15.6}$$

A degree of freedom analysis for a preheater tower containing N cyclone stages shows that two temperatures must be specified in order to solve the equation system. Here, the temperature of the raw meal feed and the gas/solid flow from the calciner cyclone is specified.
Mass and energy balances where reaction changes have been left out have previously been used in connection with the modelling of preheaters (see, for instance,Hansen [2]).

15.4 Cyclone Stage Model

The model combines known gas and solid flow patterns, as described in the literature [166], with standard reactor models, by dividing a cyclone stage into distinct interconnected zones. Figure 15.3 shows a cyclone stage and its division into a riser section and a cyclone section. Each section is further subdivided into three zones, which is done in order to make it possible to account for flow patterns and reaction conditions, since each zone can be ascribed unique features. Figure 15.4 shows a schematic drawing of the zones found in a cyclone stage and how these interact. The features of the zones are explained below.

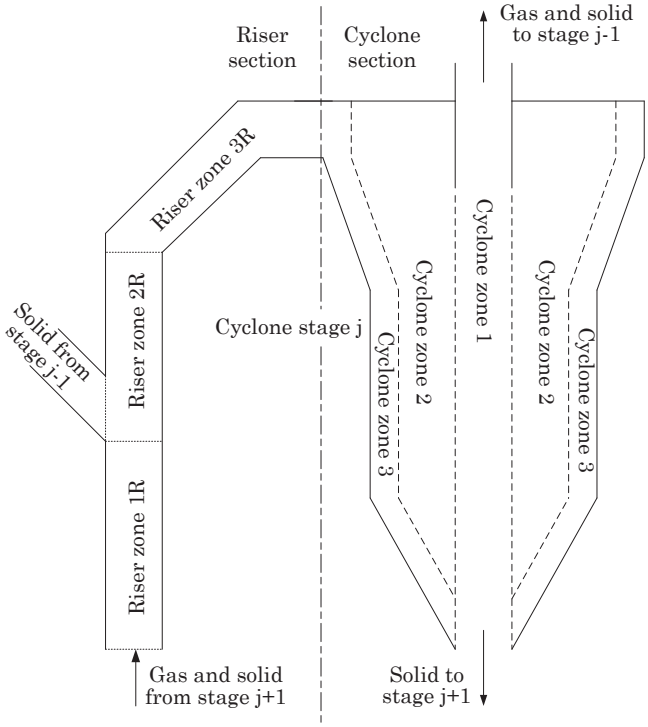

Figure 15.3: *Outline of how a cyclone stage is divided into sections and zones in order to model the cyclone stage as a reactor.*

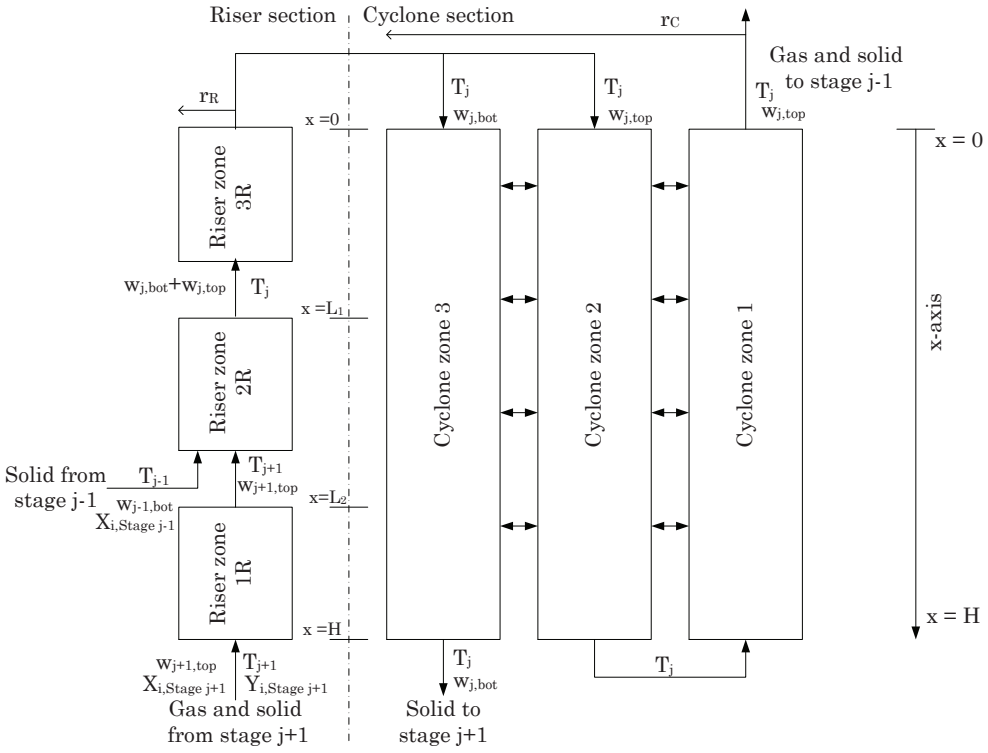

Figure 15.4: *Schematic drawing of how a cyclone stage is divided into different zones and how these zones interact.*

15.4.1 Riser Section

Riser zone 1R connects the outlet from cyclone stage $j+1$ with riser zone 2R. The temperature in this zone is equal to the temperature in cyclone $j+1$, and the solid content is equal to the solid that cyclone $j+1$ does not separate.
In riser zone 2R gas and solid from riser zone 1R are mixed with solids from cyclone stage $j-1$. In this zone heat exchange takes place and it is assumed that gas and solids leaving riser zone 2R have the same temperature and are perfectly mixed. The inlet streams to zone 2R are two separate streams, so a function which describes the physical mixing and heat exchange must be assigned.
Riser zone 3R connects zone 2R with the cyclone section, and it is assumed that this zone behaves like zone 1R, just at a lower temperature and with a larger content of solid material.
The lengths of the three riser zones need to be defined, meaning that it is possible to adjust the residence time in each zone by increasing/decreasing the length of each zone.
In the following, a gas and solid component mass balance for each zone in the riser section is established. Again, it is assumed that each cyclone is at steady state. When establishing the mass balances it is assumed that the flow pattern in each section is plug flow, without any radial concentration gradients.

Riser zone 1R and 3R
The mass balances for these two zones are identical and represented by equation 15.7 and 15.8, which describes the solid and gas mass balances, respectively.

$$V_{g,zR}\frac{dX_{i,zR}}{dx_j} = -\pi \cdot r_R^2 \cdot R_{i,s} \tag{15.7}$$

$$V_{g,zR}\frac{dY_{i,zR}}{dx_j} = -\pi \cdot r_R^2 \cdot R_{i,g} \tag{15.8}$$

Here, $V_{g,zR}$ is the total gas flow in riser zone zR, $X_{i,zR}$ is the concentration of solid component i per mass of solid in zone zR, $R_{i,s}$ is the reaction rate of solid component i, $Y_{i,zR}$ is the concentration of gas component i per mass of gas in zone zR and $R_{i,g}$ is the reaction rate of gaseous component i. Furthermore, x_j is the distance from the top of cyclone stage j.
The boundary conditions for zone $1R$ are stated in equation 15.9 and for zone $3R$ in equation 15.10.

$$Y_{i,1R} = Y_{i,Stage\ j+1} \ \ \& \ \ X_{i,1R} = X_{i,Stage\ j+1} \ \ at \ \ x_j = H \tag{15.9}$$

$$Y_{i,3R} = Y_{i,2R}|_{x=L_1} \ \ \& \ \ X_{i,3R} = X_{i,2R}|_{x=L_1} \ \ at \ \ x_j = L_1 \tag{15.10}$$

Riser zone 2R
In this zone heat exchange between hot gas and hot solid and cold solid material takes place.

In this thesis it has been decided to model this process as a three-phase system, with one phase consisting of hot gas, one of hot solid material and the last phase of cold solid material. The three phases are assumed to exchange material freely. For instance, oxygen for pyrite oxidation will be freely available in the cold phase, while SO_2 formed will instantaneously be transferred to the hot gas phase. The temperatures of the two hot phases are identical and will change from the inlet temperature to the outlet temperature over the length of riser zone 2R. The temperature change for the three phases is here modelled for the hot gas and hot solid phase, as seen in equation 15.11, and for the cold solid phase, as shown in equation 15.12. The temperatures needed for calculating the right side of equation 15.11 and 15.12 are obtained from solving the energy balance.

$$\frac{dT_{hot}}{dx_j} = \frac{T_j - T_{j+1}}{L_2 - L_1} \tag{15.11}$$

$$\frac{dT_{cold}}{dx_j} = \frac{T_j - T_{j-1}}{L_2 - L_1} \tag{15.12}$$

The boundary conditions for these two equations are stated in equation 15.13

$$T_{hot} = T_{j+1} \;\; \& \;\; T_{cold} = T_{j-1} \;\; at \;\; x_j = L_2 \tag{15.13}$$

Equation 15.14 shows the solid mass balance for the hot phase. It is noteworthy that reaction rate $R_{i,s}$ depends on the temperature of the hot phase. Equation 15.15 states the solid mass balance for the cold phase. Here, $R_{i,s}$ depends on the temperature of the cold phase. It should be noted that in equations 15.14 and 15.15 the subscripts hot and $cold$ on $X_{i,2R}$ denote the hot phase and cold phase, respectively.

$$V_{g,2R}(T_{hot})\frac{dX_{i,2R,hot}}{dx_j} = -\pi \cdot r_R^2 \cdot R_{i,s}(T_{hot}) \tag{15.14}$$

$$V_{g,2R}(T_{cold})\frac{dX_{i,2R,cold}}{dx_j} = -\pi \cdot r_R^2 \cdot R_{i,s}(T_{cold}) \tag{15.15}$$

Equation 15.16 shows the mass balance for the hot gas. Here, it is seen that the cold phase makes a contribution to the hot gas phase, which is due to the assumption that no cold gas phase exists.

$$V_{g,2R}(T_{hot})\frac{dY_{i,2R}}{dx_j} = \pi \cdot r_R^2 \left(R_{i,g}(T_{hot}) + R_{i,g}(T_{cold})\right) \tag{15.16}$$

The boundary conditions for equation 15.14-15.16 are stated in equation 15.17

$$X_{i,2Rs} = X_{i,Stage\ j-1} \;\; \& \;\; X_{i,2Rg} = X_{i,1R}|_{x_j=L_2} \;\; \& \;\; Y_{i,2R} = Y_{i,1R}|_{x_j=L_2} \;\; at \;\; x_j = L_2 \tag{15.17}$$

Appendix C outlines the In, Out and $Formed$ terms for the riser section mass balance.

15.4.2 Cyclone Section

The modelling of the cyclone section was developed by Petersen [167] in his Bachelor thesis. In his work, the basic ideas about how to consider a cyclone as a reactor were established and modelling of the pyrite oxidation in a single cyclone was conducted. Here, the same ideas are used, but the modelling will be extended to the entire preheater tower and SO_2 absorption will also be included.
When gas and solids enter the cyclone section it is assumed that they are instantaneously separated into cyclone zones 2 and 3, with zone 3 as a high solid density zone situated at the cyclone wall and zone 2 as a gas zone containing the solid material that the cyclone does not separate. The solid material in zone 2 is assumed to follow the gas flow. When the solid material in zone 3 reaches the outlet of zone 3 it becomes the solid inlet to cyclone stage $j + 1$. Zones 2 and 3 are allowed to exchange gas but not solid material. The gas exchange is described by a mass transfer coefficient and a concentration difference between the two zones. The gas/solid outlet from zone 2 will become the inlet to zone 1. The flow in zone 1 is directed upwards, as known from cyclone literature. The outlet stream from zone 1 will then become the gas/solid inlet stream to cyclone stage $j - 1$. It is possible for zones 1 and 2 to exchange gas due to concentration differences, which can be described as for zones 2 and 3. Furthermore, it is possible for zones 1 and 2 to exchange both gas and solids through a convective radial flow from zone 1 to zone 2, which can transport matter from low to high concentration and is introduced in order to account for phenomena such as lip leakages and other radial flow phenomena.
The division of the cyclone section into three zones makes it possible to account for the primary flow characteristics of cyclones such as longer solid residence time than gas residence time, the separation of gas and solids and the U-turn of gas flow at the bottom of the cyclone.
The assumptions for the cyclone model are that the cyclone section is isothermal, separation takes place instantaneously, in each zone there are no concentration gradients in radial direction, the amounts of solid and gas do not change due to reactions and gas and solid flow are modelled as a plug flow in each zone. The fast, spinning motion spiralling upwards or downwards in a plug flow is explained by a slower vertical plug flow with the same residence time. In the following, a gas and solid component mass balances for each zone in the cyclone section is established, with the accumulating term equal to 0. The mass balances are shown below, with the specific In, Out and $Formed$ terms found in Appendix C.

Cyclone zone 1
The solid and gaseous mass balances for component i in zone 1 are seen in equation 15.18 and 15.19

$$X_{i,1}\frac{dV_{g,1}}{dx} + V_{g,1}\frac{dX_{i,1}}{dx_j} = 2 \cdot \pi \cdot r_1 \cdot U_r \cdot X_{i,2} - \pi \cdot r_1^2 \cdot R_{i,s} \tag{15.18}$$

$$Y_{i,1}\frac{dV_{g,1}}{dx} + V_{g,1}\frac{dY_{i,1}}{dx_j} = 2\cdot\pi\cdot r_1\left(U_r\cdot Y_{i,2} + K_{1\to 2}\left(Y_{i,1}-Y_{i,2}\right)\right) - \pi\cdot r_1^2\cdot R_{i,g} \tag{15.19}$$

Here, U_r is the radial gas flow from zone 1 to 2 and $K_{1\to 2}$ is the mass transfer coefficient from zone 1 to 2. It is here noted that the gas flow ($V_{g,1}$) in zone 1 depends upon x, which is due to the radial flow from zone 1 to zone 2. In order to handle this flow, a total gas mass balance for zone 1 is established, as seen in equation 15.20

$$\frac{dV_{g,1}}{dx_j} = 2\cdot\pi\cdot r_1\cdot U_r \tag{15.20}$$

The boundary conditions for zone 1 are stated in equation 15.21, where $V_{g,0}$ is defined as the volume flow of gas in the entrance to the cyclone section.

$$X_{i,1} = X_{i,2}\ \ at\ \ x_j = H \quad \& \quad Y_{i,1} = Y_{i,2}\ \ at\ \ x_j = H \quad \& \quad V_{g,1} = V_{g,0}\ \ at\ \ x_j = 0 \tag{15.21}$$

Cyclone zone 2

Equations 15.22 and 15.23 represent the solid and gas mass balances for component i in zone 2, respectively. Equation 15.24 describes the total gas mass balance in zone 2, which is needed due to the radial flow from zone 1 to zone 2. In equation 15.23, $K_{2\to 3}$ denotes the mass transfer coefficient for gas transfer from zone 2 to zone 3.

$$X_{i,2}\frac{dV_{g,2}}{dx_j} + V_{g,2}\frac{dX_{i,2}}{dx_j} = 2\cdot\pi\cdot r_1\cdot U_r\cdot X_{i,2} + \pi\cdot\left(r_2^2 - r_1^2\right)\cdot R_{i,s} \tag{15.22}$$

$$\begin{aligned} Y_{i,2}\frac{dV_{g,2}}{dx_j} + V_{g,2}\frac{dY_{i,2}}{dx_j} &= 2\cdot\pi\cdot r_1\left(U_r\cdot Y_{i,2} + K_{1\to 2}\left(Y_{i,1}-Y_{i,2}\right)\right) \\ &\quad - 2\cdot\pi\cdot r_2\cdot K_{2\to 3}\left(Y_{i,2}-Y_{i,3}\right) + \pi\cdot\left(r_2^2 - r_1^2\right)\cdot R_{i,g} \end{aligned} \tag{15.23}$$

$$\frac{dV_{g,2}}{dx_j} = 2\cdot\pi\cdot r_1\cdot U_r \tag{15.24}$$

The boundary conditions for zone 2 are stated in equation 15.25

$$X_{i,2} = X_{i,3R}|_{x_j=0}\ \ at\ \ x_j = 0 \quad \& \quad Y_{i,2} = Y_{i,3R}|_{x_j=0}\ \ at\ \ x_j = 0 \quad \& \quad V_{g,2} = V_{g,0}\ \ at\ \ x_j = 0 \tag{15.25}$$

Cyclone zone 3

Where the mass balances in cyclone zone 1 and 2 were based on the gas flow, the mass balances for zone 3 are based on the flow of solid material, as seen in equations 15.26 and 15.27, which describe the solid and gaseous mass balances for component i in zone 3, respectively.

$$V_{s,3}\frac{dX_{i,3}}{dx_j} = \frac{1}{1+\epsilon}\cdot\pi\cdot\left(r_3^2 - r_2^2\right)\cdot R_{i,s} \tag{15.26}$$

$$V_{s,3}\frac{dY_{i,3}}{dx_j} = 2 \cdot \frac{1}{1+\epsilon} \cdot \pi \cdot K_{2\to3} \cdot r_2 \cdot (Y_{i,2} - Y_{i,3}) + \frac{1}{1+\epsilon} \cdot \pi \cdot \left(r_3^2 - r_2^2\right) \cdot R_{i,g} \tag{15.27}$$

Here, ϵ denotes the gas/solid volume ratio in zone 3. The solid flow in zone 3 does not depend on x because solid material is not exchanged with zone 2. The boundary conditions for zone 3 are stated in equation 15.28.

$$X_{i,3} = X_{i,3R}|_{x=0} \;\; at \;\; x_j = 0 \quad \& \quad Y_{i,3} = Y_{i,3R}|_{x_j=0} \;\; at \;\; x_j = 0 \tag{15.28}$$

15.4.3 Dimensionless Variables

The equation system is made dimensionless by introducing the dimensionless variables defined as:

$$z_j = \frac{x_j}{H} \tag{15.29}$$

$$W_{g,z} = \frac{V_{g,z}}{V_{g,0}} \tag{15.30}$$

$$X^*_{i,z} = \frac{X_{i,z}}{X_{i,0}} \tag{15.31}$$

$$Y^*_{i,z} = \frac{Y_{i,z}}{Y_{i,0}} \tag{15.32}$$

$$U^*_r = \frac{U_r}{U_{r,0}} \tag{15.33}$$

Here H is the height of the cyclone stage, $X_{i,0}$ is the maximum amount of solid species i, defined based on the relevant reaction equation. For instance, $X_{CaSO_3,0}$ will be equal to the mass of $CaCO_3$ times the $CaSO_3/CaCO_3$ molar ratio, according to reaction equation 15.34.

$$CaCO_3(s) + SO_2(g) \to CaSO_3(s) + CO_2(g) \tag{15.34}$$

This way of defining $X_{i,0}$ makes the dimensionless parameter ($X^*_{i,z}$) equal to the conversion, on mass basis, of the solid reactant, in this case $CaCO_3$.
If $Y_{i,0}$ is defined as the maximum concentration possible in the exhaust gas from the top cyclone, $Y_{SO_2,0}$ will be equal to the total sulphur input times the molar ratio of SO_2/S. When defining $Y_{i,0}$ in this way, $Y^*_{i,z}$ becomes a measure for the fraction of the substance that is emitted with the exhaust gas.
If $U_{r,0}$ is defined as the highest radial flow velocity, U^*_r will be between 0 and 1. Furthermore, $V_{g,0}$ is defined as the volume flow of gas in the inlet to a cyclone section, where the temperature is equal to the cyclone temperature. The entire dimensionless equation system is seen in Appendix D, along with the dimensionless boundary conditions.

15.5 Reaction Kinetics

The reactions considered in this thesis are pyrite oxidation, SO_2 formation and SO_2 absorption on $CaCO_3$. However, SO_2 absorption on CaO will not be considered because it does not, to any significant extent, contribute to the SO_2 absorption, as concluded earlier.

15.5.1 Pyrite Oxidation

As suggested by Hansen [2], the pyrite oxidation is divided into two reactions, namely the oxidation of pyrite to troilite (15.35) and the further oxidation of troilite to hematite (15.36).

$$FeS_2(s) + O_2(g) \rightarrow FeS(s) + SO_2(g) \tag{15.35}$$

$$2FeS(s) + 3O_2(g) \rightarrow Fe_2O_3(s) + 2SO_2(g) \tag{15.36}$$

Hansen [2] found from his experiments with pure pyrite crystals and shale containing pyrite inclusions that both reactions were first order with respect to the concentration of solid reactant. When investigating the effect of oxygen, Hansen [2] ascertained that the reactions were zero order with respect to oxygen when the concentration was between 2 and 5 %. Oxygen concentrations of this size correspond to the concentrations found in preheater towers, which is why reactions 15.35 and 15.36 are assumed to be independent of the oxygen concentration. Equations 15.37 and 15.38 show the rate expressions for FeS_2 and FeS oxidation, respectively.

$$R_{FeS_2,s} = K_{FeS_2}(T) \cdot X_{FeS_2,z} \qquad \left[\frac{kg\ FeS_2}{s \cdot kg\ solid}\right] \tag{15.37}$$

$$R_{FeS,s} = K_{FeS}(T) \cdot X_{FeS,z} \qquad \left[\frac{kg\ FeS}{s \cdot kg\ solid}\right] \tag{15.38}$$

The temperature dependency of the rate constants (K_{FeS_2} & K_{FeS}) was found by Hansen [2] to follow expression 15.39, with a reference temperature ($T_{i,0}$) of 400 °C.

$$ln\left(\frac{K_i}{K_{i,0}}\right) = \frac{E_{a,i}}{R_{gas}}\left(\frac{1}{T_{ref}} - \frac{1}{T}\right) \tag{15.39}$$

The reference rate constant ($K_{i,0}$) and activation energy ($E_{a,i}$) are given by Hansen [2] for the oxidation of pure pyrite crystals and pyrite inclusions in shale. In raw meal, pyrite is commonly found as inclusions in shale. Hence, the kinetic is based on these data (see Table 15.1).

15.5.2 SO_2 Formation

In this modelling approach SO_2 originates exclusively from the oxidation of FeS_2 and FeS. From equations 15.35 and 15.36 it is noticeable that the reaction stoichiometry, in both cases, is 1:1.

Component	$E_{a,i}$	$K_{i,0}\|_{400\ ^\circ C}$
	kJ/mol	1/S
FeS_2	117	$3.36{\cdot}10^{-2}$
FeS	205	$3.34{\cdot}10^{-4}$

Table 15.1: *Activation energy and reference rate constant for the oxidation of pyrite inclusions in shale, Hansen [2].*

This leads to a formation rate of SO_2 that can be calculated from equation 15.40.

$$R_{SO_2,g} = y_{solid,z} \cdot \left(\frac{M_{SO_2}}{M_{FeS_2}} \cdot R_{FeS_2,s} + \frac{M_{SO_2}}{M_{FeS}} \cdot R_{FeS,s} \right) \quad \left[\frac{kg\ SO_2}{s \cdot kg\ gas} \right] \tag{15.40}$$

15.5.3 SO_2 Absorption

SO_2 absorption is assumed to take place according to equation 15.41.

$$CaCO_3(s) + SO_2(g) \rightarrow CaSO_3(s) + CO_2(g) \tag{15.41}$$

Numerous studies (see Chapter 5) have been carried out concerning this reaction. Here, data from Hu [3] will be used, since it was obtained with the absorption of SO_2 in preheater towers in mind. However, the reaction mechanism proposed by Hu [3] will be discarded due to the reasons outlined below.

If the data from Hu [3] is subjected to an analysis for internal and external mass transfer limitations, as outlined in Appendix 11, it is possible to construct Figure 15.5, which shows the particle diameter at which the Weisz-Prater modulus and Mears criterion are equal to 0.15, meaning the largest particle diameter where mass transfer limitations are negligible. When calculating the Weisz-Prater modulus, a particle porosity of 8 % has been used instead of the porosity of 30 % stated by Hu [3], because a number of repeated Hg-porosimetry measurements have shown that a porosity of 8 % is correct, when inter-particuler void is sorted out.

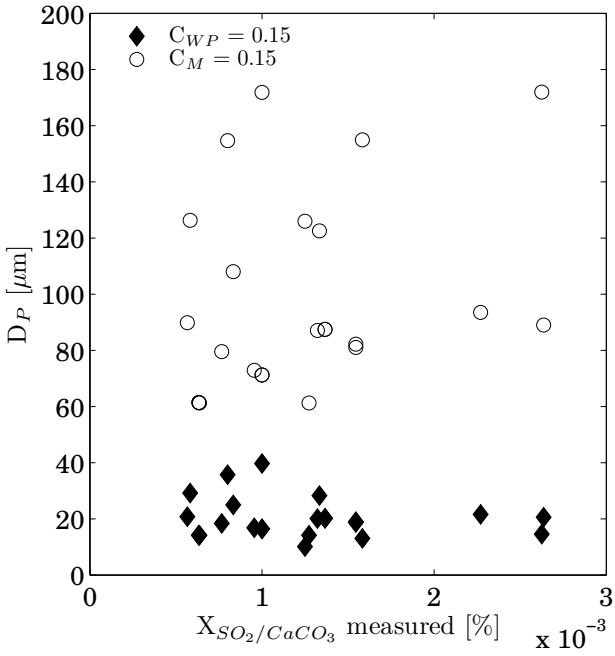

Figure 15.5: *Particle diameter at which C_{WP} and C_M are equal to 0.15 as a function of the measured values for $CaCO_3$ conversion in Hu's experiments [3].*

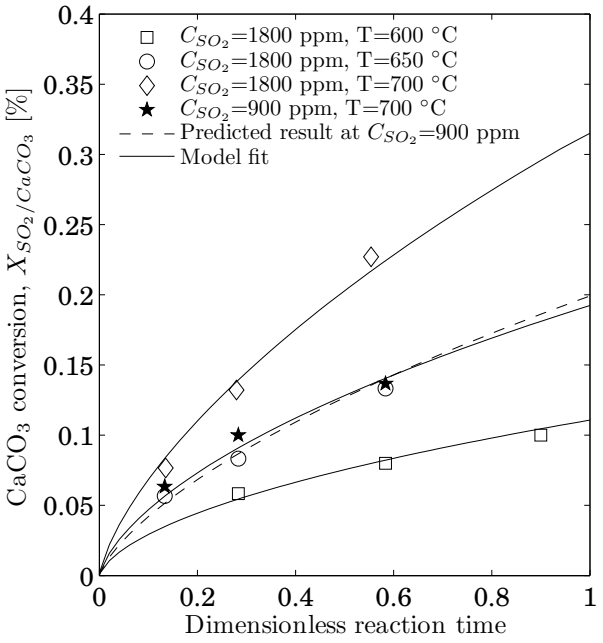

Figure 15.6: *Comparison between the model and experimental results for Hu's [3] data. The dotted line indicates the predicted conversion at 900 ppm SO_2.*

When comparing the diameters in figure 15.5 to Hu's [3] particle distribution, it is evident that internal diffusion limitations can be ruled out only for about 5 w/w % of the particles used, and external diffusion limitations cannot in any case be completely ruled out. In order to deal with the diffusion limitations in Hu's experiments [3] his data is fitted to the model outlined in Chapter 14 and used for modelling the CaO results.

Fitting Hu's [3] data is based on three data series obtained between 600 and 700 °C in an atmosphere containing 3 % O_2, 15 % CO_2, 1800 ppm SO_2 and a balance N_2. The oxygen concentration used by Hu [3] corresponds well with the concentration found in preheater towers, whereas the CO_2 concentration is only about half of that found in preheater towers. From the experiments with CaO, it is known that, above a 10 % CO_2 level, an increase in the CO_2 concentration has a very limited influence upon the CaO conversion. Therefore, it is assumed that above 15 % CO_2 the $SO_2/CaCO_3$ reaction is zero order with respect to CO_2. The reaction order with respect to SO_2 is assumed to be 1.

When estimating the reaction parameters for the CaO data it was found that the minimum sum of square became constant when the reaction constant became larger than 1 m/s. The same behaviour has been observed for Hu's [3] data for the $CaCO_3/SO_2$ reaction. For this reason, the reaction constant (here denoted as $K_{SO_2/CaCO_3}$) is, as was also the case for the CaO/SO_2 reaction, put equal to 10 m/s and assumed independent of temperature. Thus, the parameters that are to be estimated from the experimental data are D_0 and ψ, with the reference temperature for ψ taken to be 500 °C.

Figure 15.6 shows the three data series used for estimating the parameters along with the calculated $CaCO_3$ conversion. The calculated data show that the model describes the experimental data very satisfactorily and that the model can predict $CaCO_3$ conversion when using a SO_2 concentration of 900 ppm. Equation 15.42 shows the expression for D_{s,SO_2}.

$$D_{s,SO_2} = 3.75 \cdot 10^{-2} \cdot exp\left(\frac{-186.4kJ/mol}{R_{gas} \cdot T}\right) \quad [m^2/s] \tag{15.42}$$

When simulating the SO_2 absorption, it is assumed that there are no diffusion limitations. This assumption is justified because normally more than 50 w/w % of the particles are smaller than 10 μm and SO_2 formation takes place at temperatures lower than those used in the experiments by Hu [3]. Based on these assumptions the rate at which $CaCO_3$ grains shrink can be expressed by equation 15.43.

$$\frac{dr}{dt} = \frac{C_{SO_2,bulk}}{\rho_{CaCO_3}} \cdot \frac{1}{\frac{1}{K_{SO_2/CaCO_3}} + \frac{r_g}{D_{s,SO_2}} \cdot \frac{r}{r_g} \cdot \left(1 - \frac{r}{r_g}\right)} \tag{15.43}$$

The conversion of a spherical $CaCO_3$ grain to $CaSO_3$ (equation 15.44) is substituted into equation 15.43, resulting in equation 15.45.

$$X_{SO_2/CaCO_3} = 1 - \frac{r^3}{r_g^3} \quad \left[\frac{mole\ \ CaSO_3}{mole\ \ CaCO_3}\right] \tag{15.44}$$

$$\begin{aligned} \frac{dX_{SO_2/CaCO_3}}{dt} \quad = \quad & \frac{C_{bulk,SO_2}}{\rho_{CaCO_3}} \cdot \frac{\left(1 - X_{SO_2/CaCO_3}\right)^{2/3}}{\frac{r_g}{K_{SO_2/CaCO_3}} + \frac{r_g^2}{D_{s,SO_2}}} \cdot \\ & \frac{1}{\left(1 - X_{SO_2/CaCO_3}\right)^{1/3} \cdot \left(1 - \left(1 - X_{SO_2/CaCO_3}\right)^{1/3}\right)} \end{aligned} \tag{15.45}$$

Equation 15.45 is simplified by approximating the denominator and the numerator by a Taylor series (equation 15.46 and 15.47). Only the first order term is used, since $X_{SO_2/CaCO_3}$ will always be small due to the large excess of $CaCO_3$.

$$\left(1 - X_{SO_2/CaSO_3}\right)^{2/3} \approx 1 - \frac{2}{3} \cdot X_{SO_2/CaSO_3} \tag{15.46}$$

$$\left(1 - X_{SO_2/CaSO_3}\right)^{1/3} \cdot \left(1 - \left(1 - X_{SO_2/CaSO_3}\right)^{1/3}\right) \approx \frac{1}{3} \cdot X_{SO_2/CaSO_3} \tag{15.47}$$

By substituting the Taylor series into equation 15.45 and rewriting to the right units, the rate at which $CaSO_3$ is formed can be expressed by equation 15.48.

$$\begin{aligned} R_{CaSO_3,s} \quad = \quad & \frac{M_{CaSO_3} \cdot Y^*_{SO_2,z} \cdot Y_{SO_2,0} \cdot \rho_{gas}}{M_{SO_2} \cdot \rho_{CaCO_3}} \cdot \\ & \frac{1 - \frac{2 \cdot M_{CaCO_3}}{3 \cdot M_{CaSO_3} \cdot Q_{CaCO_3}} \cdot X_{CaSO_3,z}}{\frac{r_g}{K_{SO_2/CaCO_3}} + \frac{r_g^2}{D_{s,SO_2}} \cdot \frac{M_{CaCO_3}}{3 \cdot M_{CaSO_3} \cdot Q_{CaCO_3}} \cdot X_{CaSO_3,z}} \quad \frac{kg\ \ CaSO_3}{s\ \cdot\ kg\ \ solid} \end{aligned} \tag{15.48}$$

The absorption rate of SO_2 can now be expressed by equation 15.49.

$$R_{SO_2,g}(absorption) = -y_{solid,z} \cdot \frac{M_{SO_2}}{M_{CaSO_3}} \cdot R_{CaSO_3,s} \quad \left[\frac{kg\ \ SO_2}{s\ \cdot\ kg\ \ gas}\right] \tag{15.49}$$

15.6 Input Parameters

Table 15.2 summarises the 29 parameters required for solving the preheater tower model.

	Parameter	Symbol	Calculated by	Unit
1	Raw meal feed of component i	$w_{i,0,bot}$	Specified	kg/s
2	Mole fraction of component i in the gas phase	x_i	Specified	
3	Mass fraction of component i from stage $N+1$	$Q_{i,N+1}$	Specified	
4	Cyclone separation efficiency for stage j	$x_{s,j}$	Specified	
5	Diameter of cyclone	D	Specified	m
6	Pressure in cyclone j	P_j	Specified	Pa
7	Gas from calciner to stage N	$G_{N+1,top}$	Specified	kg/s
8	Inlet temperature of raw meal	T_0	Specified	K
9	Inlet temperature of gas/solid from stage $N+1$	T_{N+1}	Specified	K
10	Residence time of solid material in cyclone zone 3	t_3	Specified	s
11	Bulk density of solid material	ρ_{solid}	Specified	kg/m^3
12	Surface Area of CaCO3 in raw meal	$A_{BET,CaCO_3}$	Specified	m2/kg
13	Fraction of riser duct length used for heat exchange	hel	Specified	
14	Volume of gas per volume of solid in cyclone zone 3	ϵ	Specified	
15	Flow from cyclone zone 1 to 2	U_r	Specified	m/s
16	Mass transfer coefficient from cyclone zone 1 to 2	$K_{1\to2}$	Specified	m/s
17	Mass transfer coefficient from cyclone zone 2 to 3	$K_{2\to3}$	Specified	m/s
18	Length of riser zone 3R	L_1	$H - L_2 - hel \cdot H$	m
19	Density of gas	ρ_{gas}	$\frac{M_{gas} \cdot P}{R \cdot T}$	kg/m^3
20	Volume flow of gas in section z	$V_{g,z}$	$\frac{G_{j,top} \cdot R \cdot T}{M_{gas} \cdot P}$	m^3/s
21	Radius of cyclone zone 2	r_2	$\frac{D}{2} - \frac{w_{j,bot} \cdot t_3 \cdot (1+\epsilon)}{\rho_{solid} \cdot A_{wall}}$	m
22	Radius of cyclone zone 3	r_3	$\frac{D}{2}$	m
23	Molar mass of gas phase	M_{gas}	$\sum_{n=1}^{i} x_{i,gas} \cdot M_i$	kg/mol
24	Solid from calciner to stage N	$w_{N+1,top}$	$w_{N,bot} \cdot x_{s,N+1}$	kg/s
25	Hight of cyclone	H	Confidential	m
26	Radius of cyclone zone 1	r_1	Confidential	m
27	Area of cyclone wall	A_{wall}	Confidential	m^2
28	Radius of riser duct	r_R	Confidential	m
29	Length of riser zone 2R and 3R	L_2	Confidential	m

Table 15.2: *Overview of parameters required for solving prheater tower model. Confidential means that the parameters are calculated using unpublished models provided by FLSmidth.*

The first six parameters are all plant-specific, and they must be specified as vectors which should either contain a value for each component considered or a value for each cyclone stage in the preheater tower. It is important to note at this juncture that $x_{s,j}$ contains $N+1$ values, because

it must be stated how much of the material entering the calciner cyclone recirculates to stage N. Parameters 7-13 are also plant-specific but are scalar values.
Parameter 14 can be interpreted as an aeration factor of cyclone zone 3. Levenspiel [133] posits such aeration factors for different reactor types. Table 15.3 summarises the original values from Levenspiel, along with the corresponding ϵ values.

	Value Levenspiel [133]	Value of ϵ
unit	m^3 solid / m^3 vessel	m^3 gas/ m^3 solid
Pneumatic conveying	0.01-0.06	16-99
Fast fluidisation	0.06-0.2	4-16
Turbulent fluidisation	0.2-0.4	2-4
Bubbling fluidised bed	0.4-0.6	1-2

Table 15.3: *Values of ϵ for different reactor types.*

Parameters 15-17 are mass transfer coefficients estimated by fitting the model to experimental data. Parameters 18-24 are calculated from the stated equations for relevant conditions, which are determined by the cyclone stage and zone considered. Parameters 25-29 are calculated from unpublished design equations used by FLSmidth for designing preheater cyclones, which is why they can not be stated here.

Chapter 16

Evaluation of the Preheater Tower Model

Based on measurements performed by FLSmidth it has been possible to obtain data for five different plants, here denoted as plants A-E. In plant A N is equal to 5, while N is 4 for plant B and 3 for plant C, D and E. Plant-specific data for the five plants is stated in Appendix E. In this chapter simulation results and the influence of specific parameters will be presented and evaluated.

16.1 Total Mass and Energy Balance

A solution of the total mass and energy balances is produced by the $fsolve$ function in Matlab. In order to do this, parameters 1-4 and 7-9 act as input parameters. The separation efficiency of the cyclones can be especially difficult to determine, and may therefore be reported with some uncertainty. Carbonisation in cyclone N, caused by the recirculation of material from the calciner cyclone, is here accounted for in the energy balance by allowing more material to recirculate from the calciner cyclone. A higher recirculation will increase the temperature in cyclone N. This way of accounting for carbonisation in cyclone N will result in too high a mass content in cyclone N, but it is considered more important that the temperature profile is right than the mass content in cyclone N.
Figure 16.1 shows the cyclone temperature predicted by the preheater tower model as a function of the measured temperature for plants A-E. It is evident that there is good agreement between the measured and predicted temperatures, which is crucial for the calculations for SO_2 emission, due to the temperature dependency of the reaction kinetics.

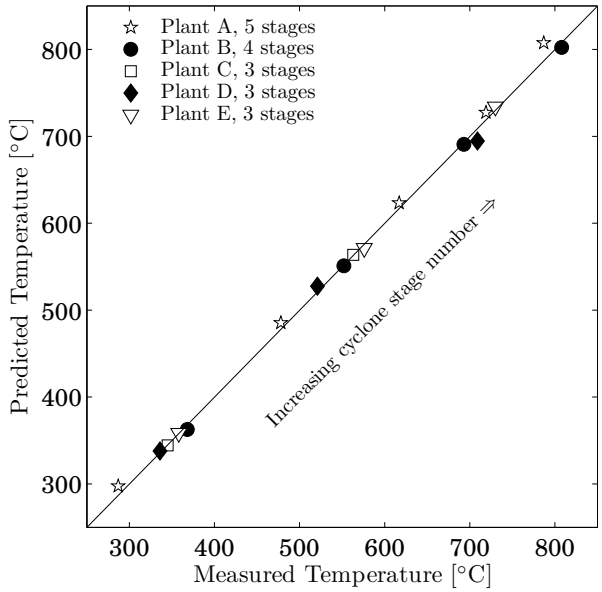

Figure 16.1: *Temperatures predicted by the preheater tower model as a function of the measured temperature for plants A-E.*

16.2 Cyclone Stage Model

The cyclone stage model used for evaluating the reactions in each cyclone stage includes three reactions, as outlined in section 15.5. The kinetics of these reactions depend on the concentrations of the four species FeS_2(s), FeS(s), SO_2(g) and $CaSO_3$(s), which have been included in the cyclone stage model. Setting up the differential equations for each species results in riser zones 1 and 3 both containing three differential equations for solid material and one equation for SO_2 in the gas phase. Riser zone 2 is described by three differential equations for solid material in the hot phase and three equations for material in the cold phase. One equation is used for describing SO_2 in the hot gas phase and two for describing the temperature profile in the hot and cold phase. In total, nine differential equations are used for describing riser zone 2. Each zone in the cyclone section is described by four differential equations, three for solid material and one for gaseous material. Furthermore, one equation for the total gas mass balance for zone 1 is needed. The differential equation systems are solved by the ordinary differential equation solver *ode15s* in Matlab, which is well suited for solving stiff problems like the cyclone stage model appeared to be.

The interconnection of the cyclone stages couples cyclone stage j to the other stages, and is handled by an iteration procedure where all N cyclone stages are solved. Next, new inlet concentrations are calculated from the solution and applied when solving the cyclone stage model again. The iteration procedure continues until new and old inlet concentrations are equal.

The outlet pressure from cyclone 1 is close to atmospheric pressure, and the cyclones are designed to minimise pressure loss. To simplify calculations a constant pressure equal to 1 atm is

specified, while the aeration factor (ϵ) for cyclone zone 3 is put equal to 4 m^3 gas/m^3 solid. According to Table 15.3 this corresponds to a fast/turbulent fluidisation reactor. The value of the 4 m^3 gas/m^3 solid is chosen as a starting point because it is believed that zone 3 has a relatively high particle density. Based on the measurements made by Strauss et al. [12] the solid residence time in cyclone zone 3 is 8 s. It was decided that 20% of the riser duct length would be utilised for heat exchanging hot gas/solid and cold solid material. This results in hel being 0.2.

In the model, three parameters ($K_{1\to2}$, $K_{2\to3}$ and U_r) are to be estimated from experimental data. Of these, $K_{2\to3}$ is considered by far the most important parameter, since it ensures that gas is exchanged between cyclone zones 2 and 3. Both U_r and $K_{1\to2}$ are considered less important, because solid material and gas in zone 2 will enter zone 1 at the bottom of the cyclone, so in this manner zone 1 and 2 exchange material in any case. In order to minimise the number of parameters to be estimated, both $K_{1\to2}$ and U_r are put equal to zero. Thus, the only parameter to be estimated will be $K_{2\to3}$, which will be assumed independent of the cyclone considered.

Figure 16.2 shows the predicted sulphide content in the raw meal out of different cyclones as a function of the measured sulphide content in the raw meal. The figure clearly shows a satisfactory agreement between predicted and measured sulphide content.

At low pyrite concentrations, the model predicts a sulfide content which is too low. Most of the deviation between model and measured results at low sulphide contents is caused by measuring errors. This is, for instance, observed for plant B, where the measured sulphide content appears to be constant about 0.02 w/w%, although the temperature increases from about 550 °C to 700 °C, meaning that all pyrite should have been oxidised.

When using the preheater tower model all sulphide was assumed to be found as FeS_2, meaning that 50 w/w% was oxidised according to the FeS_2 reaction rate, while the other 50% was oxidised according to the FeS reaction rate. However, if FeS content comprises more than 50 w/w % of the sulphide (meaning that FeS_2 will constitute less than 50 w/w %), the model will predict a lower sulphide content in the raw meal than measured. This is due to the slower oxidation kinetics of FeS than those for FeS_2, which is why the FeS_2/FeS ratio is crucial for where the formation of SO_2 will take place.

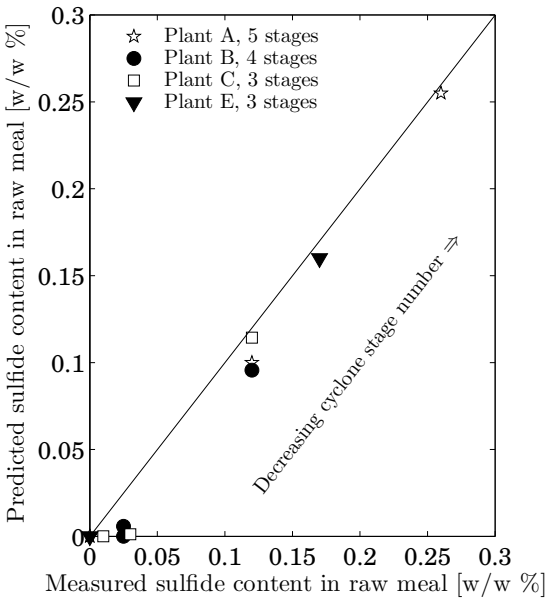

Figure 16.2: *Sulphide content in raw meal predicted by the preheater tower model as a function of the measured sulphide content in the outlet from different cyclone stages. No data for plant D is available.*

Figure 16.3 shows the mass fraction of raw meal sulphide emitted as SO_2 from the preheater tower for the five plants as a function of the mass transfer coefficient between cyclone zones 2 and 3. The measured emissions for the five plants are summarised in Table 16.1. A comparison of the data in Table 16.1 with the predicted emissions in the figure shows that the predicted emission for plant A is similar to the one measured for $K_{2\to3}$ values between 0.05 m/s and 0.5 m/s. The measured emission from plant C is a little higher than the predicted one at small values of $K_{2\to3}$. The measured emission is extremely low for plant B (this could indicate a very reactive limestone), with the model predicting considerably higher emissions than those observed. The predicted emissions for plants D and E are about 50 % of that measured, with the predicted value for plant E lower than for D. This is the same trend as seen in the measurements.
In general, the effect of changing $K_{2\to3}$ seems to be limited, as long as $K_{2\to3}$ is below 0.1 m/s. At higher values the predicted emissions tend to approach an asymptote where the effect of increasing $K_{2\to3}$ further is strongly limited. At higher values of $K_{2\to3}$ cyclone zones 2 and 3 can exchange mass almost freely, so that the emission tends to be exclusively limited by the $SO_2/CaCO_3$ reaction. At low values of $K_{2\to3}$, the sulphide emitted as SO_2 also approaches an asymptote. Here, it is caused by an absence of SO_2 exchange between the two zones.

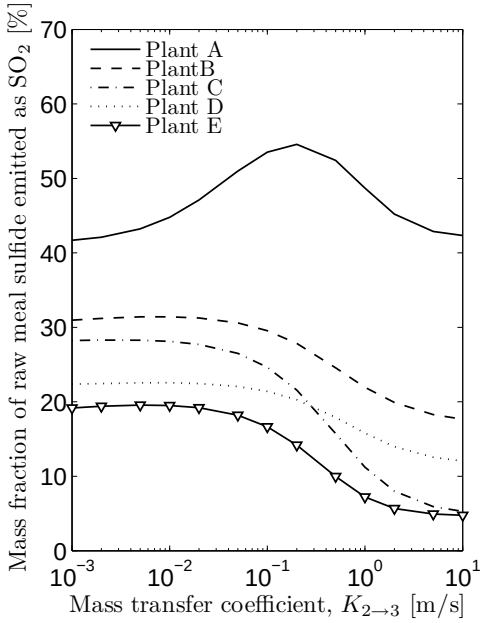

Figure 16.3: *Predicted fraction of raw meal sulphide that will leave the preheater tower as SO_2, as a function of the mass transfer coefficient between cyclone zones 2 and 3.*

Plant	Raw meal sulphide emitted
	w/w %
A	53
B	8
C	33
D	40
E	36

Table 16.1: *Measured fraction of raw meal sulphide emitted from the preheater tower for the five plants.*

The three parameters ϵ, hel and t_3 are based on non-plant specific data. Their influences are investigated at a maintained value for $K_{2\to3}$ of 0.05 m/s. One parameter is changed at a time, with the value of the two others set to the value used when determining $K_{2\to3}$.

Figure 16.4 shows the predicted emission of sulphide as a function of the aeration factor for cyclone zone 3 (ϵ). It is evident that even large changes in ϵ have no effect upon the predicted amount of raw meal sulphide emitted as SO_2, because only a small amount of SO_2 is exchanged between zones 2 and 3 (relatively small $K_{2\to3}$ value). Any SO_2 released in zone 2 is to be absorbed therein and it is not influenced by the aeration factor. In relation to a full-scale cement plant this result implies that any absorbent for the in-situ removal of SO_2 has to be added directly to the phase where it is required to reduce SO_2.

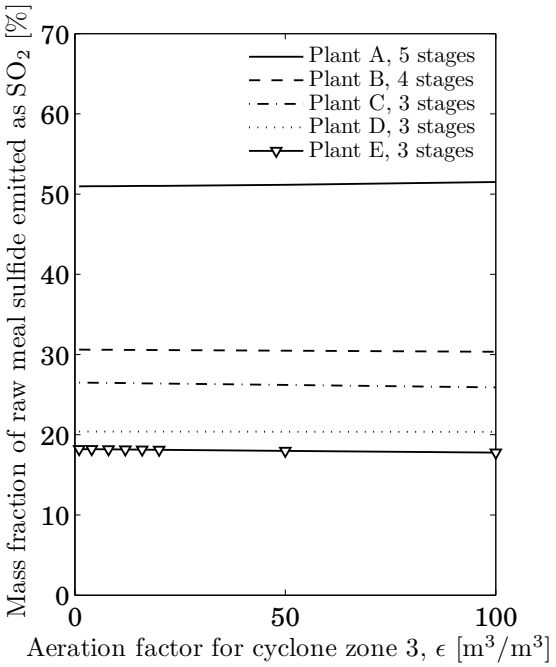

Figure 16.4: *Predicted fraction of raw meal sulphide that will leave the preheater tower as SO_2, as a function of the aeration factor. ϵ was 4 m^3 gas/m^3 solid when determining $K_{2\to3}$.*

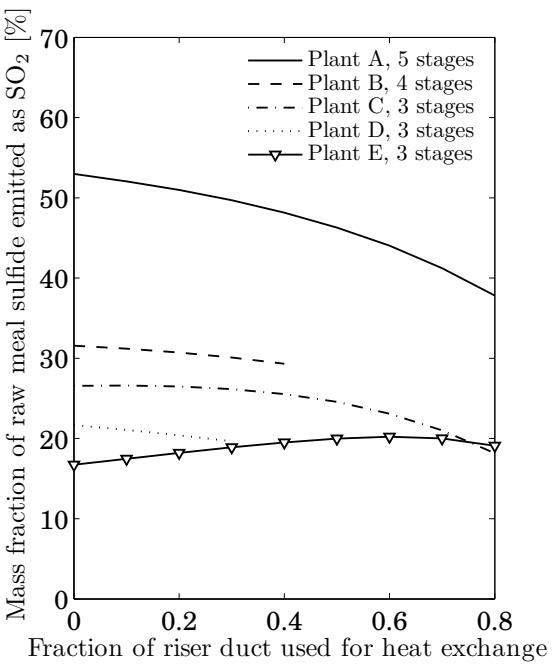

Figure 16.5: *Predicted fraction of raw meal sulphide that will leave the preheater tower as SO_2, as a function of the fraction of riser duct used for heat exchange. hel was 0.2 when determining $K_{2\to3}$.*

Figure 16.5 shows the effect of changing the fraction of the riser duct used for heat exchange (hel). A large hel value means that heat exchange will take place over a longer period. It is observed that, except for plant A, the effect of changing hel is limited, with different trends for different plants. Plant A's effect relates to the fact that this plant contains five cyclones. The large number of cyclones causes SO_2 to be released at lower temperatures, where the SO_2 absorption is less effective. A longer time for heat exchange will reduce SO_2 release in the riser duct, because the cold material contains the main fraction of sulphide. Some of the SO_2 not released in the riser duct will instead be formed in cyclone zone 3 where the absorption is most efficient due to the high content of $CaCO_3$. Hence, less raw meal sulphide will be emitted as SO_2. Contrary to the other four plants, plant E does not follow this trend; instead, a small increase in emission is observed up to a hel value around 0.7. This increase occurs because plant E has the highest temperature in cyclone stage 2, where most of the pyrite oxidation is known to take place. The relatively high temperature in cyclone stage 2 means that the absorption is faster than pyrite oxidation, which is why a longer heat transfer time in this case means that the material has a shorter residence time in riser zone 3, where the absorption is very efficient.

Figure 16.6 shows the raw meal sulphide emitted as SO_2 as a function of the solid material residence time in cyclone zone 3. Two different tendencies are seen. Plants A and D have a contentious decrease in emissions as the residence time in cyclone zone 3 increases. Plants B, C

and E, on the other hand, appear to have a minimum emission between 3 and 6 s. In general, the effect of changing the residence in cyclone zone 3 is much weaker for plants B,C and E than observed for plants A and D. These results are related closely to cyclone temperatures. Figure 16.1 highlights that plants A and D have the lowest temperatures in cyclone stages 1 and 2, meaning that SO_2 absorption on $CaCO_3$ is slow compared to plants B, C and E. When the reaction rate is lower, these plants will benefit from a longer reaction time in zone 3, which is why a continuous decrease in emission is observed when the residence time in cyclone zone 3 is increased. In plants B, C and E the temperature is higher in the top cyclone, meaning that more SO_2 is formed in the first cyclone stage. However, the temperature is still too low for the absorption to be efficient, resulting in a weak increase in emission at long residence times, since more SO_2 can be formed in the first cyclone stage. The increase observed at short times is caused because the raw meal does not have enough time to absorb the formed SO_2 in cyclone stage 2.

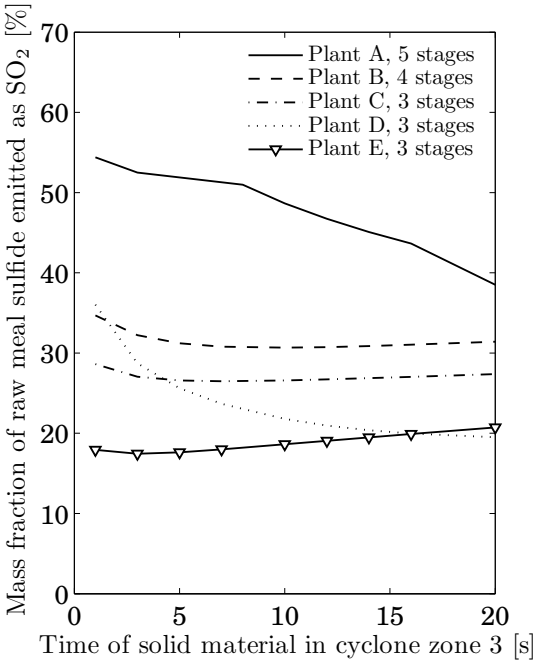

Figure 16.6: *Predicted fraction of raw meal sulphide that will leave the preheater tower as SO_2, as a function of residence time in cyclone zone 3. t_3 was 8 s when determining $K_{2\to3}$.*

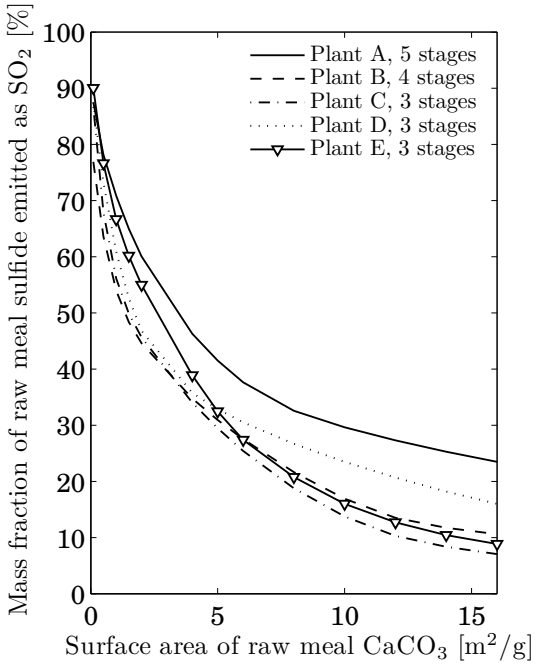

Figure 16.7: *Predicted fraction of raw meal sulphide that will leave the preheater tower as SO_2, as a function of the $CaCO_3$ surface area.*

Modelling of the CaO reaction shows that the surface area available for reaction is a key parameter in relation to SO_2 absorption. The $CaCO_3$ surface area for the plants modelled here was measured on the raw meal and calculated as the mass fraction of $CaCO_3$ times the raw meal surface area. The raw meal surface area enters the reaction equations used for simulating the preheater tower through the $CaCO_3$ grain radius (r_g), as seen in equation 15.48. Figure 16.7

shows the mass fraction of raw meal sulphide emitted as SO_2 as a function of the $CaCO_3$ surface area. The calculations were made with a $K_{2\rightarrow3}$ value of 0.05 m/s and ϵ, hel and t_3 as specified when estimating $K_{2\rightarrow3}$.
While changes of $K_{2\rightarrow3}$, hel and t_3 produced different trends among the plants, the emission unambiguously decreases with an increasing $CaCO_3$ surface area. Furthermore, the effect of changing the $CaCO_3$ surface area is much stronger than observed when changing $K_{2\rightarrow3}$, ϵ, hel and t_3. Thus, the $CaCO_3$ surface area is a key parameter when calculating SO_2 emission.
Comparing the measured emission data in Table 16.1 with the calculated emissions in Figure 16.7 shows that for plants A, C, D and E the $CaCO_3$ surface area should be between 3 and 4.5 m^2/g, while for plant B it should be larger than 15 m^2/g for the model to predict the right emission. No surface areas for raw meal $CaCO_3$ are available, but it is remarkable that, in four out of five cases, the model can predict the SO_2 emission if similar surface areas are used in the calculations.

16.3 Summary

Modelling the cement preheater tower is of great importance when predicting emissions, especially for new plants. A model was set-up by combining an overall mass balance, an energy balance and a cyclone reactor model. The cyclone stage model considers a cyclone stage as a reactor by dividing it into a riser section and a cyclone section. Each section is subdivided into three zones, each zone having unique features. In this manner the model accounts for heat exchange, particle residence time, different gas/solid residence time and major flow patterns. The model was evaluated against data from five full-scale plants, and the simulations showed that it was possible to predict cyclone temperatures and pyrite oxidation very well in all cases. The emission of SO_2 made it possible to predict satisfactorily in two out of five cases. The influence of the aeration factor for cyclone zone 3 (ϵ), the fraction of the riser duct used for heat exchange (hel), the residence of solid material in cyclone zone 3 (t_3) and the surface area of $CaCO_3$ ($A_{BET,CaCO_3}$) were investigated. It was found that the aeration factor did not affect the model. Both hel and t_3 turned out to influence the model in different ways depending on which plant was considered. The greatest effect was observed for the five-stage plant. The influence of both hel and t_3 could, in all cases, be explained by the temperatures in the top stages. The limestone surface area turned out, in all cases, to be a critical parameter, with a particularly large effect upon the calculated emission. The investigation of the limestone surface area showed that it was possible to satisfactorily predict the emission in four out of five cases, using a limestone surface area around 4 m^2/g. In general, the model turned out to be promising, but further evaluation against full-scale data is required for consolidation of the model.

Chapter 17

Final Conclusions and Recommendations

In the introduction to the thesis eight objectives were stated, which it was desired to fulfill. Here the obtained results are evaluated against these objectives and recommendations for future work will be given.
Two of the eight objectives were to gain knowledge about the reactions of CaO with SO_2 at relevant conditions. The four main findings in relation to the fundamental knowledge gained are:

- CO_2 strongly inhibits the reaction of SO_2 with CaO The inhibition is caused by CO_2 taking up reactive sites that otherwise would be available for reaction with SO_2. In addition, the larger molar volume of $CaCO_3$ compared to that of CaO, causes pore blockage, resulting in a reduction of surface area available for reaction.

- CaO conversion increases with surface area, while higher temperature only has a positive effect in atmospheric air. At high CO_2 concentrations no effect, or even a negative effect, on temperature is seen. The negative effect is most likely linked with the rate of inhibiting reactions increaseing faster with temperature than the CaO/SO_2 reaction rate.

- Oxygen was found not to influence the CaO/SO_2 reaction below 600 °C. That the reaction is independent of oxygen concentration shows that the reaction product of the CaO/SO_2 reaction is $CaSO_3$. From IR studies it was determined that both $CaSO_3$ and $CaSO_4$ could be found. However, the experimental results with oxygen shows that $CaSO_4$ is caused by oxidation of the formed $CaSO_3$.

- The observed results for CaO's reaction with SO_2 were shown to be limited by external and internal mass transfer, which indicates that the initial kinetic of the reactions are extremely fast.

The knowledge that has been gained in this work with regard to the CaO/SO_2 reaction leads to the conclusion that CaO recirculating inside the preheater tower does not influence the emission of SO_2 from preheater towers. Any CaO reaching the top stages would have been exposed to heavy carbonization before coming into contact with SO_2 and the experimental evidence in this thesis clearly shows that the CaO reactivity towards SO_2 decrease extremely fast when exposed to carbonating conditions.
Evaluation of CaO as a potential absorbent for reduction of SO_2 emissions must be seen in relation to the calcination experiments conducted. In these experiments it was found that it was possible to produce CaO with a large surface area if the CaO was produced by flash calcination at relatively low temperatures. However, the calcination experiments also led to the conclusion that it is difficult to produce CaO with a high surface area because temperatures around 800 °C are needed and the CO_2 formed promotes sintering. Heavy sintering of calcined material was also observed from the surface area measurements conducted on hot meals. These measurements showed that material withdrawn form the calciner can be expected to be heavily sintered. The calcination experiments and the measurements on hot meal has led to the conclusion that CaO produced from $CaCO_3$ is not well suited as an absorbent for reduction of SO_2 emissions.

Kinetic modelling is based on the experimental results obtained for the CaO/SO_2 reaction when CO_2 does not influence the reaction. In the modelling approach it was decided to leave out the carbonization reaction due to a lack of data. From the experiments it was determined that both external and internal mass transfer limitations should be included in the model. In order to do so it was decided to use a time-dependent grain model, with reaction between CaO and SO_2 at the interface between the product layer and the unreacted shrinking core of the non-porous CaO grains. The most important conclusions from the kinetic modelling are:

- The chemical reaction between CaO and SO_2 was found to be so fast, that the rate was exclusively dependent on solid state diffusion in the non-porous CaO grains. If it is assumed that all CaO molecules found as surface molecules has the same reactivity towards SO_2 and their reaction with $SO_2$is controlled by the chemical reaction, it can be shown that the chemical reaction should make a significant contribution to the observed results. However, this was not confirmed by the model

- For the solid-state diffusion of SO_2, activation energies between 90-140 kJ/mole were found using a least sum of squares fitting method. However, an activation energy of 115 kJ/mole was found to describe all data series very well, if the preexponential factor was adjusted accordingly.

Based on the modelling carried out in this study, it can be concluded that more knowledge about the surface reactions is needed in order to properly describe what happens in the initial phase

of the reaction. This is especially important if the inhibiting effect of CO_2 is to be incorporated ina model for how CaOreacts with SO_2 in a CO_2 atmosphere. It is recommended to investigate the surface reactions in the $CaO/SO_2/CO_2$ sytsem further.

In the objectives it was also stated that a goal was to set up a model for a cyclone stage considered as a reactor. Modelling of cyclones are complicated by the highly irregular flow pattern, where gas and solid thus are separated. This challenge has been solved by dividing a cyclone stage into different zones in order to account for gas/solid separation, different gas and solid residence times, heat exchange, etc.. The model was evaluated against SO_2 emission data from five different full scale plants. The reaction kinetics used for modelling the emission of SO_2 were based on previous work [2, 3]. The kinetic models derived for the CaO/SO_2 reaction was not included in the modelling, since it has been concluded that CaO does not make any significant contribution to the absorption of SO_2 within the preheater tower.
The model operates with three empirical mass transfer coefficients between the model zones, which are unknown but characteristic for this model. In the model evaluation it was chosen to put two of these equal to zero in order to reduce the number of fitting parameters in the initial evaluation. Hence the only fitting parameter used was the gas mass transfer coefficient ($K_{2\rightarrow3}$) between the high solid density cyclone zone, situated at the cyclone wall, and the low density solid zone, situated between the high solid density cyclone zone and the vortex. The main conclusions from the model evaluation are.

- Using one fitting parameter ($K_{2\rightarrow3}$) it was possible to satisfactorily predict the emission in two out of five cases. In the remaining three cases the model in two cases predicted an SO_2 emission that was too low and in one case it predicted a too high emission of SO_2.

- An investigation into model parameters, using a $K_{2\rightarrow3}$ value of 0.05 m/s, showed that the aeration factor in the high solid density zone did not affect the model. The residence time in the high solid density zone and the time for heat exchange, were also investigated showing both positive and negative effects upon the SO_2 emission depending on the plant simulated. However, the effects could in all cases be related to the cyclone temperature, which determine the rate at which SO_2 is formed and absorbed.

- From earlier experimental results [3] and the kinetic modelling it is known that the surface area of $CaCO_3$ available for SO_2 absorption is an important parameter. Therefore, the influence of the $CaCO_3$ surface area available for reaction with SO_2 was investigated. It was found that this parameter by far is the most important for the SO_2 emission predicted by the preheater tower model. In fact it was found that it was possible to predict satisfactorily the SO_2 emission in four out of the five cases, using a $CaCO_3$ surface area at around 4 m^2/g, instead of those measured, which was up to around 10 m^2/g. This result clearly shows how important the $CaCO_3$ surface area is for the model and thereby how crucial a

precise determination of this parameter is.

Based on the simulation results it can be concluded that the preheater tower model shows promising results. The model utilise experimental results obtained previously in projects investigating the SO_2 emission from preheater towers, and combined with the knowledge that CaO does not to any significant extend contribute to the absorption of SO_2 in the top stages, it has been possible to establish a new promising model for predicting emissions from preheater tower. The next step in predicting SO_2 emissions will be to investigate the SO_2 absorption kinetic on raw meals in order to determine what raw meal parameters are crucial in connection with SO_2 absorption. This should be combined with model evaluations against more plant data in order to identify parameters of special importance in the preheater tower model. In particular, the empirical transport coefficients of the cyclone model, characteristic for FLSmidth A/S preheater towers, could be determined.

Bibliography

[1] J. Bhatty, F. Kosmatka, and S. Miller, *Innovations in Portland Cement Manufacturing*. Portland Cement Association 2004, 2004.

[2] J. P. Hansen, *SO_2 Emissions from Cement Production*. PhD thesis, Technical University of Denmark, 2003.

[3] G. Hu, *Emission of SO_2 from Cement Production*. PhD thesis, Technical University of Denmark, 2007.

[4] E. Worrell, L. Price, N. Martin, C. Hendriks, and L. O. Meida, "Carbon dioxide emissions from the global cement industry," *Annual Review of Environment and Resources*, vol. 26, p. 303, 2001.

[5] Cembureau, *"Best Available Techniques" for the Cement Industry*. 2000.

[6] P. Hewlett, ed., *Leas Chemistry of Cement and Concrete*. Elsevier Ltd., 1998.

[7] H. Brundiek and H.-J. Poeschl, "Roller mill application for high moisture feed," *Cement Industry Technical Conference. 1997. XXXIX Conference Record., 1997 IEEE/PCA*, pp. 213–225, 1997.

[8] http://www.flsmidth.com.

[9] C. G. Manias, "Kiln burning systems: An overview," *Cement Americas*, pp. 6–17, 2005.

[10] FLSmidth A/S, "Dry process kiln systems."

[11] A. Helm and P. Rosholm, "State-of-the-art preheater design," *World Cement*, vol. 25, no. 3, p. 26, 1994.

[12] F. Strauss, E. Steinbiss, and A. Wolter, "Measurement of retention times in cement burning systems with the aid of radionuclides," *Zement-kalk-gips*, vol. 40, no. 9, pp. 441–446, 1987.

[13] R. Wolff and S. Alesi, "Improved preheater/calciner efficiency and capacity," *World Cement*, vol. 26, no. 12, p. 2, 1995.

[14] O. L. Jepsen and P. B. Nielsen, "New cyclone design improves pyroprocessing economics.," *IEEE Cement Industry Technical Conference (Paper)*, pp. 381–393, 1987.

[15] W. H. Duda, *Cement Data Book 1*. Bauverlaug GmbH, Wiesbaden und Berlin, 1985.

[16] X. Delong and H. Daohe, "Characteristics of momentum and heat transfer between gas and particles in a transport bed.," *Fluidization '85: Science and Technology, Conference Papers, Second China-Japan Symposium.*, pp. 445–455, 1985.

[17] C. Belot, D. Grouset, D. Goffe, C. Bertrand, B. Homassel, and J. Philippe, "Optimization of a cement plant preheating tower, equipped with a precalciner, burning pulverized coal," *Combustion Science and Technology*, vol. 93, no. 1, pp. 9–25, 1993.

[18] K. S. Mujumdar, K. Ganesh, S. B. Kulkarni, and V. V. Ranade, "Rotary cement kiln simulator (rocks): Integrated modeling of pre-heater, calciner, kiln and clinker cooler," *Chemical Engineering Science*, vol. 62, no. 9, pp. 2590–2607, 2007.

[19] G. Locher, "Mathematical models for the cement clinker burning process: Part 2: Preheater, calciner and bypass," *ZKG International*, vol. 55, no. 1, pp. 39–50, 2002.

[20] G. Locher, "Mathematical models for the cement clinker burning process part 5: Complete plant," *ZKG International*, vol. 55, no. 7, pp. 25–37, 2002.

[21] E. P. Agency, "Standards of performance for portland cement plants; proposed rules," tech. rep., Enviromental Protection Agency, 2008.

[22] B. Klotz, "New developments in precalciners and preheaters," *Cement Industry Technical Conference. 1997. XXXIX Conference Record., 1997 IEEE/PCA*, pp. 255–280, 1997.

[23] J. Salmento and R. Shenk, "Accurately predicting cement plant emissions," *IEEE-IAS/PCA 2004 Cement Industry Technical Conference*, pp. 333–343, 2004.

[24] C. Bech and L. Gundtoft, "Study of NO_x, SO_x, and CO mechanisms based on actual plant data," *Cement Industry Technical Conference, 1998. 40th Conference Record. 1998 IEEE/PCA*, pp. 141–154, 1998.

[25] G. Hu, K. Dam-Johansen, S. Wedel, and J. P. Hansen, "Decomposition and oxidation of pyrite," *Progress in Energy and Combustion Science*, vol. 32, no. 3, pp. 295–314, 2006.

[26] K. Bauer, J. Thormann, and L. Lohnherr, "Method of removing sulphur dioxide from cement kiln exhaust gases," 1999.

[27] W. W. Emmer, "Removal of sulfur oxides from waste gases by scrubbing with an aqueous slurry of finely comminuted limestone," 1996.

[28] J. P. Hansen and L. Skaarup, "Method and apparatus for hydration of a particulate or pulverulent material containing cao, hydrated product, and use of the hydrated product," 2005.

[29] J. P. Hansen, "Method and plant for manufacturing cement clinker," 2007.

[30] O. Heinemann, "Method of reducing volatile pollutants in the exhaust gases from a heat exchanger system," 2001.

[31] H.-W. Meyer and M. Siegert, "Method and apparatus for thermal processing of powder raw materials," 2004.

[32] L. Skaarup and J. P. Hansen, "Method and plant for preheating particulate or pulverulent material," 2005.

[33] K. Thomsen, "Method for reducing the sulphur dioxide content in the flue gas from a clinker production plant and apparatus for carrying out the method," 1993.

[34] K. Thomsen and F. Schomburg, "Removal of sulfur oxides from preheater off gases," 1999.

[35] K. Thomsen and S. Hundebol, "Method and apparatus for desulphurisation of exhaust gases," 2000.

[36] J. Ziegler and H. S. Erhard, "Method for dry desulfurizing flue gases," 1997.

[37] S. Miller and J. Hansen, "Methods for reducing so$_2$ emissions," *Cement Industry Technical Conference, 2004. IEEE-IAS/PCA*, pp. 79–92, 2004.

[38] J. Oates, *Lime and Limestone, Chemistry and Technology, Production and Uses*. Wiley-VCH, 1998.

[39] R. Boynton, *Chemistry and Technology of Lime and Limestone*. John Wiley & Sons, INC., 1980.

[40] $http://www.see.leeds.ac.uk/electronoptics/set3/rock\_27c.jpg$.

[41] K. Dam-Johansen, *Karakterisering af kalk*. DTU, 1987.

[42] F. Garcia-Labiano, A. Abad, L. de Diego, P. Gayen, and J. Adenez, "Calcination of calcium-based sorbents at pressure in a broad range of CO_2 concentrations," *Chemical Engineering Science*, vol. 57, no. 13, pp. 2381–2393, 2002.

[43] E. Baker, "Calcium oxide-carbon dioxide system in pressure range 1-300 atmospheres," *journal Of The Chemical Society*, no. FEB, p. 464, 1962.

[44] N. Hu and A. W. Scaroni, "Calcination of pulverized limestone particles under furnace injection conditions," *Fuel*, vol. 75, no. 2, pp. 177–186, 1996.

[45] G. D. Silcox, J. C. Kramlich, and D. W. Pershing, "Mathematical model for the flash calcination of dispersed $CaCO_3$ and $Ca(OH)_2$ particles," *Industrial & Engineering Chemistry Research*, vol. 28, no. 2, pp. 155–160, 1989.

[46] D. Beruto, L. Barco, A. Searcy, and G. Spinolo, "Characterization of the porous CaO particles formed by decomposition of $CaCO_3$ and $Ca(OH)_2$ in vacuum," *Journal of the American Ceramic Society*, vol. 63, no. 7-8, pp. 439–443, 1980.

[47] A. Fuertes, D. Alvarez, F. Rubiera, J. Pis, G. Marban, and J. Palacios, "Surface area and pore size changes during sintering of calcium oxide particles," *Chem. Eng. Comm.*, vol. 109, pp. 73–88, 1991.

[48] J. Agnew, E. Hampartsoumian, J. Jones, and W. Nimmo, "The simultaneous calcination and sintering of calcium based sorbents under a combustion atmosphere," *Fuel*, vol. 79, no. 12, pp. 1515–1523, 2000.

[49] C. Rodriguez-Navarro, E. Ruiz-Agudo, A. Luque, A. B. Rodriguez-Navarro, and M. Ortega-Huertas, "Thermal decomposition of calcite: Mechanisms of formation and textural evolution of CaO nanocrystals," *American Mineralogist*, vol. 94, no. 4, pp. 578–593, 2009.

[50] D. Glasson and P. O'Neill, "Reactivity of lime and related oxides – 16, 17, 18," *Journal of Applied Chemistry*, vol. 17, no. 4, pp. 91–106, 1967.

[51] R. H. Borgwardt, "Calcium oxide sintering in atmospheres containing water and carbon dioxide," *Industrial & Engineering Chemistry Research*, vol. 28, no. 4, pp. 493–500, 1989.

[52] R. Borgwardt, "Sintering of nascent calcium oxide," *Chemical Engineering Science*, vol. 44, no. 1, pp. 53–60, 1989.

[53] J. Chen and M. Shi, "A universal model to calculate cyclone pressure drop," *Powder Technology*, vol. 171, no. 3, pp. 184–191, 2007.

[54] K. Bruce, B. Gullett, and L. Beach, "Comparative SO_2 reactivity of CaO derived from $CaCO_3$ and $Ca(OH)_2$," *Aiche Journal*, vol. 35, no. 1, pp. 37–41, 1989.

[55] A. Wolter, S. Luger, and G. Schaefer, "The kinetics of the hydration of quicklime and zur kinetik der hydratation von branntkalk," *ZKG International*, vol. 57, no. 8, pp. 60–68, 2004.

[56] P. Halstead and A. Moore, "The thermal dissociation of calcium hydroxide," *Journal Of The Chemical Society*, no. SEP, pp. 3873–3875, 1957.

[57] H. Matsuda, T. Ishizu, S. Lee, and M. Hasatani, "Kinetic-study of $Ca(OH)_2/CaO$ reversible thermochemical reaction for thermal-energy storage by means of chemical-reaction," *Kagaku Kogaku Ronbunshu*, vol. 11, no. 5, pp. 542–548, 1985.

[58] M. Hartman and O. Trnka, "Thermal dehydration of calcium hydroxide .1. kinetic-model and parameters - comment," *Industrial & Engineering Chemistry Research*, vol. 33, no. 2, p. 448, 1994.

[59] R.-M. Dheilly, J. Tudo, and M. Queneudec, "Influence of climatic conditions on the carbonation of quicklime," *Journal of Materials Engineering and Performance*, vol. 7, no. 6, pp. 789–795, 1998.

[60] D. Glasson, "Reactivity of lime and related oxides – 2," *Journal of Applied Chemistry*, vol. 8, no. Part 12, pp. 793–803, 1958.

[61] A. Irabien, J. R. Viguri, F. Cortabitarte, and I. Ortiz, "Thermal dehydration of calcium hydroxide. 2. surface area evolution," *Industrial and Engineering Chemistry Research*, vol. 29, no. 8, pp. 1606–1611, 1990.

[62] A. Galwey and G. Laverty, "A kinetic and mechanistic study of the dehydroxylation of calcium hydroxide," *Thermochimica Acta*, vol. 228, pp. 359–378, 1993.

[63] C. R. Milne, G. D. Silcox, D. W. Pershing, and D. A. Kirchgessner, "Calcination and sintering models for application to high-temperature, short-time sulfation of calcium-based sorbents," *Industrial and Engineering Chemistry Research*, vol. 29, no. 2, pp. 139–149, 1990.

[64] G. Hu, K. Dam-Johansen, S. Wedel, and J. Peter Hansen, "Review of the direct sulfation reaction of limestone," *Progress in Energy and Combustion Science*, vol. 32, no. 4, pp. 386–407, 2006.

[65] R. H. Green, Don W.; Perry, *Perry's Chemical Engineers' Handbook (8th Edition)*. McGraw-Hill, 2008.

[66] G. Hu, K. Dam-Johansen, S. Wedel, and J. P. Hansen, "Enhancement of the direct sulfation of limestone by alkali metal salts, calcium chloride, and hydrogen chloride," *Industrial & Engineering Chemistry Research*, vol. 46, no. 16, pp. 5295–5303, 2007.

[67] G. Hu, K. Dam-Johansen, S. Wedel, and J. P. Hansen, "Direct sulfation of limestone," *Aiche Journal*, vol. 53, no. 4, pp. 948–960, 2007.

[68] G. Hu, L. Shang, K. Dam-Johansen, S. Wedel, and J. P. Hansen, "Initial kinetics of the direct sulfation of limestone," *AIChE Journal*, vol. 54, no. 10, p. 2663, 2008.

[69] G. Hu, K. Dam-Johansen, and S. Wedel, "Oriented nucleation and growth of anhydrite during direct sulfation of limestone," *Crystal Growth & Design*, vol. 8, no. 4, pp. 1181–1185, 2008.

[70] G. Krammer, C. Brunner, J. Khinast, and G. Staudinger, "Reaction of $Ca(OH)_2$ with SO_2 at low temperature," *Industrial & Engineering Chemistry Research*, vol. 36, no. 5, pp. 1410–1418, 1997.

[71] W. Wang, M. Hu, Y. Dong, and C. Ma, "Study on the Effect of CO_2 on the Consumption of Desulfurizing Agent $Ca(OH)_2$ in Flue Gas Desulfurization," *Industrial & Engineering Chemistry Research*, vol. 49, no. 3, pp. 1444–1449, 2010.

[72] F. J. Gutierrez Ortiz and P. Ollero, "A realistic approach to modeling an in-duct desulfurization process based on an experimental pilot plant study," *Chemical Engineering Journal*, vol. 141, no. 1-3, pp. 141–150, 2008.

[73] C. Ho, S. Shih, C. Liu, H. Chu, and C. Lee, "Kinetics of the sulfation of $Ca(OH)_2$ at low temperatures," *Industrial & Engineering Chemistry Research*, vol. 41, no. 14, pp. 3357–3364, 2002.

[74] J. Izquierdo, C. Fite, F. Cunill, M. Iborra, and J. Tejero, "Kinetic study of the reaction between sulfur dioxide and calcium hydroxide at low temperature in a fixed-bed reactor," *Journal of Hazardous Materials*, vol. 76, no. 1, pp. 113–123, 2000.

[75] A. Garea, J. Herrera, M. Renedo, J. Fernandez, and A. Irabien, "Thermogravimetric determination of the influence of water vapour in the FGD in-duct injection at low temperatures," *Journal of Chemical Technology and Biotechnology*, vol. 75, no. 6, pp. 484–490, 2000.

[76] A. Garea, J. Marques, and A. Irabien, "Modelling of in-duct desulfurization reactors," *Chemical Engineering Journal*, vol. 107, no. 1-3, Sp. Iss. SI, pp. 119–125, 2005.

[77] A. Garea, J. Marques, and A. Irabien, "Mechanistical and non-linear modelling approaches to in-duct desulfurization," *Chemical Engineering and Processing*, vol. 44, no. 7, pp. 709–715, 2005.

[78] M. Bausach, M. Pera-Titus, C. Fite, F. Cunill, J. Izquierdo, J. Tejero, and M. Iborra, "Kinetic modeling of the reaction between hydrated lime and SO_2 at low temperature," *AIChE Journal*, vol. 51, no. 5, pp. 1455–1466, 2005.

[79] A. Bueno-Lopez and A. Garcia-Garcia, "Combined SO_2 and NO_x removal at moderate temperature by a dual bed of potassium-containing coal-pellets and calcium-containing pellets," *Fuel Processing Technology*, vol. 86, no. 16, pp. 1745–1759, 2005.

[80] B. Gorkem and H. Oguz, "Development of an active sorbent from fly ash for dry desulphurization of simulated flue gas in a fluidized-bed reactor," *Chemical Engineering Journal*, vol. 119, no. 2-3, pp. 147–152, 2006.

[81] M. Yamamoto, S. Komaki, D. Nakajima, N. Matsushima, D. Liu, M. Nishioka, and M. Sadakata, "Enhancement of $Ca(OH)_2$/fly ash sorbent for the dry-desulfurization process," *Energy & Fuels*, vol. 20, no. 5, pp. 1901–1905, 2006.

[82] H. Tseng, M. Wey, C. Lin, and Y. Chang, "Pore structure effects on Ca-based sorbent sulfation capacity at medium temperatures: Activated carbon as sorbent/catalyst support," *Journal of the Air & Waste Management Association*, vol. 52, no. 11, pp. 1281–1287, 2002.

[83] I. Fernandez, A. Garea, and A. Irabien, "Flue-gas desulfurization at medium temperatures. Kinetic model validation from thermogravimetric data," *Fuel*, vol. 77, no. 7, pp. 749–755, 1998.

[84] N. Matsushima, Y. Li, M. Nishioka, M. Sadakata, H. Qi, and X. Xu, "Novel dry-desulfurization process using Ca(OH)(2)/fly ash sorbent in a circulating fluidized bed," *Environmental Science & Technology*, vol. 38, no. 24, pp. 6867–6874, 2004.

[85] Y. Li and M. Sadakata, "Study of gypsum formation for appropriate dry desulfurization process of flue gas," *Fuel*, vol. 78, no. 9, pp. 1089–1095, 1999.

[86] I. Fernandez, A. Garea, and A. Irabien, "SO_2 reaction with $Ca(OH)_2$, at medium temperatures (300-425 degrees c): kinetic behaviour," *Chemical Engineering Science*, vol. 53, no. 10, pp. 1869–1881, 1998.

[87] A. Newman, *Chemistry of Clays and Clay Minerals*. Longman Scientific & Technical, 1987.

[88] W. Worrall, *Clays their nature, origin and general properties*. Maclaren and Sons, 1968.

[89] K. Dam-Johansen and K. ï¿½stergaard, "High-temperature reaction between sulphur dioxide and limestone-i. comparison of limestones in two laboratory reactors and a pilot plant," *Chemical Engineering Science*, vol. 46, no. 3, pp. 827–837, 1991.

[90] A. Vinokurov, L. Derlyukova, and V. Evdokimov, "Chemisorption of sulfur-dioxide on iron(iii) oxide," *Bulletin of the Academy of Sciences of the USSR Division of Chemical Science*, vol. 36, pp. 1337–1340, 1987.

[91] T. C. Keener and W. T. Davis, "Study of the reaction of sulfur di oxide with sodium bi carbonate and sodium carbonate," *Journal of the Air Pollution Control Association*, vol. 34, no. 6, pp. 651–654, 1984.

[92] M. Hartman, O. Trnka, and V. Vesely, "Heats of decomposition and equilibrium dissociation pressures of the magnesian and calcareous compounds in desulfurization technologies," *Collection of Czechoslovak Chemical Communications*, vol. 58, no. 8, pp. 1885–1890, 1993.

[93] E. Oneill, D. Keairns, and W. Kittle, "Thermogravimetric study of sulfation of limestone and dolomite, effect of calcination conditions," *Thermochimica Acta*, vol. 14, no. 1-2, pp. 209–220, 1976.

[94] K. Murthi, D. Harrison, and R. Chan, "Reaction of sulfur dioxide with calcined limestones and dolomites," *Environmental Science & Technology*, vol. 5, no. 9, p. 776, 1971.

[95] C.-H. Cheng and C.-I. Lin, "Effects of additives on the reaction of SO_2 with MgO," *Journal of the Chinese Institute of Chemical Engineers*, vol. 27, no. 1, pp. 53–56, 1996.

[96] A. Fuertes, G. Velasco, T. Alvarez, and M. Fernandez, "Sulfation of dolomite particles at high CO_2 partial pressures," *Thermochimica Acta*, vol. 254, pp. 63–78, 1995.

[97] H.-G. Wiedemann, A. Boller, and G. Bayer, "Thermogravimetric studies of the reactions between dolomite and sulfur dioxide," *Solid State Ionics*, vol. 43, pp. 53–60, 1990.

[98] T. Kaljuvee, A. Trikkel, and R. Kuusik, "Decarbonization of natural lime-containing materials and reactivity of calcined products towards SO_2 and CO_2," *Journal of Thermal Analysis and Calorimetry*, vol. 64, no. 3, pp. 1229–1240, 2001.

[99] T. Kaljuvee, A. Trikkel, R. Kuusik, and V. Bender, "The role of MgO in the binding of SO_2 by lime-containing materials," *Journal of Thermal Analysis and Calorimetry*, vol. 80, no. 3, pp. 591–597, 2005.

[100] D. Kocaefe, D. Karman, and F. R. Steward, "Comparison of the sulfation rates of calcium, magnesium and zinc oxides with SO_2 and SO_3.," *Canadian Journal of Chemical Engineering*, vol. 63, no. 6, pp. 971–977, 1985.

[101] R. Borgward and R. Harvey, "Properties of carbonate rocks related to SO_2 reactivity," *Environmental Science & Technology*, vol. 6, no. 4, p. 350, 1972.

[102] G. Mura, A. Lallai, and P. Olla, "On the kinetics of dry desulfurization with calcium oxide," *The Chemical Engineering Journal*, vol. 46, no. 3, pp. 119–128, 1991.

[103] R. H. Borgwardt, "Kinetics of the reaction of SO_2 with calcined limestone," *Environ Sci Technol*, vol. 4, no. 1, pp. 59–63, 1970.

[104] D. Marsh and D. Ulrichson, "Rate and diffusional study of the reaction of calcium-oxide with sulfur-dioxide," *Chemical Engineering Science*, vol. 40, no. 3, pp. 423–433, 1985.

[105] R. H. Borgwardt and K. R. Bruce, "Effect of specific surface area on the reactivity of CaO with SO_2," *AIChE Journal*, vol. 32, no. 2, pp. 239–246, 1986.

[106] C. Tullin and E. Ljungstrom, "Reaction between calcium-carbonate and sulfur-dioxide," *Energy & Fuels*, vol. 3, no. 3, pp. 284–287, 1989.

[107] Z. Qin, "Thermogravimetric studies of the reaction of CaO with SO_2," *Journal of Thermal Analysis*, vol. 45, no. 1, pp. 211–219, 1995.

[108] B. Gullett and K. Bruce, "Pore distribution changes of calcium-based sorbents reacting with sulfur-dioxide," *AICHE Journal*, vol. 33, no. 10, pp. 1719–1726, 1987.

[109] C. Milne, G. Silcox, D. Pershing, and D. Kirchgessner, "High-temperature, short-time sulfation of calcium-based sorbents .2. experimental-data and theoretical-model predictions," *Industrial & Engineering Chemistry Research*, vol. 29, no. 11, pp. 2201–2214, 1990.

[110] L. Shi and X. Xu, "Study of the effect of fly ash on desulfurization by lime," *Fuel*, vol. 80, no. 13, pp. 1969–1973, 2001.

[111] S.-M. Shih, J.-T. Hung, T.-Y. Wang, and R.-B. Lin, "Kinetics of the reaction of sulfur dioxide with calcium oxide powder," *Journal of the Chinese Institute of Chemical Engineers*, vol. 35, no. 4, pp. 447–454, 2004.

[112] R. H. Borgwardt, K. R. Bruce, and J. Blake, "Investigation of product-layer diffusivity for CaO sulfation.," *Industrial & Engineering Chemistry Research*, vol. 26, no. 10, pp. 1993–1998, 1987.

[113] R. T. Yang, M.-S. Shen, and M. Steinberg, "Fluidized-bed combustion of coal with lime additives: catalytic sulfation of lime with iron compounds and coal ash.," *Environ Sci Technol*, vol. 12, no. 8, pp. 915–918, 1978.

[114] M. Mucoz-Guillena, A. Linares-Solano, and C. Salinas-Martinez de Lecea, "A study of CaO-SO_2 interaction," *Applied Surface Science*, vol. 81, no. 4, pp. 409–415, 1994.

[115] M. Muï¿½oz-Guillena, A. Linares-Solano, and C. Salinas-Martï¿½nez de Lecea, "A study of CaO-SO_2 interaction in the presence of O_2," *Applied Surface Science*, vol. 81, no. 4, pp. 417–425, 1994.

[116] M. Low, A. Goodsel, and N. Takezawa, "reactions of gaseous pollutants with solids .1. infrared study of sorption of SO_2 on CaO," *Environmental Science & Technology*, vol. 5, no. 12, pp. 1191–&, 1971.

[117] T. Ishizuka, H. Kabashima, T. Yamaguchi, K. Tanabe, and H. Hattori, "Initial step of flue gas desulfurization-an IR study of the reaction of SO_2 with NO_x on CaO," *Environmental Science & Technology*, vol. 34, no. 13, pp. 2799–2803, 2000.

[118] S. Ghardashkhani and D. Cooper, "A thermogravimetric study of the reaction between sulfur-dioxide and calcium-oxide," *Thermochimica Acta*, vol. 161, no. 2, pp. 327–337, 1990.

[119] D. Allen and A. Hayhurst, "Reaction between gaseous sulfur dioxide and solid calcium oxide - mechanism and kinetics," *Journal of the chemical society-faraday transactions*, vol. 92, no. 7, pp. 1227–1238, 1996.

[120] G. A. Simons, T. E. Parker, and J. R. Morency, "The oxygen reaction order of SO_2 with CaO," *Combustion and Flame*, vol. 74, no. 1, pp. 107–110, 1988.

[121] J. Dennis and A. Hayhurst, "Mechanism of the sulfation of calcined limestone particles in combustion gases," *Chemical Engineering Science*, vol. 45, no. 5, pp. 1175–1187, 1990.

[122] L. Shi and X. Xu, "Partially sulfated lime-fly ash sorbents activated by water or steam for SO_2 removal at a medium temperature," *Energy & Fuels*, vol. 19, no. 6, pp. 2335–2339, 2005.

[123] M. Stouffer and H. Yoon, "An investigation of CaO sulfation mechanisms in boiler sorbent injection," *AICiE Journal*, vol. 35, no. 8, pp. 1253–1262, 1989.

[124] J. Partanen, P. Backman, R. Backman, and M. Hupa, "Absorption of HCl by limestone in hot flue gases. part i: the effects of temperature, gas atmosphere and absorbent quality," *Fuel*, vol. 84, no. 12-13, pp. 1664–1673, 2005.

[125] M. Hartman and O. Trnka, "Reactions between calcium-oxide and flue-gas containing sulfur-dioxide at lower temperatures," *AICHE Journal*, vol. 39, no. 4, pp. 615–624, 1993.

[126] K. Iisa, C. Tullin, and M. Hupa, "Simultaneous sulfation and recarbonation of calcined limestone under PFBC conditions," *11 th. International Conference on Fluidized Bed Combustion ASME 1991*, pp. 83–90, 1991.

[127] Y. Suyadal and H. Oguz, "Dry desulfurization of simulated flue gas in a fluidized-bed reactor for a broad range of SO_2 concentration and temperature: A comparison of models," *Industrial & Engineering Chemistry Research*, vol. 38, no. 8, pp. 2932–2939, 1999.

[128] P. Alvfors and G. Svedberg, "Modelling of the simultaneous calcination, sintering and sulphation of limestone and dolomite," *Chemical Engineering Science*, vol. 47, no. 8, pp. 1903–1912, 1992.

[129] S. K. Bhatia and D. D. Perlmutter, "Effect of pore structure on fluid-solid reactions: application to the SO_2-lime reaction.," *AIChE Journal*, vol. 27, no. 2, pp. 226–234, 1981.

[130] C. R. Milne, G. D. Silcox, D. W. Pershing, and D. A. Kirchgessner, "High-temperature, short-time sulfation of calcium-based sorbents. 1. theoretical sulfation model," *Industrial & Engineering Chemistry Research*, vol. 29, no. 11, pp. 2192–2201, 1990.

[131] W. Wang and I. Bjerle, "Modeling of high-temperature desulfurization by Ca-based sorbents - part i. fundamental processes," *Chemical Engineering Science*, vol. 53, no. 11, pp. 1973–1989, 1998.

[132] M. Hartman and R. W. Coughlin, "Reaction of sulfur dioxide with limestone and the grain model.," *AIChE J*, vol. 22, no. 3, pp. 490–498, 1976.

[133] O. Levenspiel, *Chemical reaction engineering; an introduction to the design of chemical reactors*. Wiley New York,, 1962.

[134] C. Wang, X. Shen, and Y. Xu, "Investigation on sulfation of modified Ca-based sorbent," *Fuel Processing Technology*, vol. 79, no. 2, pp. 121–133, 2002.

[135] C. Hsia, G. Stpierre, K. Raghunathan, and L. Fan, "Diffusion through $CaSO_4$ formed during the reaction of CaO with SO_2 and O_2," *AIChE Journal*, vol. 39, no. 4, pp. 698–700, 1993.

[136] C. Hsia, G. St. Pierre, and L.-S. Fan, "Isotope study on diffusion in $CaSO_4$ formed during sorbent-flue-gas reaction," *AIChE Journal*, vol. 41, no. 10, pp. 2337–2340, 1995.

[137] D. Alvarez and J. Carlos Abanades, "Determination of the critical product layer thickness in the reaction of CaO with CO_2," *Industrial and Engineering Chemistry Research*, vol. 44, no. 15, pp. 5608–5615, 2005.

[138] J. C. Abanades and D. Alvarez, "Conversion limits in the reaction of CO_2 with lime," *Energy and Fuels*, vol. 17, no. 2, p. 308, 2003.

[139] N. H. Florin and A. T. Harris, "Reactivity of cao derived from nano-sized $caco_3$ particles through multiple co_2 capture-and-release cycles," *Chemical Engineering Science*, vol. 64, no. 2, pp. 187–191, 2009.

[140] R. Barker, "Reversibility of the reaction $CaCO_3$ reversible reaction CaO plus CO_2.," *J Appl Chem Biotechnol*, vol. 23, no. 10, pp. 733–742, 1973.

[141] D. Alvarez and J. C. Abanades, "Pore-size and shape effects on the recarbonation performance of calcium oxide submitted to repeated calcination/recarbonation cycles," *Energy & Fuels*, vol. 19, no. 1, pp. 270–278, 2005.

[142] S. K. Bhatia and D. D. Perlmutter, "Effect of the product layer on the kinetics of the CO_2-lime reaction.," *AIChE Journal*, vol. 29, no. 1, pp. 79–86, 1983.

[143] P. Sun, J. R. Grace, C. J. Lim, and E. J. Anthony, "Determination of intrinsic rate constants of the CaO-CO_2 reaction," *chemical Engineering Science*, vol. 63, no. 1, pp. 47–56, 2008.

[144] R. T. Symonds, D. Y. Lu, A. Macchi, R. W. Hughes, and E. J. Anthony, "CO_2 capture from syngas via cyclic carbonation/calcination for a naturally occurring limestone: Modelling and bench-scale testing," *Chemical Engineering Science*, vol. 64, no. 15, pp. 3536–3543, 2009.

[145] H. Gupta and L.-S. Fan, "Carbonation-calcination cycle using high reactivity calcium oxide for carbon dioxide separation from flue gas," *Industrial and Engineering Chemistry Research*, vol. 41, no. 16, p. 4035, 2002.

[146] K. Kyaw, M. Kanamori, H. Matsuda, and M. Hasatani, "Study of carbonation reactions of Ca-mg oxides for high temperature energy storage and heat transformation," *Journal of Chemical Engineering of Japan*, vol. 29, no. 1, p. 112, 1996.

[147] D. Mess, A. F. Sarofim, and J. P. Longwell, "Product layer diffusion during the reaction of calcium oxide with carbon dioxide," *Energy & Fuels*, vol. 13, no. 5, pp. 999–1005, 1999.

[148] A. Dedman and A. Owen, "Calcium cyanamide synthesis .4. reaction CaO+CO_2 = $CaCO_3$," *Transactions of the Faraday Society*, vol. 58, no. 478, p. 2027, 1962.

[149] W. Oakeson and I. Cutler, "Effect of CO_2 pressure on the reaction with CaO," *Journal of the American Ceramic Society*, vol. 62, no. 11-1, pp. 556–558, 1979.

[150] E. Bouquet, G. Leyssens, C. Schoennenbeck, and P. Gilot, "The decrease of carbonation efficiency of CaO along calcination-carbonation cycles: Experiments and modelling," *Chemical Engineering Science*, vol. 64, no. 9, pp. 2136–2146, 2009.

[151] V. Manovic and E. J. Anthony, "Sequential SO_2/CO_2 capture enhanced by steam reactivation of a CaO-based sorbent," *Fuel*, vol. 87, no. 8-9, pp. 1564–1573, 2008.

[152] V. Manovic and E. J. Anthony, "Improvement of CaO-based sorbent performance for CO_2 looping cycles," *Thermal Science*, vol. 13, no. 1, pp. 89–104, 2009.

[153] P. Sun, J. R. Grace, C. J. Lim, and E. J. Anthony, "Investigation of attempts to improve cyclic CO_2 capture by sorbent hydration and modification," *Industrial & Engineering Chemistry Research*, vol. 47, no. 6, pp. 2024–2032, 2008.

[154] C. Salvador, D. Lu, E. Anthony, and J. Abanades, "Enhancement of CaO for CO_2 capture in an FBC environment," *Chemical Engineering Journal*, vol. 96, no. 1-3, pp. 187–195, 2003.

[155] D. Beruto, L. Barco, and A. Searcy, "Rearrangement of porous CaO aggregates during calcite decomposition in vacuum," *Journal of the American Ceramic Society*, vol. 66, no. 12, pp. 893–896, 1983.

[156] J. Ewing, D. Beruto, and A. Searcy, "Nature of CaO produced by calcite powder decomposition in vacuum and in CO_2," *Journal of the American Ceramic Society*, vol. 62, no. 11-1, pp. 580–584, 1979.

[157] H. S. Fogler, *Elements of Chemical Reaction Engineering*. Prentice Hall, 2006.

[158] W. Massman, "A review of the molecular diffusivities of H_2O, CO_2, CH_4, CO, O_3, SO_2, NH_3, N_2O, NO, and NO_2 in air, O_2 and N_2 near stp - polar and polyatomic gases," *Atmospheric Environment*, vol. 32, no. 6, pp. 1111–1127, 1998.

[159] A. H. Kristensen, A. Thorbjorn, M. P. Jensen, M. Pedersen, and P. Moldrup, "Gas-phase diffusivity and tortuosity of structured soils," *Journal of Contaminant Hydrology*, vol. 115, no. 1-4, pp. 26–33, 2010.

[160] T. Gimmi, H. Fluhler, B. Studer, and A. Rasmuson, "Transport of volatile chlorinated hydrocarbons in unsaturated aggregated media," *Water Air and Soil Pollution*, vol. 68, no. 1-2, pp. 291–305, 1993.

[161] J. van Brakel and P. Heertjes, "Analysis of diffusion in macroporous media in terms of a porosity, a tortuosity and a constrictivity factor," *International Journal of Heat and Mass Transfer*, vol. 17, no. 9, pp. 1093 – 1103, 1974.

[162] F. Campbell, A. Hills, and A. Paulin, "Transport properties of porous lime and their influence on the decomposition of porous compacts of calcium carbonate," *Chemical Engineering Science*, vol. 25, no. 6, pp. 929 – 942, 1970.

[163] Y. Arai, T. Yasue, N. Nagata, and H. Shino, "Crystallographic data for new phases in the caso$_3$-h$_2$o system," *Bulletin Of The Chemical Society Of Japan*, vol. 55, no. 3, pp. 738–741, 1982.

[164] I. Barin, *Thermochemical data of pure substances Vol. I & II*. VCH, 1995.

[165] $http://webbook.nist.gov/chemistry/$.

[166] A. Hoffman and S. L.E., *Gas Cyclones and Swirl Tubes*. Springer, 2002.

[167] T. Petersen, "Modeling of cyclone reactors," Master's thesis, Technical University of Denmark, 2010.

[168] Y. Tsuji and Y. Morikawa, "Ldv measurements of an air-solid two-phase flow in a horizontal pipe," *Journal of Fluid Mechanics*, vol. 120, pp. 385–409, 1982.

[169] N. Huber and M. Sommerfeld, "Characterization of the cross-sectional particle concentration distribution in pneumatic conveying systems," *Powder Technology*, vol. 79, no. 3, pp. 191–210, 1994.

[170] M. Sommerfeld and J. Kussin, "Wall roughness effects on pneumatic conveying of spherical particles in a narrow horizontal channel," *Powder Technology*, vol. 142, no. 2-3, pp. 180–192, 2004.

[171] T. Y. Quek, C.-H. Wang, and M. B. Ray, "Dilute gas-solid flows in horizontal and vertical bends," *Industrial & Engineering Chemistry Research*, vol. 44, no. 7, pp. 2301–2315, 2005.

[172] H. Akilli, E. Levy, and B. Sahin, "Gas-solid flow behavior in a horizontal pipe after a 90° vertical-to-horizontal elbow," *Powder Technology*, vol. 116, no. 1, pp. 43–52, 2001.

[173] T. Frank, K.-P. Schade, and D. Petrak, "Numerical simulation and experimental investigation of a gas-solid two-phase flow in a horizontal channel," *International Journal of Multiphase Flow*, vol. 19, no. 1, pp. 187–198, 1993.

[174] A. Yilmaz and E. K. Levy, "Formation and dispersion of ropes in pneumatic conveying," *Powder Technology*, vol. 114, no. 1-3, pp. 168–185, 2001.

[175] M. Hidayat and A. Rasmuson, "Numerical assessment of gas-solid flow in a u-bend," *Chemical Engineering Research and Design*, vol. 82, no. 3, pp. 332–343, 2004.

[176] B. Kuan, W. Yang, and M. Schwarz, "Dilute gas-solid two-phase flows in a curved 90° duct bend: Cfd simulation with experimental validation," *Chemical Engineering Science*, vol. 62, no. 7, pp. 2068–2088, 2007.

[177] M. Hidayat and A. Rasmuson, "Some aspects on gas-solid flow in a u-bend: Numerical investigation," *Powder Technology*, vol. 153, no. 1, pp. 1–13, 2005.

[178] R. Schallert and E. Levy, "Effect of a combination of two elbows on particle roping in pneumatic conveying," *Powder Technology*, vol. 107, no. 3, pp. 226–233, 2000.

[179] M. Hidayat and A. Rasmuson, "A computational investigation of non-isothermal gas-solid flow in a u-bend," *Powder Technology*, vol. 175, no. 2, pp. 104–114, 2007.

[180] S. M. El-Behery, M. H. Hamed, M. El-Kadi, and K. Ibrahim, "Cfd prediction of air-solid flow in 180° curved duct," *Powder Technology*, vol. 191, no. 1-2, pp. 130–142, 2009.

[181] C. Satterfield and F. Feakes, "Kinetics of the thermal decomposition of calcium carbonate," *AIChE journal*, vol. 5, no. 1, pp. 115–122, 1959.

List of Symbols

χ	Particle velocity as fraction of gas velocity	$\frac{m/s}{m/s}$
$\Delta H_{reac,i}$	Enthalpy of reaction for i	$\frac{J}{mole}$
$\Delta H_{vap,i}$	Enthalpy of vaporization of i	$\frac{J}{mole}$
ϵ	Aeration factor for cyclone zone 3	$\frac{m^3}{m^3}$
γ	Kinematic viscosity	$Pa \cdot s$
ν_{amb}	Volume flow at ambient temperature	$\frac{m^3}{s}$
$\overline{\rho}_i$	Molar density of i	$\frac{kg}{m^3}$
ϕ	Particle porosity	
ϕ_{int}	Particle porosity before reaction	
ψ	Dimensionless factor in Arrhenius expression	
ρ_i	Gas density of i	$\frac{kg}{m^3}$
ρ_i	True density of i	$\frac{kg}{m^3}$
ρ_p	Particle density	$\frac{kg}{m^3}$
ρ_{solid}	Bulk density of solid material	kg/m^3
τ	Dimensionless time	
τ_p	Tortuosity factor	
ξ	Fraction of particle where reaction takes place	
A_{BET}	BET surface area	$\frac{m^2}{kg}$
Bi_m	Mass transfer Biot numer	
$C_{i,bulk}$	Bulk concentration of i	$\frac{mol}{m^3}$
$C_{i,c}$	Concentration of i at product/unreacted core interface	$\frac{mol}{m^3}$
$C_{i,g}$	Concentration of i in grain product layer	$\frac{mol}{m^3}$
$C_{i,surface}$	Surface concentration of i	$\frac{mol}{m^3}$
C_i	Concentration of i	$\frac{mol}{m^3}$
C_M	Mears criterion	

$C_{p,s}$	Heat capacity of solid materail	$\frac{J}{mole \cdot K}$
C_{WP}	Weisz-Prater modulus	
D_0	Preexponential factor in Arrhenius expression for solid state diffusion coefficient	$\frac{m^2}{s}$
D_{bend}	Diameter of reactor bend	m
$D_{critical}$	The particle diameter at which diffusion becomes significant	m
$D_{e,i}$	Effective pore diffusion coefficient for i	$\frac{m^2}{s}$
$D_{i,s}$	Solid state diffusion coefficient for i	$\frac{m^2}{s}$
D_i	Diffusion coefficient for i	$\frac{m^2}{s}$
D_{tube}	Diameter of reactor tube	m
E	Reaction energy	$\frac{J}{mole}$
$E_{a,i}$	Activation energy for reaction of component i	$\frac{J}{mole}$
$G_{j,top}$	Gas flow through top of cyclone j	$\frac{kg}{s}$
H	Height of cyclone stage	m
h_g	Convective heat transfer coefficient	$\frac{W}{m^2 \cdot K}$
H_i	Enthalpy of component i	$\frac{J}{mole}$
hel	Fraction of riser duct used for heat exchange	
$K_{1\rightarrow 2}$	Mass transfer coefficient between cyclone zone 1 and 2	$\frac{m}{s}$
$K_{2\rightarrow 3}$	Mass transfer coefficient between cyclone zone 2 and 3	$\frac{m}{s}$
$K_{g,i}$	Mass transfer coefficient for i in the gas phase	$\frac{m}{s}$
K_g	Heat transfer coefficient for gas	$\frac{W}{m^2 \cdot K}$
$K_{i,0}$	Reference rate constant for i	$\frac{kg\ i}{s \cdot kg\ solid}$
$K_{i/m}$	Rate constant for the reaction between i and m	$\frac{m}{s}$
K_i	Rate constant for i	$\frac{kg\ i}{s \cdot kg\ solid}$
K_s	Thermal conductivity of solid	$\frac{W}{m \cdot K}$
L_1	Length of riser zone 3	m
L_2	Length of riser zone 2 plus 3	m
L_{tube}	Length of reactor tube	m
M_i	Molar mass of i	$\frac{kg}{mole}$
n	Reaction order	
N_{bends}	Number of reator bends	
N_{disp}	Number of reator diamerters used for paricle dispersion	
n_i	Moles of i	$mole$
Nu	Nusselt number	

P	Pressure	Pa
P_i	Partial pressure of i	Pa
$P_{i,0}$	Constant in Clausius-Claperon expression for i	Pa
$P_{i,eq}$	Equilibrium pressure of i	Pa
$Q_{i,particle}$	Mass fraction of particles with size i	$\frac{kg}{kg}$
$Q_{i/m_{tot}}$	Mass fraction of i compared to the total mass	$\frac{kg}{kg}$
R	Radius	m
r	Radius	m
r_g	Grain radius	m
r_i	Reaction rate of i	$\frac{mole}{s}$
R_p	Particle radius	m
r_R	Radius of riser duct	m
r_z	Radius of cyclone zone z	m
R_{gas}	Universal gas constant	$\frac{J}{K \cdot mole}$
$R_{i,g}$	Reaction rate of i in gas phase	$\frac{kg\ i}{s \cdot kg\ gas}$
$R_{i,s}$	Reaction rate of i in solid phase	$\frac{kg\ i}{s \cdot kg\ solid}$
$r'''_{obs,i}$	Observed reaction rate for i	$\frac{mole}{m^3 \cdot s}$
Re	Reynolds number	
Sc	Schmidts number	
Sh	Sherwoods number	
T	Temperature	K
t	Time	s
T^*	Dimensionless temperature	
T_{amb}	Ambient temperature	K
t_{bends}	Residence time in bends	s
T_{bulk}	Bulk temperature	K
t_{disp}	Residence time used for particle dispersion	s
T_g	Gas temperature	K
T_j	Temperature in cyclone stage j	K
T_{reac}	Reactor temperature	K
T_{ref}	Reference temperature	K
t_r	Total reaction time	s
$t_{straight}$	Residence time in straight parts of reactor	s

$T_{surface}$	Surface temperature	K
T_s	Solid temperature	K
U_r	Radial gas flow	$\frac{m^3}{s}$
U_r^*	Dimensionless radial gas flow	
$U_{r,0}$	Maximum radial gas flow	$\frac{m^3}{s}$
V_i	Molar volume of i	$\frac{mole}{m^3}$
V_p	volume of particles	m^3
$V_{g,0}$	Gas flow in inlet to cyclone section	$\frac{m^3}{s}$
$V_{g,z}$	Gas flow in zone z	$\frac{m^3}{s}$
v_{gas}	Linear gas velocity	$\frac{m}{s}$
$W_{g,z}$	Dimensionless gas flow in zone z	
$w_{j,bot}$	Solid mass flow through bottom of cyclone j	$\frac{kg}{s}$
$w_{j,top}$	Solid mass flow through top of cyclone j	$\frac{kg}{s}$
W_p	Mass flow of particles	$\frac{kg}{s}$
x	Distance	m
$x_{i,bulk}$	Mole fraction of i in bulk gas	$\frac{mole}{mole}$
$X_{i,z}$	Solid mass fraction of i in zone z	$\frac{kg}{kg}$
$X_{i,z}^*$	Dimensionless solid mass fraction of i in zone z	
$x_{i/Ca}$	Mole of i per mole of Ca	$\frac{mole}{mole}$
X_i	Dimensionless concentration of i in gas phase	
x_i	Mole fraction of i	$\frac{mole}{mole}$
$x_{s,j}$	Separation efficiency of cyclone j	
$X_{SO_2/basis,g}$	Conversion of a grain basis with respect to SO_2	$\frac{mole}{mole}$
$X_{SO_2/basis}$	Conversion of basis with respect to SO_2	$\frac{mole}{mole}$
Y	Dimensionless concentration of i in product layer	
$Y_{i,z}$	Gas mass fraction of i in zone z	$\frac{kg}{kg}$
$Y_{i,z}^*$	Dimensionless gas mass fraction of i in zone z	
$y_{solid,z}$	Solid-gas ratio in in zone z	$\frac{kg}{kg}$
Z	Dimensionless particle diameter	
z	Dimensionless distance	

Appendix A

Verification of Set-up

Here, the entrained flow reactor set-up will be evaluated in order confirm the reliability of the reaction data obtained. Furthermore, the standard deviation for the obtained date will be determined, while the flow pattern in the entrained flow reactor will be evaluated in order to estimate the influence of the horizontal arrangement with U-bends used for the reactor tube.

A.1 Gas Sampling

As mentioned earlier, gas sampling does not discriminate between particles and gas. The separation takes place in the particle filter located at a distance of about 0.5 m from the gas sampling point. Carrying out experiments particles will accumulate in the filter, why it has been investigated if this accumulation affects the SO_2 concentration. This was achieved by measuring the change in SO_2 concentration of a known calibration gas, with and without CaO particles in the filter. The results showed that the variation in the SO_2 concentration was less than 2 ppm, which was independent of whether the filter contained particles or not, which is why the influence of SO_2 absorption in the particle filter can be neglected.
The sampled gas/particle mixture cools from the reactor temperature to the particle filter temperature in the pipe connecting the gas sampling point with the particle filter. The inner diameter of the pipe is 1.4 mm and the gas flow is 2.4 Nl/min, corresponding to a gas residence time in the sampling pipe of 0.02 s, calculated at ambient temperature. A residence time of 0.02 s corresponds, in some cases, to 25 % of the contact time, which is why reactions in the sampling pipe may affect the observed results. An investigation of this was conducted by comparing the amount of particles collected in the filter to the amount expected if the particle concentration in the sampled gas were equal to the concentration in the reactor tube. Consequently, it was found that particle concentration in the sampled gas is only about 10 % of the concentration in the reactor tube, which strongly reduces the influence of the gas sampling pipe. Low particle concentration, along with cooling of sample gas, entails that the influence of reactions in the sampling pipe is considered negligible for the observed results.

A.2 Solid Material Injection

The effect of particle feeding was investigated in six experiments by feeding between 600 and 1500 g/hr of inert sand particles into the entrained flow reactor. Figure A.1 shows the SO_2 concentration measured

in one of these experiments, highlighting that steady-state concentration is slightly lower when sand particles are fed into the reactor. On average, the SO_2 concentration dropped by 4 ppm with a standard deviation of the same size, which is why it can be concluded that injecting solid material, in itself, does not affect the observed results.

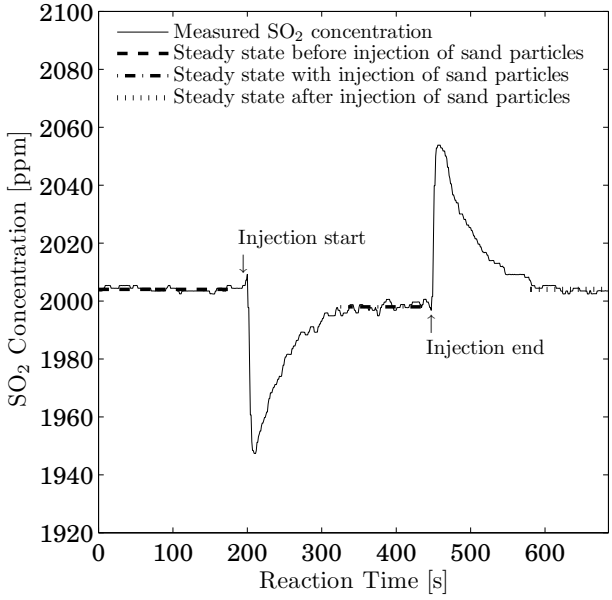

Figure A.1: *Effect on SO_2 concentration when inert sand particles are fed to the entrained flow reactor.*

A.3 Temperature Profile

In Figure A.3 the temperature is measured along the reactor tube is shown as a function of the distance from the mixing point (see also Figure 8.1). It is apparent that the temperature variation between V1 and the reactor outlet (the reactor outlet is at the right boundary of the figure) is only about 3 °C, with the variation being a little larger when particles are injected into the system. The set point for the oven temperature during the experiment is 575 °C, which is not obtained. In all experiments the measured temperature is lower than the oven set point, with a deviation up to 15 °C. However, the temperature variation from V1 to the reactor outlet is, in all experiments, observed at about 3 °C, which is considered isothermal conditions.

A.4 Reproducibility of Data

In order to determine the standard deviation for the entrained flow reactor, a number of data points were repeated up to seven times. In Figure A.2 the standard deviations obtained from the repeated experiments are shown as a function of the SO_2/Ca conversion. The figure shows a tendency towards a smaller standard deviation when the conversion is low, with the increase in standard deviation at higher con-

versions approaching a limit of about $6{\cdot}10^{-4}$. The largest values for the standard deviation are observed from the data points that were repeated seven times, making the upper limit of $6{\cdot}10^{-4}$ rather trustworthy. As noted from the figure, the standard deviation is calculated based on the calcium conversion. In order to estimate the standard deviation on another basis, for instance for CaO, the standard deviation is divided by the mole fraction of the base in the material considered, as a direct consequence of equation 9.1. In the following the standard deviation for the Ca base is put equal to $6{\cdot}10^{-4}$.

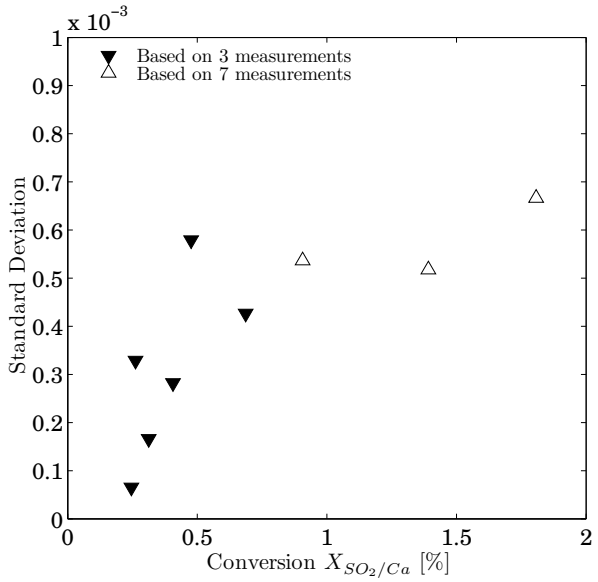

Figure A.2: *The standard deviation calculated from a number of different measurement series.*

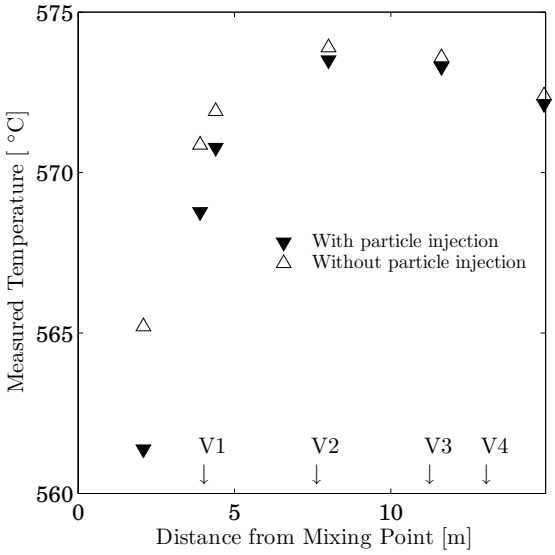

Figure A.3: *Temperature along the reactor tube as a function of the distance from the mixing point. The particles injected are CaO with an injection rate of 500 g/hr.*

A.5 Particle Flow in an Entrained Flow Reactor

As mentioned earlier, the reactor tube is situated horizontally in the reactor oven and contains seven of U-bends. When making calculations on data obtained in the entrained flow reactors it is assumed that the particles will follow the gas flow and be equally distributed in the gas. However, when using a set-up like the entrained flow reactor this assumption may not be valid.

In the straight part of a horizontal reactor tube, gravity can induce a skewed velocity profile due to a higher concentration of particles near the bottom of the tube. Such a skewed profile will cause unequal residence time for the particles, while some particles can experience a lower concentration of certain gas phase components such as SO_2. In the literature, the flow profile in a horizontal tube has been studied by, for instance, Tsuji and Morikawa [168], who used a reactor tube with dimensions similar to that installed in the entrained flow reactor. Their results show that a low solid to gas ratio and a high gas velocity mean that a flow profile similar to the flow profile obtained without solid material in the gas is observed, with the particles following the gas flow closely. Other authors [169, 170] observe this behaviour, too. It

is noteworthy here that the mentioned literature operates with a solid to gas ratio that is up to 30 times higher than that used in the entrained flow reactor, while the gas velocities and particle sizes are similar. Therefore, it is reasonable to assume that, in the straight part of the horizontal tube, the solid materials are dispersed equally and follow the gas flow.
The U-bends, constituting 15 % of the entrained flow reactor length, can cause disturbance in particle flow due to the formation of particle ropes at the outer wall. Ropes are formed due to the centrifugal forces experienced by the particles when entering a U-bend. The formation of particle ropes in U-bends and in elbows is well documented in the literature [171–180]; however, most of the research concerning this subject is related to pneumatic conveying, which is why considerably higher solid to gas ratios, as well as wider tubes, are used in the investigations, while the linear gas velocity and particle sizes are similar to those utilised in the entrained flow reactor. The general decrease in velocity in the outlet of an U-bend or elbow is 40 to 75 % of the linear gas velocity. The tube length needed to disperse the particle rope (re-establishing the original flow pattern) has been estimated in the literature to take about 10 tube diameters.
In order to estimate the influence of rope formation on particle residence time, the residence time is divided into three contributions, namely:

- Residence time in straight parts of the reactor tube ($t_{straight}$). It is assumed that the particles follow the gas flow.
- Residence time in bends (t_{bends}). Particle velocity decreases by a certain percentage (χ) compared to linear gas velocity (υ_{gas}).
- Residence time for dispersion (t_{disp}). Dispersion takes place over a number (N_{disp}) of tube diameters, which here are assumed to be 10 in total. The acceleration of the particles from the bend outlet to the gas velocity is assumed to be linear from the bend outlet velocity up to the gas velocity.

In Figure A.4, the reactor tube is outlined with the relevant dimensions required for calculating different contributions to the residence time.
Equation A.1-A.3 shows the expressions for calculating the residence time in each part of the reactor tube, and Table A.1 shows the distance from the four gas inlets to the gas sampling point (L_{tube}) and the number of bends (N_{bends}) for each of the four gas inlet points.

$$t_{straight} = \frac{L_{tube} - 0.5\pi D_{bend} N_{bends} - D_{tube}\left(N_{disp}\left(N_{bends}+1\right) - 1.2\right)}{\upsilon_{gas}} \tag{A.1}$$

$$t_{bends} = \frac{0.5\pi D_{bend} N_{bends}}{(1-\chi)\upsilon_{gas}} \tag{A.2}$$

$$t_{disp} = \frac{D_{tube}\left(N_{disp}\left(N_{bends}+1\right) - 1.2\right)}{0.5\upsilon_{gas}(1+(1-\chi))} \tag{A.3}$$

	Distance to gas sampling, L_{tube}	Number of bends , N_{bends}
V1	473.8D_{tube}	5
V2	313.2D_{tube}	3
V3	152.6D_{tube}	1
V4	72.1D_{tube}	0

Table A.1: *Distances from the gas inlet to gas sampling in the reactor tube as a function of the tube diameter.*

Figure A.5 shows the increase in residence time as a function of the deviation of particle velocity in proportion to gas velocity. It is clear that this increase can be significant if the particle velocity is strongly reduced in the bends. However, if the decrease in particle velocity can be kept at 40 % compared to the linear gas velocity, the increase in residence time observed for inlet point V1 is only 13 %. Since both the particle loading and tube diameter used here are significantly smaller than that used in the literature, it is believed that a deviation from gas velocity in the bends of no more than 40 % is realistic.
Based on this evaluation it is concluded that particles can be assumed to follow the gas flow without any significant discrepancy.

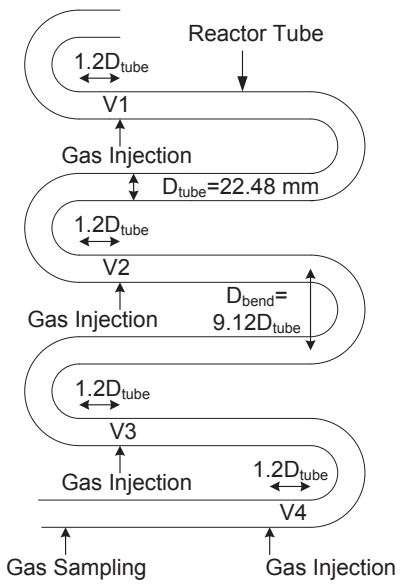

Figure A.4: *Schematic drawing of the reactor tube, with relevant dimensions.*

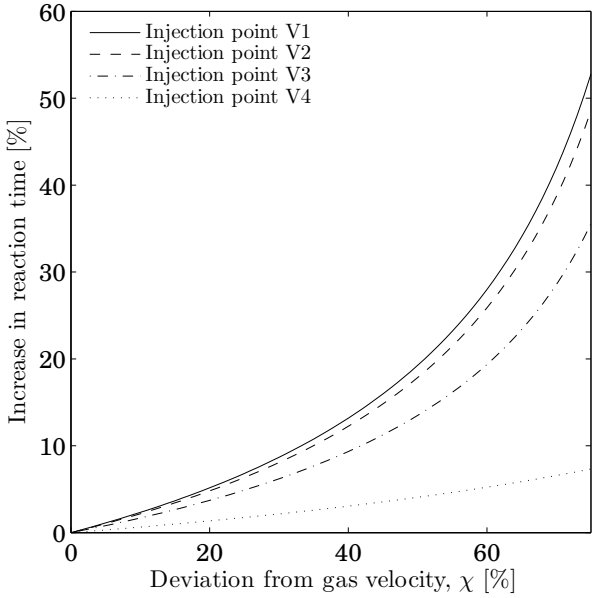

Figure A.5: *Increase in residence time as a function of the deviation from gas velocity in the bends. The calculations are based on a gas velocity of 20 m/s and rope dispersion length of 10 times the tube diameter.*

Appendix B

Models for Evaluating Mass and Temperature Gradients

B.1 Weisz-Prater Modulus

Equation B.1 shows the definition of the Weisz-Prater modulus.

$$C_{WP} = \frac{-r'''_{obs,SO_2} \cdot R_p^2}{C_{SO_2,surface} \cdot D_{e,SO_2}} \tag{B.1}$$

Here, r'''_{obs,SO_2} denotes the average observed reaction rate, R_p the particle radius, $C_{SO_2,surface}$ the SO_2 concentration at the particle surface and D_{e,SO_2} the effective pore diffusion coefficient. The parameters -r'''_{obs,SO_2}, $C_{SO_2,surface}$ and D_{e,SO_2} are calculated from equation B.2-B.4, respectively. In equation B.3 it is assumed that the reaction gas is ideal and the surface concentration is equal to the bulk concentration. When calculating the effective pore diffusion coefficient, Knudsen diffusion is neglected because the average primary pore diameter is about 0.5 μm. The expression for D_{SO_2} is taken from Massman [158]. Several authors [159–162] have found that a tortuosity factor of 1.5 is suitable for materials such as $CaCO_3$ and CaO.

$$-r'''_{obs,SO_2} = -\frac{1}{V_p}\frac{dN_{SO_2}}{dt} \tag{B.2}$$

$$C_{SO_2,surface} = x_{SO_2,bulk}\frac{P}{RT} \tag{B.3}$$

$$D_{e,SO_2} = \frac{\phi}{\tau} \cdot D_{SO_2} = \frac{\phi}{\tau} \cdot 1.1 \cdot 10^{-5}\left(\frac{T}{273.15}\right)^{1.81} \tag{B.4}$$

The expression for r'''_{obs,SO_2} is rewritten, assuming that dN_{SO_2} and dt can be replaced by ΔN_{SO_2} and Δt. If the definition of the CaO conversion (equation 9.1) is introduced and the particle volume (V_p) expressed, as seen in equation B.5, ρ_p is the particle density, M_{CaO} the molar mass of CaO and Q_{CaO} the weight fraction of CaO in the particles utilised. The average observed reaction rate can then be calculated from equation B.6.

$$V_p = \frac{N_{CaO} \cdot M_{CaO}}{\rho_p \cdot Q_{CaO}} \tag{B.5}$$

$$-r'''_{obs,SO_2} = \frac{\rho_p \cdot Q_{CaO}}{M_{CaO}} \frac{X_{SO_2/CaO}}{\Delta t} \tag{B.6}$$

B.2 Mears Criterion

Equation B.7 shows the definition of the Mears criterion.

$$C_M = \frac{-r'''_{obs,SO_2} \cdot R_p \cdot n}{K_{SO_2} \cdot C_{SO_2,bulk}} \tag{B.7}$$

Here, n is the reaction order and K_{SO_2} the mass transfer coefficient for SO_2 in the outer gas film. K_{SO_2} is related to the Sherwood number (Sh) through equation B.8

$$Sh = \frac{2 \cdot K_{SO_2} \cdot R_p}{D_{SO_2}} \tag{B.8}$$

Here, D_{SO_2} is obtained from Massman [158]. If no other data is available a Sherwood number of 2 should be used, corresponding to a spherical particle at rest in a stagnant gas.

B.3 Temperature Gradients

A temperature profile for a spherical particle can be calculated from the partial differential equation in B.9.

$$\rho_p \cdot C_{p,s} \frac{\partial T}{\partial t} = \frac{K_s}{r^2} \cdot \frac{\partial}{\partial r} \left(r^2 \frac{\partial T}{\partial r} \right) + E(r) \tag{B.9}$$

Here, $C_{p,s}$ is the heat capacity of the solid material, K_s the thermal conductivity of the particle and $E(r)$ the energy evolved due to chemical reactions. Equation B.9 is based on the assumption that only temperature gradients in the radial direction exist.
The initial and boundary conditions for equation B.9 are as follows:

$$T = T_{int} \;\; at \;\; t = 0 \tag{B.10}$$

$$\frac{\partial T}{\partial r} = 0 \;\; at \;\; r = 0 \tag{B.11}$$

$$K_g \frac{\partial T}{\partial r} = h_g \cdot (T_{bulk} - T_{surface}) \;\; at \;\; r = 1 \tag{B.12}$$

The Neumann boundary condition (equation B.12) implies that a temperature gradient in an outer gas film is possible. Here, h_g is the convective heat transfer coefficient for the gas film, and is related to the Nusselt number by equation B.13.

$$Nu = \frac{2 \cdot h_g \cdot R_p}{K_g} \tag{B.13}$$

If no other data is available, a value of 2 should be used for the Nusselt number, corresponding to a particle at rest in a stagnant gas.
The model is made dimensionless by introducing the following dimensionless variables: $T^* = \frac{T}{T_{bulk}}$,

$z = \frac{r}{R_p}$ $\tau = \frac{t}{t_r}$, where t_r is the total reaction time. The variable transformation results in the dimensionless energy balance shown in equation B.14.

$$\frac{\partial T^*}{\partial \tau} = \frac{K_s \cdot t_r}{\rho_p \cdot C_{p,s} \cdot R_p^2} \cdot \frac{1}{z^2} \frac{\partial}{\partial z} \left(z^2 \frac{\partial T^*}{\partial z} \right) + \frac{t_r}{\rho_p \cdot C_{p,s} \cdot T_{bulk}} \cdot E(z) \tag{B.14}$$

with the dimensionless boundary conditions in equation B.15-B.17.

$$T^* = \frac{T_{int}}{T_{bulk}} \quad at \quad \tau = 0 \tag{B.15}$$

$$\frac{\partial T^*}{\partial z} = 0 \quad at \quad z = 0 \tag{B.16}$$

$$\frac{\partial T^*}{\partial z} = \frac{h_g \cdot R_p}{K_g} \cdot \left(1 - T^*_{surface}\right) \quad at \quad z = 1 \tag{B.17}$$

The energy evolved due to chemical reactions is modelled as a step function, as seen in equation B.18. This way of modelling the reaction energy happens because, as we know from section 11.1, for most particle sizes only a thin outer shell takes part in the reaction.

$$E(z) = \begin{cases} \frac{1}{1-\xi^3} \cdot r'''_{obs,i} \cdot \Delta H_{reac,i} & \text{if } z > \xi \\ 0 & \text{if } z \leq \xi \end{cases} \tag{B.18}$$

Here, $\Delta H_{reac,i}$ denotes that the reaction enthalpy and ξ are the radius of the unreacted core divided by the particle radius.
When considering the CaO/SO_2 reaction, sulphation takes place according to B.19. This reaction is chosen as an upper limit on the energy that can be evolved when CaO reacts with SO_2.

$$CaO + SO_2 + 0.5O_2 \rightarrow CaSO_4 \tag{B.19}$$

In Table B.1 the relevant values needed for solving equation B.14 are shown at 25 °C and 600 °C. When solving equation B.14 it is assumed that K_s, $\Delta H_{reac,i}$ and ρ_p are temperature independent, with an average value of $\Delta H_{reac,i}$ used. $C_{p,s}$, $C_{p,g}$ and K_g are all temperature dependent, and equations for these parameters as a function of temperature are stated in Appendix F. The particle porosity of 1300 kg/m^3 is chosen because it is the porosity at which Satterfield and Feakes [181] measured K_{CaO}.

Parameter	Value at 25 °C	Value at 600 °C	Reference
$C_{p,CaO}$	852 J/kg/K	1236 J/kg/K	[165]
$C_{p,g}$	975 J/kg/K	1144 J/kg/K	[165]
K_{CaO}	0.6 W/s/m	0.6 W/s/m	[181]
K_g	0.02 W/s/m	0.06 W/s/m	[165]
$\Delta H_{reac,SO_2}$	502 kJ/mol	492 kJ/mol	[164]
$\Delta H_{reac,CO_2}$	502 kJ/mol	492 kJ/mol	[164]
ρ_p	1300 kg/m^3	1300 kg/m^3	[181]

Table B.1: *Data needed for solving the energy balance*

The partial differential equation established here is solved by using the Matlab function *pdepe*, which is designed for solving initial boundary value problems for partial differential equation systems in one di-

mension.

B.4 Evaluation of Particle Heating Time

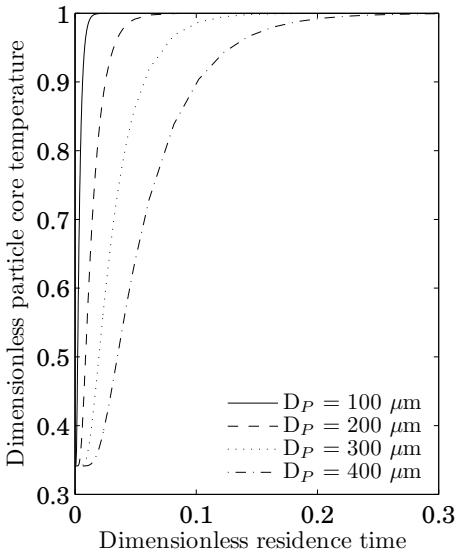

Figure B.1: *Dimensionless particle core temperature as a function of the dimensionless residence time. In the calculations, T_{bulk} was equal to 600 °C, while t_r was 0.215 s.*

The model established above is used here to evaluate whether the particles will be isothermal when SO_2 and CO_2 are injected into the reactor tube. In Appendix A it is shown that the distance from the mixing point, where hot gas and cold particles are mixed, to the first injection point for SO_2/CO_2 is 4.3 m. With a linear gas velocity of up to 20 m/s, the particles will, as a minimum, have 0.215 s to reach the reactor temperature. Figure B.1 shows the core temperature for four different particle diameters as a function of the dimensionless residence time. A dimensionless residence time of 1 corresponds, in Figure B.1, to 0.215 s, which is why it is concluded that the particles will obtain reactor temperature well before SO_2 and CO_2 are injected.

Appendix C

Mass Balances

Gas mass balance for riser zones 1 and 3

$$In = \rho_{gas} \cdot V_g \cdot Y_{i,1R}|_{x_j+\Delta x_j} \tag{C.1}$$

$$Out = \rho_{gas} \cdot V_g \cdot Y_{i,1R}|_{x_j} \tag{C.2}$$

$$Formed = \rho_{gas} \cdot \pi \cdot r_R^2 \cdot \Delta x_j \cdot R_{i,g} \tag{C.3}$$

Solid mass balance for riser zones 1 and 3

$$In = \rho_{gas} \cdot y_{solid,z} \cdot V_g \cdot X_{i,1R}|_{x_j+\Delta x_j} \tag{C.4}$$

$$Out = \rho_{gas} \cdot y_{solid,z} \cdot V_g \cdot X_{i,1R}|_{x_j} \tag{C.5}$$

$$Formed = \rho_{gas} \cdot y_{solid,z} \cdot \pi \cdot r_R^2 \cdot \Delta x_j \cdot R_{i,s} \tag{C.6}$$

Gas mass balance for riser zone 2

$$In = \rho_{gas}(T_{hot}) \cdot V_{g,2}(T_{hot}) \cdot Y_{i,2R}|_{x_j+\Delta x_j} \tag{C.7}$$

$$Out = \rho_{gas}(T_{hot}) \cdot V_{g,2}(T_{hot}) \cdot Y_{i,2R}|_{x_j} \tag{C.8}$$

$$Formed = \pi \cdot r_R^2 \cdot \Delta x_j \cdot (\rho_{gas}(T_{hot}) \cdot R_{i,g}(T_{hot}) + \rho_{gas}(T_{hot}) \cdot R_{i,g}(T_{cold})) \tag{C.9}$$

Solid mass balance for riser zone 2, with hot solid material

$$In = \rho_{gas}(T_{hot}) \cdot y_{solid,z,hot} \cdot V_{g,2}(T_{hot}) \cdot X_{i,2R}|_{x_j+\Delta x_j} \tag{C.10}$$

$$Out = \rho_{gas}(T_{hot}) \cdot y_{solid,z,hot} \cdot V_{g,2}(T_{hot}) \cdot X_{i,2R}|_{x_j} \tag{C.11}$$

$$Formed = \rho_{gas}(T_{hot}) \cdot y_{solid,z,hot} \cdot \pi \cdot r_R^2 \cdot \Delta x_j \cdot R_{i,s}(T_{hot}) \tag{C.12}$$

Solid mass balance for riser zone 2, with cold solid material

$$In = \rho_{gas}(T_{hot}) \cdot y_{solid,z,cold} \cdot V_{g,2}(T_{hot}) \cdot X_{i,2R}|_{x_j+\Delta x_j} \tag{C.13}$$

$$Out = \rho_{gas}(T_{hot}) \cdot y_{solid,z,cold} \cdot V_{g,2}(T_{hot}) \cdot X_{i,2R}|_{x_j} \tag{C.14}$$

$$Formed = \rho_{gas}(T_{hot}) \cdot y_{solid,z,cold} \cdot \pi \cdot r_R^2 \cdot \Delta x_j \cdot R_{i,s}(T_{cold}) \tag{C.15}$$

Solid mass balance for cyclone zone 1

$$In = y_{solid,z} \cdot \rho_{gas} \cdot V_{g,1}|_{x_j+\Delta x_j} \cdot X_{i,1}|_{x_j+\Delta x_j} \tag{C.16}$$

$$Out = y_{solid,z} \cdot \rho_{gas} \left(V_{g,1}|_{x_j} \cdot X_{i,1}|_{x_j} + 2 \cdot \pi \cdot r_1 \cdot \Delta x_j \cdot U_r \cdot X_{i,2}|_{x_j} \right) \tag{C.17}$$

$$Formed = y_{solid,z} \cdot \rho_{gas} \cdot \pi \cdot r_1^2 \cdot \Delta x_j \cdot R_{i,s} \tag{C.18}$$

Solid mass balance for cyclone zone 2

$$In = y_{solid,z} \cdot \rho_{gas} \left(V_{g,2}|_{x_j} \cdot X_{i,2}|_{x_j} + 2 \cdot \pi \cdot r_1 \cdot \Delta x_j \cdot U_r \cdot X_{i,2}|_{x_j} \right) \tag{C.19}$$

$$Out = y_{solid,z} \cdot \rho_{gas} \cdot V_{g,2}|_{x_j+\Delta x_j} \cdot X_{i,2}|_{x_j+\Delta x_j} \tag{C.20}$$

$$Formed = y_{solid,z} \cdot \rho_{gas} \cdot \pi \cdot (r_2^2 - r_1^2) \cdot \Delta x_j \cdot R_{i,s} \tag{C.21}$$

Solid mass balance for cyclone zone 3

$$In = \rho_{solid} \cdot V_s \cdot X_{i,3}|_{x_j} \tag{C.22}$$

$$Out = \rho_{solid} \cdot V_s \cdot X_{i,3}|_{x_j+\Delta x_j} \tag{C.23}$$

$$Formed = \frac{1}{1+\epsilon} \cdot \rho_{solid} \cdot \pi \cdot (r_3^2 - r_2^2) \cdot \Delta x_j \cdot R_{i,s} \tag{C.24}$$

Gas mass balance for cyclone zone 1

$$In = \rho_{gas} \cdot V_{g,1}|_{x_j+\Delta x_j} \cdot Y_{i,1}|_{x_j+\Delta x_j} \tag{C.25}$$

$$Out = \rho_{gas} \cdot V_{g,1}|_{x_j} \cdot Y_{i,1}|_{x_j} + 2 \cdot \rho_{gas} \cdot \pi \cdot r_1 \cdot \Delta x_j \left(K_{1\to 2} \cdot \left(Y_{i,1}|_{x_j} - Y_{i,2}|_{x_j} \right) + U_r \cdot Y_{i,2}|_{x_j} \right) \tag{C.26}$$

$$Formed = \rho_{gas} \cdot \pi \cdot r_1^2 \cdot \Delta x_j \cdot R_{i,g} \tag{C.27}$$

Total gas balance for zone 1

$$In = \rho_{gas} \cdot V_{g,1}|_{x_j+\Delta x_j} \tag{C.28}$$

$$Out = \rho_{gas} \cdot V_{g,1}|_{x_j} + 2 \cdot \rho_{gas} \cdot \pi \cdot r_1 \cdot \Delta x_j U_r \tag{C.29}$$

Gas mass balance for cyclone zone 2

$$In = \rho_{gas} \cdot V_{g,2}|_{x_j} \cdot Y_{i,2}|_{x_j} + 2 \cdot \rho_{gas} \cdot \pi \cdot r_1 \cdot \Delta x_j \left(K_{1\to 2} \cdot \left(Y_{i,1}|_{x_j} - Y_{i,2}|_{x_j}\right) + U_r \cdot Y_{i,2}|_{x_j}\right) \tag{C.30}$$

$$Out = \rho_{gas} \cdot V_{g,2}|_{x_j+\Delta x_j} \cdot Y_{i,2}|_{x_j+\Delta x_j} + 2 \cdot \rho_{gas} \cdot \pi \cdot r_2 \cdot \Delta x_j \cdot K_{2\to 3} \cdot \left(Y_{i,2}|_{x_j} - Y_{i,3}|_{x_j}\right) \tag{C.31}$$

$$Formed = \rho_{gas} \cdot \pi \cdot (r_2^2 - r_1^2) \cdot \Delta x_j \cdot R_{i,g} \tag{C.32}$$

Total gas balance for zone 2

$$In = \rho_{gas} \cdot V_{g,2}|_{x_j} + 2 \cdot \rho_{gas} \cdot \pi \cdot r_1 \cdot \Delta x_j U_r \tag{C.33}$$

$$Out = \rho_{gas} \cdot V_{g,2}|_{x_j+\Delta x_j} \tag{C.34}$$

Gas mass balance for cyclone zone 3

$$In = V_s \cdot \epsilon \rho_{gas} \cdot Y_{i,3}|_{x_j} + 2 \cdot \frac{\epsilon}{1+\epsilon} \cdot K_{2\to 3} \cdot \rho gas \cdot \pi \cdot r_2 \cdot \Delta x_j \left(Y_{i,2}|_{x_j} - Y_{i,3}|_{x_j}\right) \tag{C.35}$$

$$Out = V_s \cdot \epsilon \cdot \rho_{gas} \cdot Y_{i,3}|_{x_j+\Delta x_j} \tag{C.36}$$

$$Formed = \frac{\epsilon}{1+\epsilon} \cdot \pi \cdot \rho_{gas} \cdot (r_3^2 - r_2^2) \cdot \Delta x_j \cdot R_{i,g} \tag{C.37}$$

Appendix D

Dimensionless Equation System

Riser zones 1 and 3

$$\frac{dX^*_{i,zR}}{dz_j} = \frac{\pi \cdot r_R^2 \cdot H}{V_{g,zR} \cdot X_{i,0}} \cdot R_{i,s} \tag{D.1}$$

$$\frac{dY^*_{i,zR}}{dz_j} = \frac{\pi \cdot H \cdot r_R^2}{V_{g,zR} \cdot Y_{i,0}} \cdot R_{i,g} \tag{D.2}$$

Riser zone 2

$$\frac{dY^*_{i,2R}}{dz_j} = \frac{\pi \cdot r_R^2 \cdot H}{V_{g,2R}(T_{hot}) \cdot Y_{i,0}} \left(R_{i,g}(T_{hot}) + R_{i,g}(T_{cold})\right) \tag{D.3}$$

$$\frac{dX^*_{i,2R,hot}}{dz_j} = -\frac{\pi \cdot r_R^2 \cdot H}{V_{g,2R}(T_{hot}) \cdot X_{i,0}} R_{i,s}(T_{hot}) \tag{D.4}$$

$$\frac{dX^*_{i,2R,cold}}{dz_j} = -\frac{\pi \cdot r_R^2 \cdot H}{V_{g,2R}(T_{hot}) \cdot X_{i,0}} \cdot R_{i,s}(T_{cold}) \tag{D.5}$$

$$\frac{dT_{hot}}{dz_j} = \frac{T_i - T_{i+1}}{L^*_2 - L^*_1} \tag{D.6}$$

$$\frac{dT_{cold}}{dz_j} = \frac{T_i - T_{i-1}}{L^*_2 - L^*_1} \tag{D.7}$$

Cyclone zone 1

$$\frac{dX^*_{i,1}}{dz_j} = \frac{2 \cdot \pi \cdot r_1 \cdot H \cdot U_{r,0}}{V_{g,0}} \cdot \frac{\left(X^*_{i,2} - X^*_{i,1}\right) \cdot U^*_r}{W_{g,1}} - \frac{\pi \cdot r_1^2 \cdot H}{V_{g,0} \cdot X_{i,0}} \cdot \frac{R_{i,s}}{W_{g,1}} \tag{D.8}$$

$$\frac{dY^*_{i,1}}{dz_j} = \frac{2 \cdot \pi \cdot r_1 \cdot H}{V_{g,0}} \cdot \frac{(U_{r,0} \cdot U^*_r - K_{1\to2}) \cdot \left(Y^*_{i,2} - Y^*_{i,1}\right)}{W_{g,1}} - \frac{\pi \cdot r_1^2 \cdot H}{V_{g,0} \cdot Y_{i,0}} \cdot \frac{R_{i,g}}{W_{g,1}} \tag{D.9}$$

Cyclone zone 2

$$\frac{dX^*_{i,2}}{dz_j} = \frac{\pi \cdot H \cdot \left(r_2^2 - r_1^2\right)}{V_{g,0} \cdot X_{i,0}} \cdot \frac{R_{i,s}}{W_{g,2}} \tag{D.10}$$

$$\begin{aligned}\frac{dY^*_{i,2}}{dz_j} = 2 \cdot \pi \cdot H \frac{r_1 \cdot K_{1\to2} \cdot \left(Y^*_{i,1} - Y^*_{i,2}\right) - r_2 \cdot K_{2\to3} \cdot \left(Y^*_{i,2} - Y^*_{i,3}\right)}{V_{g,0} \cdot W_{g,2}} + \\ \frac{\pi \cdot H \cdot \left(r_2^2 - r_1^2\right)}{V_{g,0} \cdot Y_{i,0}} \cdot \frac{R_{i,g}}{W_{g,2}}\end{aligned} \tag{D.11}$$

Cyclone zone 3

$$\frac{dX^*_{i,3}}{dz_j} = \frac{1}{1+\epsilon} \cdot \frac{\pi \cdot H \cdot \left(r_3^2 - r_2^2\right)}{X_{i,0} \cdot V_{s,3}} \cdot R_{i,s} \tag{D.12}$$

$$\frac{dY^*_{i,3}}{dz_j} = \frac{1}{1+\epsilon} \cdot \frac{2 \cdot \pi \cdot H \cdot K_{2\to3} \cdot r_2}{V_{s,3}} \cdot \left(Y^*_{i,2} - Y^*_{i,3}\right) + \frac{1}{1+\epsilon} \cdot \frac{\pi \cdot H \cdot \left(r_3^2 - r_2^2\right)}{Y_{i,0} \cdot V_{s,3}} \cdot R_{i,g} \tag{D.13}$$

Boundary conditions for riser zone 1

$$Y^*_{i,1R} = Y^*_{i,Stage\ i+1} \ \ \& \ \ X^*_{i,1R} = X^*_{i,Stage\ i+1} \ \ at \ \ z_j = 1 \tag{D.14}$$

Boundary conditions for riser zone 2

$$T_{hot} = T_{i-1} \ \ \& \ \ T_{cold} = T_{i+1} \ \ at \ \ z_j = L^*_2 \tag{D.15}$$

$$X^*_{i,2Rs} = X^*_{i,Stage\ i-1} \ \ \& \ \ X^*_{i,2Rg} = X^*_{i,1R}|_{z_j=L^*_2} \ \ \& \ \ Y^*_{i,2R} = Y^*_{i,1R}|_{z_j=L^*_2} \ \ at \ \ z_j = L^*_2 \tag{D.16}$$

Boundary conditions for riser zone 3

$$Y^*_{i,3R} = Y^*_{i,2R}|_{z_j=L^*_1} \ \ \& \ \ X^*_{i,3R} = X^*_{i,2R}|_{z_j=L^*_1} \ \ at \ \ z_j = L^*_1 \tag{D.17}$$

Boundary conditions for cyclone section

$$X^*_{i,1} = X^*_{i,2} \ \ at \ \ z_j = 1 \quad \& \quad X^*_{i,2} = X^*_{i,3} = X^*_{i,3R}|_{z_j=0} \ \ at \ \ z_j = 0 \tag{D.18}$$

$$Y^*_{i,1} = Y^*_{i,2} \ \ at \ \ z_j = 1 \quad \& \quad Y^*_{i,2} = Y^*_{i,3} = Y^*_{i,3R}|_{z_j=0} \ \ at \ \ z_j = 0 \tag{D.19}$$

$$W_{g,1} = W_{g,2} = 1 \ \ at \ \ z_j = 0 \tag{D.20}$$

Appendix E

Input Values for Simulating Plants A-E

Parameter	Unit	Plant A	Plant B	Plant C	Plant D	Plant E
$w_{CaCO_3,0,bot}$	kg/s	47.08	56.85	32.96	30.98	47.08
$w_{SiO_2,0,bot}$	kg/s	12.56	15.16	8.79	8.26	12.56
$w_{Al_2O_3,0,bot}$	kg/s	1.88	2.27	1.32	1.24	1.88
$w_{FeO,0,bot}$	kg/s	1.26	1.52	0.88	0.83	1.26
$w_{FeS_2,0,bot}$	kg/s	0.08	0.10	0.03	0.04	0.06
$w_{FeS,0,bot}$	kg/s	0.08	0.10	0.03	0.04	0.06
$w_{CaSO_3,0,bot}$	kg/s	0	0	0	0	0
x_{N_2}		0.64	0.63	0.63	0.68	0.66
x_{CO_2}		0.33	0.33	0.35	0.27	0.30
x_{O_2}		0.03	0.04	0.02	0.05	0.04
$Q_{CaCO_3,N+1}$		0.74	0.74	0.74	0.74	0.74
$Q_{SiO_2,N+1}$		0.20	0.20	0.20	0.20	0.20
$Q_{Al_2O,N+1}$		0.03	0.03	0.03	0.03	0.03
$Q_{FeO,N+1}$		0.02	0.02	0.02	0.02	0.02
$Q_{FeS_2,N+1}$		0	0	0	0	0
$Q_{FeS,N+1}$		0	0	0	0	0
$Q_{CaSO_3,N+1}$		0.01	0.01	0.01	0.01	0.01
$x_{s,1}$		0.92	0.80	0.90	0.91	0.92
$x_{s,2}$		0.90	0.75	0.90	0.82	0.78
$x_{s,3}$		0.86	0.75	0.80	0.69	0.79
$x_{s,4}$		0.82	0.85	0.85	0.83	0.66
$x_{s,5}$		0.80	0.60			
$x_{s,6}$		0.55				

Table E.1: *Input parameters used when simulating plants A-E*

Parameter	Unit	Plant A	Plant B	Plant C	Plant D	Plant E
D_1	m	5.7	6.9	4	3.5	5.2
D_2	m	5.7	6.9	5.7	4.8	7.6
D_3	m	6	7.2	5.7	5.2	7.6
D_4	m	6	7.2			
D_5	m	6				
P_{all}	Pa	101325	101325	101325	101325	101325
$G_{N+1,top}$	kg/s	72.19	82.25	43.14	44.80	63.89
T_0	K	298	333	347	333	333
T_{N+1}	K	1137	1143	1143	1090	1166
t_r	s	8	8	8	8	8
ρ_{solid}	kg/m^3	2200	2200	2200	2200	2200
hel		0.2	0.2	0.2	0.2	0.2
ϵ		4	4	4	4	4
U_r	m/s	0	0	0	0	0
$K_{1\rightarrow 2}$	m/s	0	0	0	0	0
$A_{BET,Raw\ meal}$	m^2/kg	3195	5025	5723	10373	7913

Table E.2: *Input parameters used when simulating plants A-E*

Appendix F

Temperature Dependent Parameters

Heat Capacities

$$C_{p,CaO} = -2.21 \cdot 10^{-4} \cdot T^2 + 0.49 \cdot T + 687 \quad \left[\frac{J}{kg \cdot K}\right]$$

$$C_{p,g} = x_{N_2,bulk} \left(2.07 \cdot 10^{-4} \cdot T^2 - 6.12 \cdot 10^{-2} \cdot T + 1038\right) + x_{CO_2,bulk} \left(326 \cdot ln(T) - 1009\right) \quad \left[\frac{J}{kg \cdot K}\right]$$

Thermal conductivities

$$C_{p,g} = x_{N_2,bulk} \left(5.77 \cdot 10^{-5} \cdot T + 9.14 \cdot 10^{-3}\right) + x_{CO_2,bulk} \left(7.87 \cdot 10^{-5} \cdot T - 6.16 \cdot 10^{-3}\right) \quad \left[\frac{W}{m \cdot K}\right]$$

Enthalpies

$$H_i(T) = \frac{A \cdot T}{1000} + \frac{B}{2}\left(\frac{T}{1000}\right)^2 + \frac{C}{3}\left(\frac{T}{1000}\right)^3 + \frac{D}{4}\left(\frac{T}{1000}\right)^4 - \frac{1000 \cdot E}{T} + F - H \quad \left[\frac{kJ}{mol}\right]$$

$$H_{CaCO_3(s)} = 2.20 \cdot 10^{-5} \cdot T^2 + 0.081 \cdot T - 26.49 \quad \left[\frac{kJ}{mol}\right]$$

	A	B	C	D	E	F	H
Al_2O_3 (s)	106.92	36.62	-13.98	2.16	-3.16	-1710.50	-1666.49
SiO_2 (s)	72.77	1.29	$-4{\cdot}10^{-3}$	$8{\cdot}10^{-4}$	-4.14	-941.14	-905.49
CO_2 (g)	25.00	55.19	-33.69	7.95	-0.14	-403.61	-393.52
O_2 (g) ($T \leq 700K$)	31.32	-20.24	57.87	-36.51	-0.01	-8.90	0.00
O_2 (g) ($T > 700K$)	30.03	8.77	-3.99	0.79	-0.74	-11.32	0.00
N_2 (g) ($T \leq 500K$)	28.99	1.85	-9.65	16.64	0.00	-8.67	0.00
N_2 (g) ($T > 500K$)	19.51	19.89	-8.60	1.37	0.53	-4.94	0.00
CaO (s)	49.95	4.89	-0.35	0.05	-0.83	-652.97	-635.09
FeO (s)	45.75	18.79	-5.95	0.85	-0.08	-286.74	-272.04
H_2O (l)	-203.61	1523.29	-3196.41	2474.46	3.86	-256.55	-285.83
H_2O (g)	30.09	6.83	6.79	-2.53	0.08	-250.88	-241.83

Table F.1: *Constants needed for calculating enthalpies. All values are taken from Nist [165]*

Appendix G

Data Handling Program (DHP)

DHP makes use of the Graphical User Interface (GUI) in Matlab in order to ease handling of large data files produced in the laboratory. The program helps the user to identify and calculate the steady-state values in an easy manner. Besides these values, the program also calculates the standard deviation upon the steady-state values. Using GUI makes the program simple to use, even for people without experience in Matlab.

G.1 Input to DHP

DHP can handle NxM data matrices such as the one shown in Table G.1. The first row should contain the column headers and the second row the unit of the column value, while rows three and four should contain numbers (no dates or times). Rows one and two can contain strings as well as numeric values, while row three and onward can only contain numeric values. The decimal point should be a dot(.) and no thousand separator should be used in the data file. DHP can handle both $.txt$ files and $.xls$ files, which should fulfil the requirements stated above.

Parameter	Parameter	Parameter	$\rightarrow$
Unit	Unit	Unit	$\rightarrow$
Value	Value	Value	$\rightarrow$
Value	Value	Value	$\rightarrow$
Value	Value	Value	$\rightarrow$
$\downarrow$	$\downarrow$	$\downarrow$	$\searrow$

Table G.1: *Layout of a data matrix that can be used in DHP.*

The algorithm for DHP is shown below.

G.2 DHP Algorithm

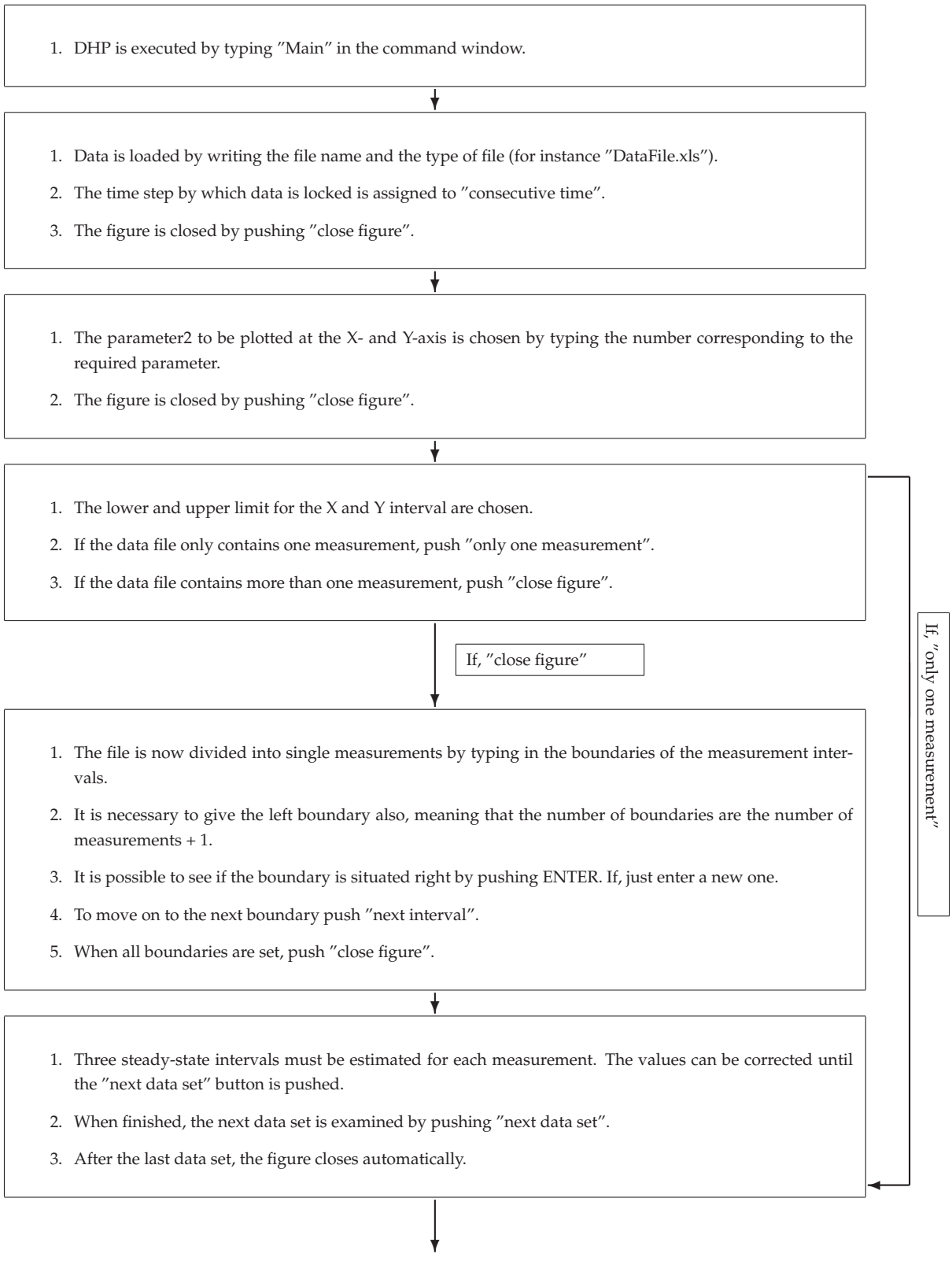

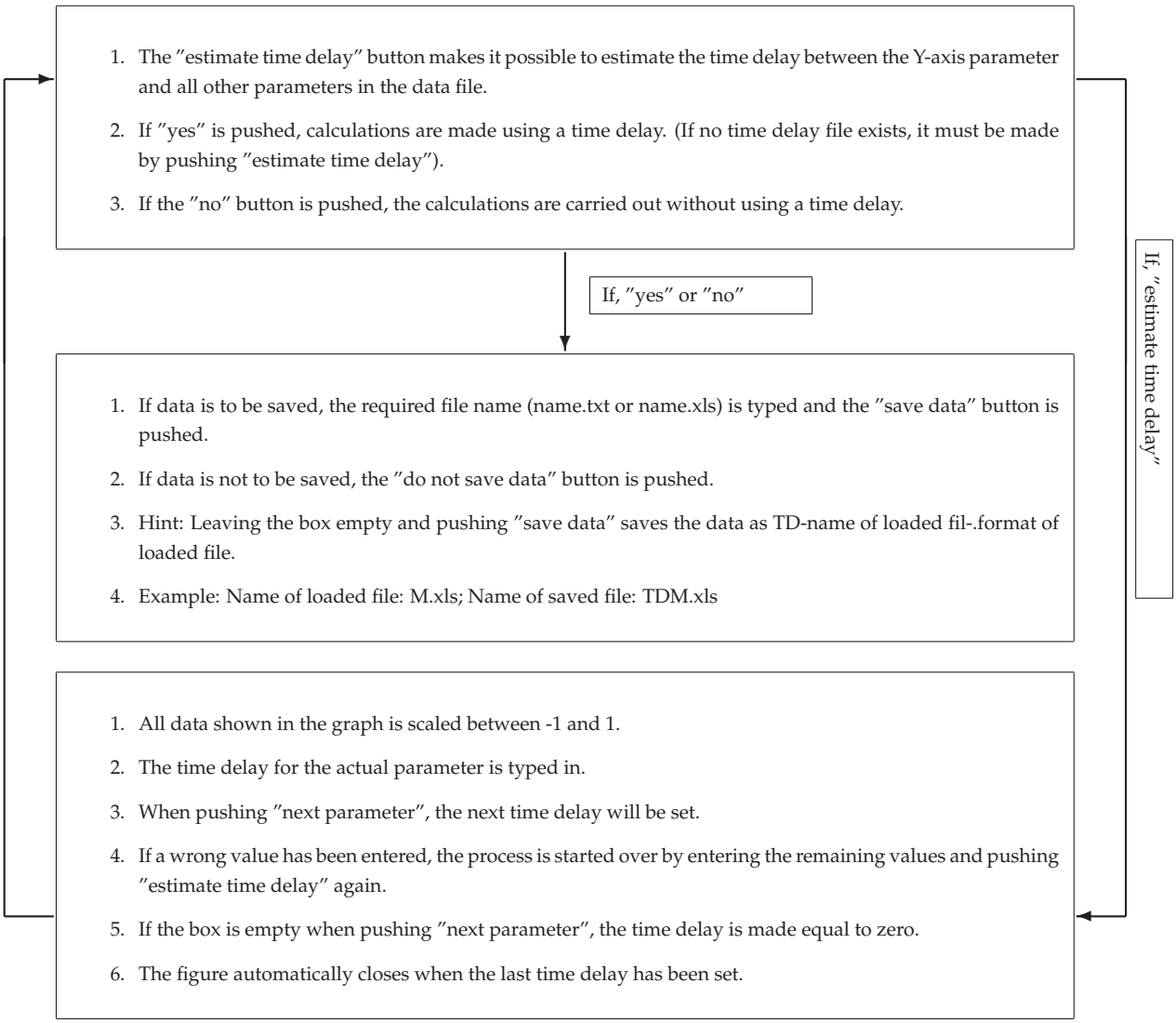
1. The ”estimate time delay” button makes it possible to estimate the time delay between the Y-axis parameter and all other parameters in the data file.
2. If ”yes” is pushed, calculations are made using a time delay. (If no time delay file exists, it must be made by pushing ”estimate time delay”).
3. If the ”no” button is pushed, the calculations are carried out without using a time delay.
If, ”yes” or ”no”
1. If data is to be saved, the required file name (name.txt or name.xls) is typed and the ”save data” button is pushed.
2. If data is not to be saved, the ”do not save data” button is pushed.
3. Hint: Leaving the box empty and pushing ”save data” saves the data as TD-name of loaded fil-.format of loaded file.
4. Example: Name of loaded file: M.xls; Name of saved file: TDM.xls
1. All data shown in the graph is scaled between -1 and 1.
2. The time delay for the actual parameter is typed in.
3. When pushing ”next parameter”, the next time delay will be set.
4. If a wrong value has been entered, the process is started over by entering the remaining values and pushing ”estimate time delay” again.
5. If the box is empty when pushing ”next parameter”, the time delay is made equal to zero.
6. The figure automatically closes when the last time delay has been set.
If, ”estimate time delay”

G.3 Result from DHP

The saved matrix looks like that shown in Table G.2. The number of rows are equal to the number of measurements times 3. The indicator in column one indicates which data is interrelated and is added by the program. The consecutive time column is also added by the program. The rest of the columns correspond to the columns given by the user.

Indicator	Consecutive time	Parameter	Parameter	Parameter	→
****	****	Unit	Unit	Unit	→
Value	Value	Value	Value	Value	→
Value	Value	Value	Value	Value	→
Value	Value	Value	Value	Value	→
↓	↓	↓	↓	↓	↘

Table G.2: *Layout of a matrix resulting from DHP*

G.4 Hints

1. When saving data to an existing file it will NOT be overwritten, the new data will be appended to the existing file.
2. Often, files obtained in the laboratory must be manipulated in order to produce the right format for the Matlab program to handle them. This can often be done in Microsoft Excel and/or Notepad.
3. In the program a number of warnings are built in so that the program does not crash. However, if it does, then try to restart the program.
4. If the program crashes when loading data, it is often because the file that is to be loaded contains a number of erroneous elements. See Table G.1 for an idea of how this file should look.